• Institute of Fundamental Technological Research
• Polish Academy of Sciences
• Warsaw • Poland

LECTURE NOTES 12

Han Zhao

Cellular Materials Under Impact Loading

Centre of Excellence for
Advanced Materials and Structures

WARSAW 2004

AMAS LECTURE NOTES

Production of this volume has been partially supported by the European Commission

Published and distributed by
Institute of Fundamental Technological Research
Świętokrzyska 21, 00-049 Warszawa, Poland

ISSN 1642-0578

Papier offset. kl. III, 70 g, B1
Ark. wyd.: 8,3; ark. druk.: 7
Skład w systemie LaTeX: T.G. Zieliński
Oddano do druku: III 2004; druk ukończono: IV 2004
Druk i oprawa: Drukarnia Braci Grodzickich, Piaseczno, ul. Geodetów 47a

Contents

Preface

This volume summarises the lectures delivered at the Center of Excellence for Advanced Materials and Structures (AMAS) in the Institute of Fundamental and Technological Research, Polish Academy of Sciences, Warsaw.

It begins by a brief survey of different aspects of cellular materials such as manufacturing, applications and mechanical behaviour under static loading (Chapter 1), which is followed by an introduction of elastic and viscoelastic wave propagation theories (Chapter 2). Particular attentions have been paid to the wave dispersion aspects in the cylindrical bar, which are useful for understanding of experimental methods involving bars. More detailed information can be found in Gibson and Ashby (1988, 1997) for cellular materials, and in Achenbach (1978) and Graff (1975) for wave propagation theory.

Chapter 3 provides general descriptions of possible factors affecting the rate sensitivity of cellular materials, such as the rate sensitivity of cell wall materials, the pressure of air entrapped in the cell, the microinertia effect, and the shock enhancement. Cellular materials have dispersive and complex micro-structures and it is difficult to formulate theoretically its rate sensitivity. Therefore, the experimental studies play an important role in looking for appropriate constitutive descriptions. It leads to the following Chapters 4 and 5, which deal with experimental techniques under impact loading. Chapter 4 describes the most common impact testing techniques and provides some critical analyses of their measuring accuracy. Interested readers can refer to the relevant chapters of books of Zukas (1982,1991), Meyers (1994). Chapter 5 presents recent developments of soft nylon Split Hopkinson Pressure Bar for testing soft cellular materials. Different methods to find accurate wave dispersions are introduced. Wave separation method for measuring large strains is also presented.

Studies on the rate sensitivity of various cellular materials such as polymeric foams, aluminium honeycomb and aluminium foams are presented

in Chapter 6. Specific experimental difficulties such as heterogeneous stress and strain fields are described. The dominant factors of the rate sensitivity for each material are also provided. Presented examples are chosen from published works co-authored with Professor G. Gary in (LMS-Ecole Polytechnique) and from recent works performed in LMT-Cachan with my Ph.D students S. Abdennadher and I. Nasri. Here I would like to express my appreciation to have worked with them.

Chapter 7 presents a model-structure study aimed at understanding inertia effects in a progressive folding process. Square tubes (the chosen model structure) made of rate insensitive base materials (brass) are studied experimentally, numerically and theoretically. It is shown that the apparent rate sensitivity of aluminium honeycombs and IFAM aluminium foam can be explained by the inertia effects in the progressive folding process. Interested reader can find details in the Ph.D thesis of S. Abdennadher.

I would like to express my appreciations to Professor W. K. Nowacki (acting director of IPPT) and Professor Z. Mróz (Scientific Coordinator of AMAS) to invite me for this very interesting visit. I appreciated stimulating discussions with Professor H. Petryk, Professor J. J. Telega, and other staff members. I am grateful to M. Basista, K. Doliński, T. G. Zieliński for their kind helps and to I. Ślęczkowska for having arranged all my practical requests during my visit. I am specially grateful to Dr. Qingming Li for his careful proof reading of the manuscript.

Lastly, I would like to express my thanks to my wife Ying and my daughters Anne and Claire, who had to cope with my travelling absences and frequent over night writings.

Palaiseau, September 2003 *Han Zhao*

Chapter 1

Cellular materials: applications, manufacturing and behaviour

1.1. Introduction

Lightweight structure designs were mostly developed in the past decades for aircraft and aerospace structures where structural weight should be minimized. It becomes nowadays an important issue in transportation vehicle designs. For example, a heavier car means more oil consumptions, more air pollution, and more damages in a crash accident. An economical way to reduce the mass is to use sandwiched structures with the core made of cellular materials.

Cellular material can be defined as solid made of relatively regular, either open or closed hollow cells. The cell could be directional hollow columns to form for example a two-dimensional honeycomb or more isotropic hollow sphere such as soup bubbles to fill an arbitrary three-dimensional space.

The most important feature of cellular materials is their low density, or more exactly low relative density, defined as the ratio between the density of the cellular material and that of the cell wall material. Common cellular materials for structural uses have a relative density around the value of 0.1 and the void occupies most of spaces.

Generally, cellular materials differ slightly from porous materials by a relative density smaller than 0.3. It should be noted that the difficulty for the porous material analysis are the interaction between a quasi-incompressible liquid phase and a deformable solid phase because of the pressure variation

due to skeleton deformations under mechanical or thermal loading. In open porous solids, there exists additional problem of the flow transfer of the liquid phase. In the contrary, for cellular materials, the pressure variation of the gas contained in the pore is generally small enough to be neglected. The large void space and the small thickness of the cell wall or edge lead to bending or buckling-dominant deforming modes of cell wall.

1.2. Applications

Cellular materials become popular in industrial applications due to their high specific resistance in terms of weight. They are used mostly in various sandwich beams or plates in order to improve the strength/weight ratio for structures in aircraft, aerospace, automotive, rail vehicle and sport industries. The dominant parameters are the stiffness and the yield stress.

They are also frequently used to absorb energy in accidental impacts. For example, aluminium honeycombs or foams are used in the sandwich shielding of an airplane to reduce bird-impact damages, in the survival cell of a high-speed train to protect conductors, or in the filled box column to absorb kinetic energies in the collision of cars. Cellular materials are also popular in package industry where low resistance (so less expensive) polyurethane and polystyrene foams and paper or thermoplastic honeycombs are used to protect goods in transportion. In this case, important parameters are the mean crushing strength and the lock-up strain where cellular materials densify and their strength increases rapidly. This lock-up strain is obviously smaller than the porosity and following empirical formula fits most of cellular materials:

$$\varepsilon_d = 1 - 1.4\frac{\rho^*}{\rho_s}. \tag{1.1}$$

Other interested properties of cellular materials are their high thermal and acoustical insulating abilities associated with closed cell structures, or in the contrary their good heat transfer and chemical exchange capacities for the open cell structures.

All these properties are often used in a combined way. For example, to protect an aircraft reactor from accidental impacts, sandwich panels with aluminium honeycomb cores are used for their capacity of energy absorptions. They are meanwhile lightweight structures with a good acoustic insulation.

1.3. Manufacturing processes

1.3.1. Honeycombs: directional regular cells

Soft woods can be considered as a natural cellular material. Observations of cork or balsa woods under microscope show that their basic cells are rather regular hollow hexagonal columns as a honeycomb of bee. R. Hooke has already reported cellular structures of corks in 1664.

Common commercial honeycomb for structural use is made of aluminium sheets. Large thin aluminium foils are printed with alternating, parallel, thin stripes of adhesive and then stacked in a press. Once the adhesive cures, the stack of aluminium sheets can be cut through their thickness. The cut slices are afterwards stretched and expanded to form the panel of continuous hexagonal cell shapes like an accordion (Fig. 1.1). When thicker sheets are needed to make higher resistance honeycombs, they are shaped through a pair of corrugated rolls and cemented together afterwards. Meanwhile, basic materials could be papers (often dipped in a tank of resin after expansion), Nomex paper (kevlar fibre sheets) as well as thermoplastics. The latter are usually manufactured by direct extrusions.

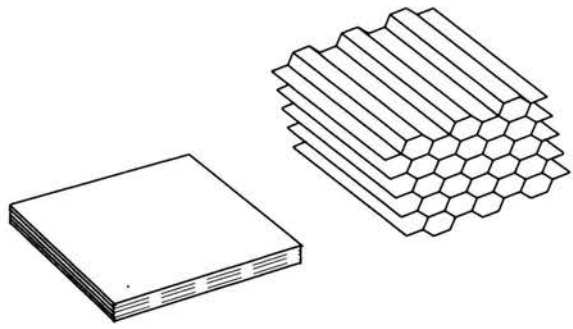

FIGURE 1.1. Honeycomb manufacturing by expansion process.

The main parameters of honeycombs are the cell size, the cell wall thickness as well as the angle between adjacent walls, which can be easily controlled by the pulling displacement in the expansion process.

1.3.2. Foams: more isotropic cells

Polymeric foams are another type of the most common cellular materials. There exist many foamable polymers. The polyurethane is mostly used for

quite low strength flexible foams. Stronger PVC foams are manufactured for structural composite cores. These foams are generally obtained by dispersing a gas phase into polymer melt, often with aid of a chemical blowing agent. The cell nucleation takes place under suitable temperature and pressure. Cells are initially closed, then their sizes increase with the thinning of cell walls, which gives different density of closed cell foams. The coarsening coalescence and collapse may happen afterwards which produce so-called open cell foams (Fig. 1.2).

FIGURE 1.2. Foaming process for polymers.

These techniques are also applied to make stronger but more expensive metallic (mostly aluminium) closed cell foams. Within aluminium melts, gas bubbles can be created by injecting gas directly (e.g., Process of Cymat, Canada) or using a blowing agent (e.g., Process of Alporas, Japan). However, gas bubbles formed in metallic melts tend to rise to the free surface, a higher viscosity of the molten metal is needed to reduce the rising speed. A common technique consists in adding, for example, ceramic powders in the melt.

Another way to obtain metallic foams is to use a powder metallurgical method. Precursor materials are composed of metallic powders (e.g., aluminium alloy) and blowing agent powders (e.g., titanium hydride). The powder mix is at first consolidated by cold isostatic pressing and then followed by hot extrusion to form the desired shape. Foaming is carried out by heating at high temperature. One major advantage of this quite expensive method is the possibility to make final products directly without machining, for example, to put the powder mix between two skin sheets to make sandwich panels with foam cores directly.

The open cell metallic foam (sponge) is obtained by electro- or vapor-depositions on precursor open cell structures made of polymers. It can be also produced by an investment casting process.

1.4. Mechanical behaviour under quasi-static loading

1.4.1. Mechanical behaviour of honeycombs

For a regular cell cellular material, such as honeycomb (Fig. 1.3), it is easy to give a theoretical expression of its relative density, which is the ratio of the cross sectional area of the cell wall over the area occupied by the cell (1.2). The essential feature is that the relative density is proportional to the ratio of the wall thickness t over the cell length h. The change of the cell shape only influence the coefficient of proportionality.

$$\frac{\rho^*}{\rho_s} = \frac{3ht}{2h\cos\theta(h + h\sin\theta)} \propto \frac{t}{h}, \tag{1.2}$$

where ρ^*, ρ_s are the density of honeycomb and the density of the base material respectively.

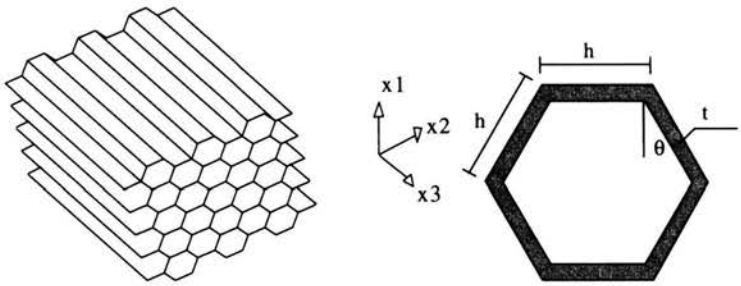

FIGURE 1.3. Honeycomb, idealised hexagonal cells.

(a) Out-of-plane behaviour (x3 direction)

Out-of-plane behaviour is the most interested property of honeycombs because of their favourable stiffness and strength in this direction. The ratio of the foam Young's modulus E_3^* over that of the base material and the yield stress σ_{y3}^{*+} in tension over the base material yield stress are equal to the relative density because the deformation is in an uniform stretching mode

$$\frac{E_3^*}{E_s} = \frac{\rho^*}{\rho_s}, \qquad \frac{\sigma_{y3}^{*+}}{\sigma_{ys}} = \frac{\rho^*}{\rho_s}, \tag{1.3}$$

where E_s, σ_{ys} denote Young's modulus and yield stress of the base material.

However, under compression, which is the loading scenario for energy absorption applications, the deformation mode is progressive folding of the cell

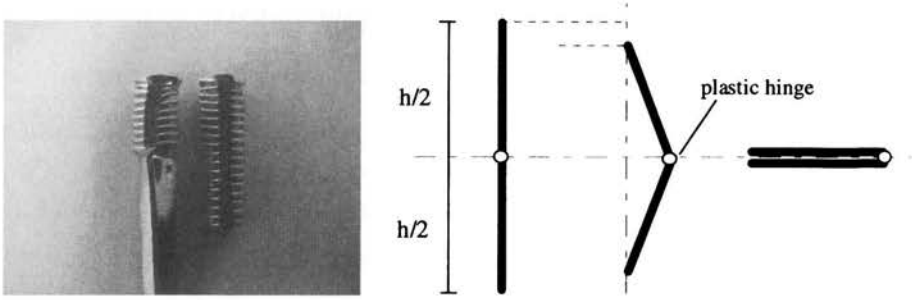

FIGURE 1.4. Progressive folding of cell walls, out-of-plane buckling.

wall. Its strength can be estimated using energy balance. Assuming that the half-wave length of folding is equal to the cell length h for simplicity (Fig. 1.4), an energy balance between the work of crushing force and total energy required in the rotation of the plastic hinge line can be made

$$\sigma_{y3}^{*-} 2h\cos\theta(h + h\sin\theta)h = \frac{1}{4}\sigma_{ys}t^2\pi 3h, \tag{1.4}$$

where σ_{y3}^{*-} is the compressive yield stress.

It leads to the following formula:

$$\frac{\sigma_{y3}^{*-}}{\sigma_{ys}} = \frac{\pi(h+2h)t^2}{8h\cos\theta(h+h\sin\theta)h} \propto \left(\frac{t}{h}\right)^2 \propto \left(\frac{\rho^*}{\rho_s}\right)^2. \tag{1.5}$$

For a cellular material with relative density of 0.1, the progressive folding strength is about 1/10 of its stretching strength.

(b) In-plane behaviour (x_1- or x_2-directions)

The in-plane deformation mode in linear elastic regime is elastic bending of sheets in microscopic scale. The relation is between the applied bending moment M and relative deflection δ

$$\delta = \frac{M}{6E_sI} = \frac{Fh\sin\theta}{12E_sI}, \tag{1.6}$$

where I denotes the moment of inertia of the cross section.

The bending moment is then related to the crushing force distribution (nominal stress σ_1 in x_1-direction) and the nominal strain ε_1 is propositional to the ratio of deflection δ over the cell length h:

$$M = \frac{1}{2}\sigma_1 h(1+\sin\theta)bh\sin\theta, \qquad \varepsilon_1 = \frac{\delta\sin\theta}{h\cos\theta}. \tag{1.7}$$

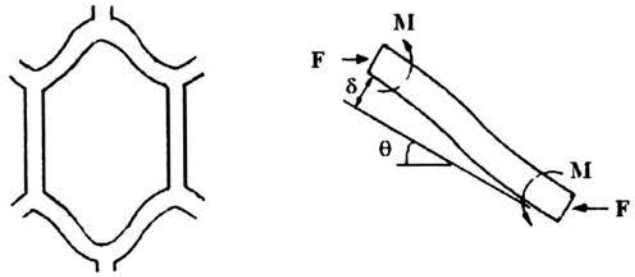

FIGURE 1.5. In-plane bending dominant deformation mode (after Gibson and Ashby, 1988).

>From Eqs. (1.6), (1.7), we obtain that the elastic moduli E_1^*, E_2^* in directions x_1 and x_2 (with similar analysis) scales with the cube of the relative density (1.8):

$$\frac{E_1^*}{E_s} = \left(\frac{t}{h}\right)^3 \frac{\cos\theta}{\sin^2\theta(1+\sin\theta)}, \quad \frac{E_2^*}{E_s} = \left(\frac{t}{h}\right)^3 \frac{(1+\sin\theta)}{\cos^3\theta}. \tag{1.8}$$

Yield stress can be obtained using the same analysis based on the energy balance as in the out-of-plane case, supposing the rotation angle ϕ is very small:

$$\sigma_{ys} t^2 b\phi = 2\sigma_{y1}^*(h + h\sin\theta)bh\phi\sin\theta. \tag{1.9}$$

It leads to the conclusion that the yield stresses $\sigma_{y1}^*, \sigma_{y2}^*$ in the directions x_1 and x_2 are proportional to the square of the relative density of the honeycomb:

$$\frac{\sigma_{y1}^*}{\sigma_{ys}} = \frac{1}{2(1+\sin\theta)\sin\theta}\left(\frac{t}{h}\right)^2, \quad \frac{\sigma_{y2}^*}{\sigma_{ys}} = \frac{1}{2\cos^2\theta}\left(\frac{t}{h}\right)^2. \tag{1.10}$$

1.4.2. Behaviour of foams

Foams do not have regular cell shapes and sizes as honeycombs and therefore, an accurate formula is impossible. However, a dimensional analysis can be made to understand the dependence of the main mechanical characteristics on the relative density.

(a) Open cell foams

For the open cell foams, an idealised cell structure is drawn in Fig. 1.6. The relative density is the ratio of the volume of cell edges over the volume occupied by the cell.

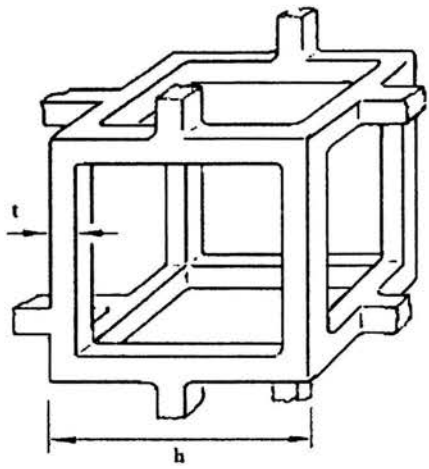

FIGURE 1.6. Idealised open cell foam model (after Gibson and Ashby).

It can easily be shown that the relative density is proportional to the square of the ratio of beam thickness t over cell size h:

$$\frac{\rho^*}{\rho_s} \propto \frac{t^2}{h^2}. \tag{1.11}$$

In the elastic range, the dominant deforming mode is bending as in the case of in-plane deformation of honeycomb, except that the basic elements are beams instead of plates. The elastic bending equation relates the applied force F and deflection δ (1.12), which leads to a relation between nominal strain ε and nominal stress σ:

$$\delta \propto \frac{Fh^3}{E_s I} \propto \frac{Fh^2}{E_s t^4} \quad \Rightarrow \quad \varepsilon \propto \frac{\delta}{h} \propto \frac{Fh^2}{E_s t^4} \propto \frac{\sigma h^4}{E_s t^4}. \tag{1.12}$$

The ratio of elastic modulus E^*over that of base material is proportional to the square of relative density:

$$\frac{E^*}{E_s} \propto \frac{t^4}{h^4} \propto \left(\frac{\rho^*}{\rho_s}\right)^2. \tag{1.13}$$

>From Fig. 1.7(b), the interested reader may estimate the value of the yielding stress by repeating the limit analysis:

$$\sigma_{ys} t^3 \frac{\delta}{h} \propto \sigma_y^* h^2 \delta. \tag{1.14}$$

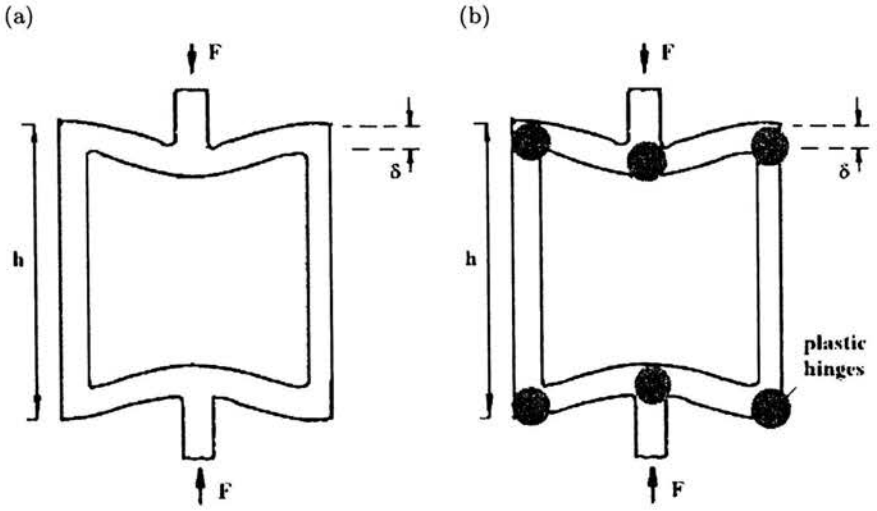

FIGURE 1.7. Deforming mode of open cell foams, elastic bending of edge beam (a), and plastic hinge rotation (b), (after Gibson and Ashby).

The yielding stress of open cell foams depends on the cube of square root of the relative density:

$$\frac{\sigma_y^*}{\sigma_{ys}^*} \propto \frac{t^3}{h^3} \propto \left(\frac{\rho^*}{\rho_s}\right)^{\frac{3}{2}}. \tag{1.15}$$

(b) Closed cell foam case

Closed cell foams are a combination of rather thick cell edges and much thinner cell membrane (Fig. 1.8) because of the manufacturing process (see Fig. 1.2). Microscopic observations of the deformation mode show that the edges and membranes are dominated by bending and stretching respectively.

The mechanical behaviour should also be a combination of these two kinds of deformation modes. Assuming that the weight percentage of edge part is φ and the membrane part is 1-φ, the elastic modulus depends then on the square of bending part and linearly on the stretching part:

$$\frac{E^*}{E_s} = C_1 \left(\varphi \frac{\rho^*}{\rho_s}\right)^2 + C_1'(1-\varphi)\frac{\rho^*}{\rho_s}, \tag{1.16}$$

where C_1, C_1' are coefficients, with values close to 1, according to experimental data on different foams.

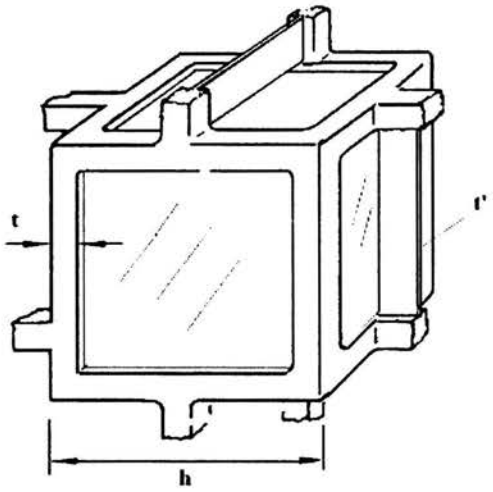

FIGURE 1.8. Idealised closed cell foams (after Gibson and Ashby).

It can also be easily deduced that the yield stress depends on the cube of the square root of bending part and linearly on the stretching part:

$$\frac{\sigma_y^*}{\sigma_{ys}} = C_2 \left(\varphi \frac{\rho^*}{\rho_s}\right)^{\frac{3}{2}} + C_2'(1-\varphi)\frac{\rho^*}{\rho_s}, \tag{1.17}$$

where C_2, C_2' are also coefficients and their experimental values are 0.3 and 0.4, respectively.

Chapter 2

Wave propagation in elastic and viscoelastic media

2.1. Introduction

Structures under impact loading are neither in an equilibrium state as under quasi-static loading, nor in a stationary motion state like vibrations. They are in a transient changing state depending on the wave propagation.

Therefore, to study the impact behaviour of cellular materials, the wave propagation knowledge is necessary to understand dynamic testing techniques as well as the analysis of impact response of structures involving cellular materials.

2.2. Elastic wave propagation in infinite media

For infinite media, the dynamic equilibrium equations are written as

$$\sigma_{ij,j} + f_i = \rho \frac{\partial^2 u_i}{\partial t^2}, \tag{2.1}$$

where ρ, σ_{ij}, u_i are the mass density, stress and displacement in the solid, respectively.

The assumption of small perturbations implies:

$$\varepsilon_{ij} = \frac{1}{2}\left(\frac{\partial u_i}{\partial x_j} + \frac{\partial u_j}{\partial x_i}\right). \tag{2.2}$$

The constitutive equation of the linear elastic solid is given by:

$$\sigma_{ij} = \lambda \varepsilon_{kk} \delta_{ij} + 2\mu \varepsilon_{ij}, \tag{2.3}$$

where λ and μ are the Lamé coefficients.

If the body force is neglected, the dynamic motion of elastic infinite media (2.2)-(2.2) is described by the Navier equations:

$$\mu\, u_{i,jj} + (\lambda + \mu) u_{j,ji} = \rho \ddot{u}_i \tag{2.4}$$

or

$$\mu \nabla^2 \mathbf{u} + (\lambda + \mu) \nabla \nabla . \mathbf{u} = \rho \ddot{\mathbf{u}}. \tag{2.5}$$

Here ∇ is the gradient operator.

Taking a natural decomposition of the displacement vector $\mathbf{u}$ into the dilatation part and distortion part, we write

$$\mathbf{u} = \nabla \phi + \nabla \times \mathbf{H}, \tag{2.6}$$

where ϕ is a scalar function and $\mathbf{H}$ a vectorial one.

Substituting (2.6) into Eq. (2.5), we get

$$\nabla \left[(\lambda + 2\mu) \nabla^2 \phi - \rho \ddot{\phi} \right] + \nabla \times \left[\mu \nabla^2 \mathbf{H} - \ddot{\mathbf{H}} \right] = 0. \tag{2.7}$$

This implies two wave propagation equations:

$$\frac{\partial^2 \phi}{\partial t^2} = \sqrt{\frac{\lambda + 2\mu}{\rho}}\, \nabla^2 \phi, \tag{2.8}$$

$$\frac{\partial^2 \mathbf{H}}{\partial t^2} = \sqrt{\frac{\mu}{\rho}}\, \nabla^2 \mathbf{H}. \tag{2.9}$$

Equation (2.8) defines the dilatation wave speed as $\sqrt{(\lambda + 2\mu)/\rho}$ and Eq. (2.9) gives the distortion wave speed equal to $\sqrt{\mu/\rho}$.

For a bounded domain, the dilatation wave reflects and transmits at the boundary to generate both dilatational and distortional waves; and so do the distortional waves. For a 3D boundary problem, there is no way to follow the wave propagations and interactions to get a simple analytical solution except for some simple cases.

2.3. One dimensional wave propagations

One-dimensional elastic wave propagation is a special case of the general wave equations and some interesting features of wave propagation can be explained. The governing equations are written in the following form:

$$\rho \frac{\partial^2 u}{\partial t^2} = \frac{\partial \sigma}{\partial x}, \qquad \varepsilon = \frac{\partial u}{\partial x}. \tag{2.10}$$

For a linear elastic behaviour we have

$$\sigma = E\varepsilon.$$

It leads to the one-dimensional elastic wave propagation equation:

$$\frac{\partial^2 u}{\partial t^2} = \frac{E}{\rho} \frac{\partial^2 u}{\partial x^2}. \tag{2.11}$$

Equation (2.11) admits the following general solution of displacement $u(x,t)$:

$$u(x,t) = f(C_0 t - x) + g(C_0 t + x), \tag{2.12}$$

where $C_0 = \sqrt{E/\rho}$ is the one-dimensional elastic wave speed, f and g are arbitrary functions (f is the wave propagating in the positive direction of x and g represents the wave in the opposite direction).

Let us consider a single wave (function f or g); Eq. (2.12) shows the time-space equivalence of these types of functions. It can be easily deduced that the stress $\sigma(x,t)$, strain $\varepsilon(x,t)$, and particle velocity $v(x,t)$ associated with one single wave are all proportional:

$$\sigma(x,t) = E\varepsilon(x,t), \qquad v(x,t) = \pm C_0 \varepsilon(x,t). \tag{2.13}$$

Another method to solve wave propagation is the characteristic equation and the jump condition. It is noted that Eq. (2.10) can be rewritten as a system of first order differential equations:

$$\begin{aligned} \frac{\partial \sigma}{\partial x} = \rho \frac{\partial v}{\partial t} \quad &\Longrightarrow \quad \frac{\partial}{\partial x}\left(\sigma - \rho v \frac{\partial x}{\partial t}\right) = 0, \\ \frac{\partial \sigma}{\partial t} = E \frac{\partial v}{\partial x} \quad &\Longrightarrow \quad \frac{\partial}{\partial x}\left(\sigma - E v \frac{\partial t}{\partial x}\right) = 0. \end{aligned} \tag{2.14}$$

It leads to the following characteristic equations, which sometimes are also called the jump condition:

$$d\sigma = \mp \rho C_0 dv \quad \text{at} \quad dx = \pm C_0 dt. \tag{2.15}$$

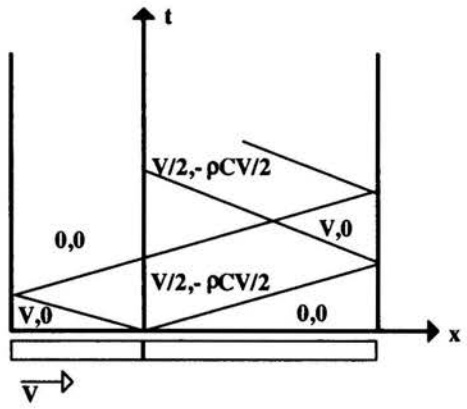

FIGURE 2.1. Collision between two thin rods.

As an example, let us consider now the wave propagation in a long thin bar generated by the impact of a shorter bar of the same size at a velocity of V (Fig. 2.1). The time-space diagrams (Lagrange diagram or x-t diagram) separate time-space region with the lines of a slope $\pm C_0$ (see Eq. (2.15)). The values of velocity and stress can be derived one by one from the jump condition (2.15) and boundary conditions.

2.4. Harmonic waves, wave dispersion in infinite elastic cylindrical bars

Harmonic waves are sinusoidal wave motions (Fig. 2.2) defined by the oscillating frequency ω, wave number ξ, and amplitude of vibration u_0:

$$u(x,t) = u_0 e^{i(\xi x - \omega t)}. \tag{2.16}$$

The wave speed C is calculated by the following formula:

$$C = \frac{\omega}{\xi}. \tag{2.17}$$

In the case of one-dimensional wave propagation, the general solution (2.12) can expressed as combinations of harmonic waves:

$$u(x,t) = \frac{1}{2\pi} \int \left(A(\omega) e^{i(\xi(\omega)x - \omega t)} + B(\omega) e^{i(\xi(\omega)x + \omega t)} \right) d\omega. \tag{2.18}$$

However, all the harmonic wave components should propagate with the same speed to ensure that wave profile does not change during propagation (non-dispersive wave).

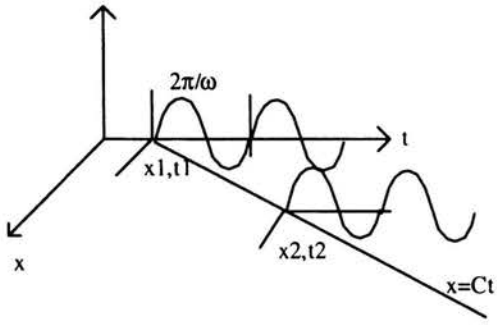

FIGURE 2.2. Harmonic wave motions.

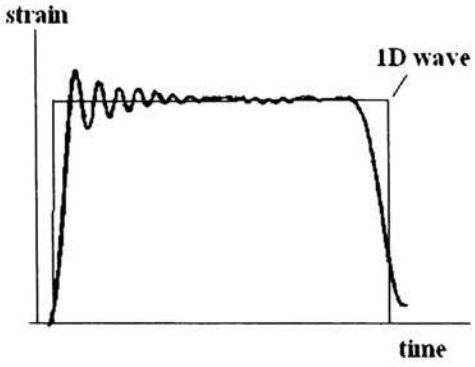

FIGURE 2.3. Wave dispersion effect.

Figure 2.3 shows the case of the wave profile generated by impact between two rods. The one-dimensional analysis gives a rectangular wave profile which is different from experimental recording. It can be concluded that the elastic wave in a rod is normally dispersive and one-dimensional theory is only a first-order approximation.

To describe this dispersive wave propagation Pochhammer (1876) and Chree (1889) derived a longitudinal wave solution for an infinite cylindrical elastic bar based on harmonic waves.

According to the propagation of harmonic waves, the displacement vector is written in the following form:

$$\mathbf{u}(\mathbf{X},t) = \frac{1}{2\pi}\int_{-\infty}^{+\infty} \mathbf{u}^*(\mathbf{X},\omega)e^{-i\omega t}d\omega$$
$$\text{with} \quad \mathbf{u}^*(\mathbf{X},\omega) = \mathbf{u}'^*(r,\theta,\omega)e^{i\xi(\omega)z}, \tag{2.19}$$

where $\mathbf{u}(\mathbf{X}, t)$, $\mathbf{u}^*(\mathbf{X}, \omega)$ are displacements as functions of time and frequency, respectively. The components of the space vector $\mathbf{X}$ are represented in cylindrical coordinates by r, θ, z, cf. Fig. 2.4.

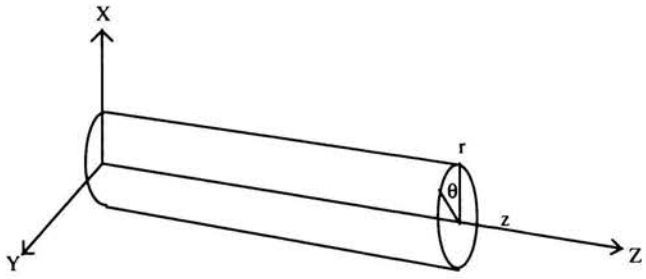

FIGURE 2.4. Cylindrical coordinates for infinite rod.

Substituting this displacement vector into wave equations (2.5), a general solution can be found. The boundary condition on the lateral surface of the cylindrical bar should be satisfied, i.e.,

$$\tau_{rr} = \tau_{r\theta} = \tau_{rz} = 0. \tag{2.20}$$

It will lead to the so-called Pochhammer–Chree's frequency equation that gives a relation between the wave number ξ and the frequency ω (Pochhammer, 1876; Chree, 1889). Detailed development is given in the following (for an infinte viscoelastic bar).

2.5. Wave propagation in infinite viscoelastic cylindrical bars

2.5.1. Viscoelastic frequency equation

In the case of a linear viscoelastic bar, a similar harmonic wave solution can be obtained. Considering a linear viscoelastic media, the constitutive law can be written in the frequency domain as follows (Bland, 1960):

$$\boldsymbol{\sigma}^*(\omega) = \lambda^*(\omega)\,\mathrm{tr}\left(\boldsymbol{\varepsilon}^*(\omega)\right)\mathbf{1} + 2\mu^*(\omega)\,\boldsymbol{\varepsilon}^*(\omega), \tag{2.21}$$

where $\boldsymbol{\sigma}^*$, $\boldsymbol{\varepsilon}^*$, and λ^* and μ^* are respectively the stress tensor, the strain tensor, and two material coefficients.

The harmonic wave displacement components $\mathbf{u}^*(\mathbf{X},\omega)$ must satisfy the following dynamic equation of motion (Achenbach, 1978):

$$\mu^*(\omega)\nabla^2\mathbf{u}^*(\mathbf{X},\omega) + \big(\lambda^*(\omega)+\mu^*(\omega)\big)\nabla\nabla\cdot\mathbf{u}^*(\mathbf{X},\omega) = -\rho\omega^2\mathbf{u}^*(\mathbf{X},\omega), \quad (2.22)$$

where ∇ is the gradient operator and ρ is the mass density.

As in the case of elastic media (Graff, 1975), each wave displacement $\mathbf{u}^*(\mathbf{X},\omega)$ can be expressed as a function of the dilatational wave part $\phi^*(\mathbf{X},\omega)$ and distortional wave part $\mathbf{H}^*(\mathbf{X},\omega)$:

$$\mathbf{u}^*(\mathbf{X},\omega) = \nabla\phi^*(\mathbf{X},\omega) + \nabla\times\mathbf{H}^*(\mathbf{X},\omega). \quad (2.23)$$

Substituting Eq. (2.23) into the dynamic equation of motion (2.22), we get:

$$\begin{aligned}\nabla^2\phi^*(\mathbf{X},\omega) + \frac{\omega^2}{C_1^2}\phi^*(\mathbf{X},\omega) = 0,\\ \nabla^2\mathbf{H}^*(\mathbf{X},\omega) + \frac{\omega^2}{C_2^2}\mathbf{H}^*(\mathbf{X},\omega) = 0,\end{aligned} \quad (2.24)$$

with

$$C_1 = \sqrt{\frac{\lambda^*(\omega)+2\mu^*(\omega)}{\rho}}, \qquad C_2 = \sqrt{\frac{\mu^*(\omega)}{\rho}}.$$

This equation must be satisfied, respectively, by the dilatational and the distortional parts of the displacement (Zhao, 1992).

For an infinite cylindrical bar, the assumption of the harmonic wave (2.19) means that the displacement must show a sinusoidal variation along the axial direction of the bar. The solutions $\phi^*(\mathbf{X},\omega)$ and $\mathbf{H}^*(\mathbf{X},\omega)$ are then expressed in the following form:

$$\begin{aligned}\phi^*(\mathbf{X},\theta,\omega) &= \varphi(r,\omega)e^{i\xi z},\\ \mathbf{H}^*(\mathbf{X},\omega) &= \Big[h_r(r,\theta,\omega)\,\mathbf{e}_r + h_\theta(r,\theta,\omega)\,\mathbf{e}_\theta + h_z(r,\theta,\omega)\,\mathbf{e}_z\Big]e^{i\xi z}.\end{aligned} \quad (2.25)$$

Furthermore, in the case of longitudinal wave, owing to the axi-symmetry of the problem, the functions $\phi^*(\mathbf{X},\omega)$ and $\mathbf{H}^*(\mathbf{X},\omega)$ are written in a simpler form:

$$\begin{aligned}\phi^*(\mathbf{X},\omega) &= \varphi(r,\omega)e^{i\xi z},\\ \mathbf{H}^*(\mathbf{X},\omega) &= h_\theta(r,\omega)\,e^{i\xi z}\mathbf{e}_\theta.\end{aligned} \quad (2.26)$$

Replacing $\phi^*(\mathbf{X},\omega)$ and $\mathbf{H}^*(\mathbf{X},\omega)$ in Eq. (2.26) by those given in Eq. (2.26), the functions $\varphi(r,\omega)$ and $h_\theta(r,\omega)$ can be determined. Then, we have:

$$\begin{aligned} \phi^*(\mathbf{X},\omega) &= A(\omega)J_0(\alpha r)e^{i\xi z}, \\ \mathbf{H}^*(\mathbf{X},\omega) &= B(\omega)J_1(\beta r)e^{i\xi z}, \end{aligned} \tag{2.27}$$

where

$$\alpha^2 = \frac{\rho\omega^2}{\lambda^*(\omega)+2\mu^*(\omega)} - \xi^2, \qquad \beta^2 = \frac{\rho\omega^2}{\mu^*(\omega)} - \xi^2. \tag{2.28}$$

Here J_0 and J_1 are zero and first order Bessel's functions, while $A(\omega)$ and $B(\omega)$ are coefficients.

The displacement can then be calculated from equation (2.23). The strain and the stress tensors are found by using Eq. (2.21). The homogeneous boundary conditions at the external surface of the bar ($r = a$), which must be satisfied by the solution (2.27), lead to an equation relating ξ and ω. A "viscoelastic frequency equation" is then obtained. This equation takes the same form as in the classical elasticity. However, in the present case the argument ξ in the equation is a complex number (Zhao, 1992):

$$\begin{aligned} f(\xi) = {} & (2\alpha/a)(\beta^2+\xi^2)J_1(\alpha.a)J_1(\beta.a) \\ & - (\beta^2-\xi^2)^2 J_0(\alpha.a)J_1(\beta.a) - 4\xi^2\alpha.\beta.J_1(\alpha.a)J_0(\beta.a) = 0. \end{aligned} \tag{2.29}$$

In this equation, ξ is a complex function of the frequency ω. Its real part gives the relation between frequency and associated phase velocity whilst the imaginary part gives the relation between frequency and associated attenuation coefficient.

2.5.2. Numerical resolution method

The harmonic wave propagation in an infinite cylindrical rod was studied in the elastic case (Bancroft, 1941; Davies, 1948; Mindlin and McNiven, 1960), where numerical results were also given.

In the case of viscoelastic rod, the explicit relation $\xi(\omega)$ has to be found numerically from equation (2.30) by solving a non-linear two-dimensional optimisation problem:

$$\begin{aligned} \mathrm{Re}\left[f\big(\mathrm{Re}(\xi),\mathrm{Im}(\xi)\big)\right] &= 0, \\ \mathrm{Im}\left[f\big(\mathrm{Re}(\xi),\mathrm{Im}(\xi)\big)\right] &= 0, \end{aligned} \tag{2.30}$$

where Re and Im denote the real and imaginary parts of complex number.

It could be difficult to obtain a very accurate solution of such a system. Fortunately, in our case the complex derivative $f'(\xi)$ can be calculated analytically, and an iterative formula of Newton type generalised to the case of complex variables is constructed:

$$\xi_{n+1} = \xi_n - \frac{f(\xi_n)}{f'(\xi_n)}. \tag{2.31}$$

The convergence of this method depends on the initial value ξ_0 of the argument. For a given frequency ω, different values of ξ are found as analytical solutions of Eq. (2.29). The procedure is similar to the elastic wave propagation where different "modes" are found (Davies, 1948). Assuming that only the first order solution (corresponding to the lowest velocity) is needed for the dispersion correction, the initial estimate ξ_0 is taken as the solution of the one-dimensional wave propagation equation:

$$\xi^2(\omega) = \frac{\rho\omega^2}{E^*(\omega)}, \tag{2.32}$$

where $E^*(\omega)$ is the complex modulus.

Chapter 3

Rate sensitivity of cellular materials

3.1. Rate sensitivity derived from base materials

In the micromechanical analyses developed in Chapter 1 the ratio of cellular material strength over that of the cell wall material depends on a certain power function of the relative density. It takes into account only the rate sensitivity of the cell wall material and the rate sensitivity of foam should be the same as of the base material. However, it is extremely difficult to determine accurately the local strain rate because of the deformation localisation and the average strain rate always under-estimates the actual strain rate. It is also difficult to know exactly the cell wall material behaviour because the material compositions in the skin and edge of the foam may be quite different from base polymers or metals.

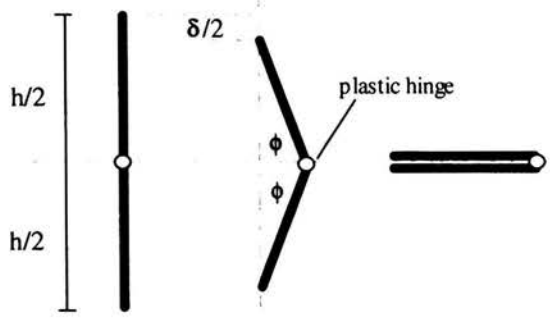

FIGURE 3.1. Honeycomb crushing.

An approximate relation between the strain rate of cell wall material and the nominal strain rate of cellular material can be however evaluated. Taking the honeycomb loaded in the x_3-direction, as an example (Fig. 3.1), we assume that the deformation mode is a progressive folding with the wave length of about h.

Assume that the specimen has the length L, the nominal cellular material strain rate $\dot{\varepsilon}_N$ is proportional to the crushing rate $\dot{\delta}$:

$$\dot{\varepsilon}_N = \frac{\dot{\delta}}{L}$$

The geometrical relation of the bending system in Fig. 3.1 yields:

$$\dot{\delta} = h\dot{\phi}\cos\phi. \tag{3.1}$$

Thus, the nominal honeycomb strain rate is related to the angle changing rate $\dot{\phi}$. On the other hand, the strain rate of base material in the plastic hinge can be approximately related to this angle changing rate $\dot{\phi}$. With the assumption that a plastic hinge length is about four times the thickness, the mean curvature change rate $\dot{\kappa}$ is $\dot{\phi}/4t$.

The mean stretching strain rate on the external surface of the plastic hinge is estimated by the following formula:

$$\dot{\varepsilon}_{\text{base}} = \frac{\dot{\kappa}t}{2} = \frac{\dot{\phi}}{8}. \tag{3.2}$$

Equations (3.1) and (3.2) provide a relationship between the strain rates in the cell wall material and in honeycomb:

$$\dot{\varepsilon}_{\text{base}} = \frac{\dot{\phi}}{8} = \frac{L}{8h\cos\phi}\,\dot{\varepsilon}_N. \tag{3.3}$$

If the length of the specimen L is about 10 times cell buckling length h, in a reasonable range of the angle ϕ (from 90° to 36° corresponding to a locking strain of about 0.6), the coefficient between the strain rate of cell wall material and the nominal honeycomb strain rate ranges from 1 to 2.

Unfortunately, such a simple analysis cannot explain all the experimental observations. There are other explanations which are discussed in the following Sections.

3.2. Pressure increase of the air entrapped in the cell

Strain rate sensitivities may be also due to the existence of the gas/fluid phase (Gibson and Ashby, 1988; Deshpande and Fleck, 2000a). Taking an open cell foam as an example, when the foam is loaded very slowly, the gas filled in the foam will escape without resistance (it becomes another problem if the foam is filled with viscous incompressible fluids). Under high speed impact, the gas entrapped in the foam may have no time to move out. They will then take part in the foam resistance by the increase of pressure due to the volume change. Evidently, the quicker the loading is, the more the air is entrapped. The enhancement of the foam strength with the loading rate can be partially explained by this assumption.

The importance of this supplementary air pressure can be easily evaluated by the gas volume change. Assuming that the gas occupies initially all the foam volume V subtracted by the solid skeleton volume, the initial gas volume V_0^{gas} is then

$$V_0^{\text{gas}} = V_0\Big(1 - \frac{\rho^*}{\rho_s}\Big), \tag{3.4}$$

where V_0 is the initial volume of the foam.

In the range of large crushing strains, the lateral expansion is generally rather small and difficult to quantify. Here we neglect this lateral expansion, knowing that this will slightly overestimate the volume change. The actual foam volume V can simply be expressed as follows

$$V = V_0(1 - \varepsilon). \tag{3.5}$$

The volume change of the solid phase is supposed to be negligible so that all the volume change is attributed to the gas phase. Under the assumption that all the air is totally trapped to get an upper limit, the actual volume occupied by gas is

$$V^{\text{gas}} = V_0(1 - \varepsilon - \frac{\rho^*}{\rho_s}). \tag{3.6}$$

Supposing the loading is done under adiabatic condition, the actual pressure of gas is

$$P^{\text{gas}} = P_0^{\text{gas}} \left(\frac{V_0^{\text{gas}}}{V^{\text{gas}}}\right)^{\gamma}, \tag{3.7}$$

where P^{gas}, P_0^{gas} denote actual and initial air pressure.

The contribution of the air pressure for the foam strength is given by the following equation:

$$\Delta P^{\text{gas}} = P_0^{\text{gas}} \left[\left(\frac{V_0^{\text{gas}}}{V^{\text{gas}}} \right)^{\gamma} - 1 \right]. \tag{3.8}$$

It yields:

$$\Delta P^{\text{gas}} = P_0^{\text{gas}} \left[\left(\frac{1 - \frac{\rho^*}{\rho_s}}{1 - \varepsilon - \frac{\rho^*}{\rho_s}} \right)^{\gamma} - 1 \right]. \tag{3.9}$$

>From Eq. (3.9), for a foam of 0.1 relative density with air (specific coefficient of 1.4), one can deduce that the amplitude of contribution of air pressure is around 2 times the initial pressure at 50% of strain (only 0.1 times at 10% strain). The upper limit of air pressure is about 0.2 MPa. Such influence should be taken into account only for very weak cellular structures, for example, in the case of low density open cell polymeric foams. It can be neglected in most cases, especially for metallic core materials such as aluminium honeycombs and foams.

3.3. Micro-inertia effect

Micro-inertia is another factor that may cause overall strain rate effect. It is known that the lateral inertia may cause a significant strength enhancement in a buckling problem. The early fundamental work in this domain was reported by Budiansky and Hutchinson (1964). It is experimentally shown that the buckling of a column under compressive impact occurs later because of lateral inertia, so that the apparent critical buckling force is higher than static one because of strain hardening (Gary, 1983). Other known works (Calladin and English, 1984; Tam *et al.*, 1991) explain in detail the role played by the lateral inertia. They developed simple models describing the buckling and post buckling behaviour of simple column under impact loading.

3.3.1. Simple rigid plastic model

To recall the basic idea without mathematical details, let us consider a simple model made of 2 rigid plastic bars linked by a plastic hinge and a concentrated mass in the middle (Fig. 3.2).

This mechanical system is well defined and the following geometrical relationship holds:

$$-\delta v = L \sin\theta \, \delta\theta. \tag{3.10}$$

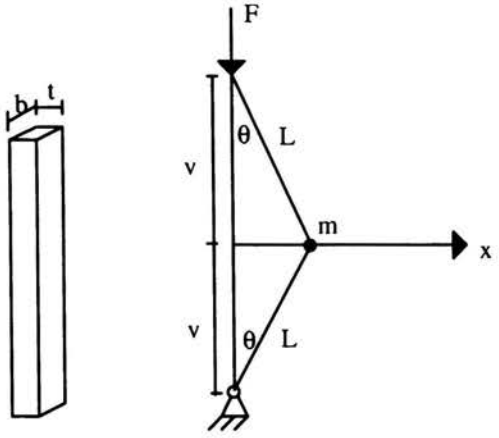

FIGURE 3.2. Rigid plastic models for lateral inertia.

Under static loading, the system will crash (the angle θ will increase rapidly) once the maximum moment due to the applied force F overcomes the fully plastic moment of the plastic hinge M_p:

$$M_p = b\,t^2 \frac{\sigma_s}{4}. \tag{3.11}$$

It leads to an estimate of the crushing force:

$$F = -M_p \frac{2\delta\theta}{2\delta v} = \frac{\sigma_s b t^2}{4L\sin\theta}. \tag{3.12}$$

The initial imperfection (deviation from a vertically straight position) is characterized by the angle θ. If the angle is zero, there will be no buckling but only compression. For a reasonable small angle, the buckling peak load is close to the product of the flow stress with the cross sectional area.

However, when the model is loaded at higher speeds, the problem is that the concentrated mass in the middle is initially at rest and its acceleration is limited by the following equation:

$$m\ddot{x} = 2\sigma_s b t \sin\theta. \tag{3.13}$$

It means that the concentrated mass will be accelerated progressively from zero to the speed corresponding to the loading impact velocity. During this period of acceleration, the crushing displacement is mostly compression of rigid plastic bars. Thus, before the mass is accelerated to an important velocity, the buckling can not take place. It should be noted that the initial

imperfection play a very important role here. The smaller the angle is, the smaller is the accelerating force so that the acceleration duration (or inertia protection duration) will be longer and the strain reached before buckling higher.

Consequently, the basic difference between static and dynamic loading is the compressive strain reached before bending. For a strain hardening material, a difference of buckling forces will be observed because under impact loading the column is more compressed. It explains why the dynamic buckling peak load appears higher.

3.3.2. Inertia sensitive structures

Such a basic concept is accepted by a number of authors and applied in several structural cases. For example, Langseth *et al.* (1996, 1999) claim that the lateral inertia is a cause of the strength increase observed in steel and aluminium square tubes. Su *et al.* (1995) provided a classification of different structures which are rate sensitive or not.

They found that structures having a quite flat force-displacement diagramme after yield point (classified as type I) present very limited rate sensitivity. The typical example is the traversal compression of circular tubes.

In contrast, structures classified as type II have a sharp drop of the crushing force after a critical loading point and rate sensitivity is observed in such structures. The buckling of a straight beam is a good example of type II structure.

As a matter of fact, the key point is whether there exists a branching point between two possible deforming modes during the crushing. When this branching point exists the inertia under impact loading may change the oc-

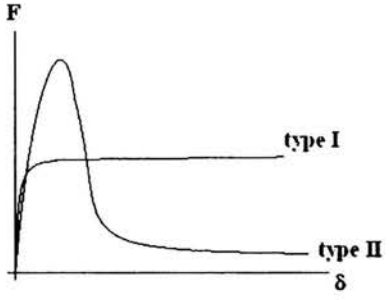

FIGURE 3.3. Inertia sensitive structure classifications.

curring chance for each particular deforming mode. Taking example of beam buckling, the lateral inertia under impact maintains the deforming mode of uniform compression because the bending becomes impossible, even though the compression needs more energy.

Such a selector effect is very clear in a polymer composite plate test, see Fig. 3.4.

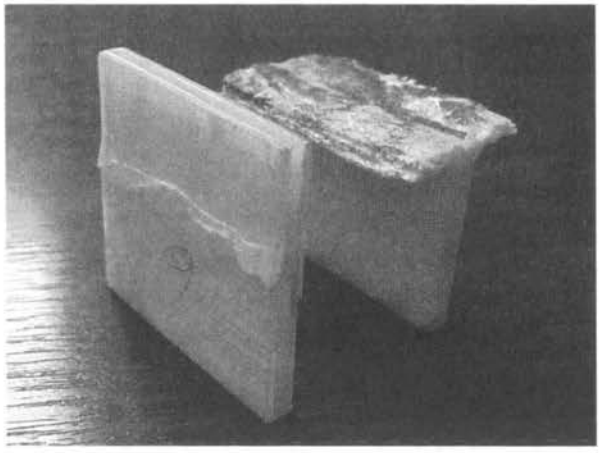

FIGURE 3.4. Deforming mode selections (an example).

During the static loading, the microbuckling is the least energy demanding deforming mode (on the left of the photograph). Under impact loading, the splitting becomes possible because microbuckling is locked by lateral inertia. Nice works on the strength enhancement in fiber composite have been reported by the team of G. Ravichandran (Oguni and Ravichandran, 2000, 2001).

Another example of deforming mode selection example can be found in balsa wood. In a progressive folding, the mean crushing strength depends strongly on the wave-length. The shorter the wave length is, the higher the crushing strength. In the case of balsa wood it can be seen, for example, that the locking strain under impact is smaller than that in the static case and this indicate that the folding wave-length becomes smaller (Vural and G. Ravichandran, 2003).

Such a wave length in the case of prism hollow box can be estimated by the minimisation of the energy needed for crushing. However, if perturbed, the wave length will change. For example, the prism tube filled with foam

deforms with a different wave length from the initial hollow tube (Langseth *et al.*, 1996). It was also shown that when the impact velocity is high enough, the wave-length in the folding is modified by stress wave propagation (Karagiozova *et al.* 2000).

3.4. Shock wave effect under hyper-velocity impact

3.4.1. Shock wave forming

For the sake of simplicity, the shock wave is introduced in the one-dimensional case, where the governing equations is written as follows:

$$\rho \frac{\partial^2 u}{\partial t^2} = \frac{\partial \sigma}{\partial x}. \tag{3.14}$$

The behaviour of an arbitrary solid can be described by a differentiable stress-strain function:

$$\sigma = f(\varepsilon). \tag{3.15}$$

Substituting (3.15) into (3.14) yields

$$\frac{\partial^2 u}{\partial t^2} = \frac{1}{\rho}\frac{d\sigma}{d\varepsilon}\frac{\partial \varepsilon}{\partial x} = \frac{1}{\rho}\frac{d\sigma}{d\varepsilon}\frac{\partial^2 u}{\partial x^2}. \tag{3.16}$$

Equation (3.16) implies that wave propagates at wave speeds varying with the strain or stress level:

$$C(\varepsilon) = \sqrt{\frac{1}{\rho}\frac{d\sigma}{d\varepsilon}}. \tag{3.17}$$

In the case where the function $\sigma = f(\varepsilon)$ is convex as for a usual elastic-plastic solid, the wave speed decreases with the strain and wave disperse on propagating. In the case where the function $\sigma = f(\varepsilon)$ is concave, the wave speed increases with the strain so that early created waves at small strain propagate at lower speeds than those generated later. The latter will somehow catch the former waves during propagation and a single shock wave front is inevitable.

Such kind of concave constitutive function is quite unusual for solid materials, except under high pressure (several GPa). For example, in the plate impact test mentioned later on in Sec. 4.4 (the interested reader can also refer to Meyers, 1994), the shock wave is generated at high pressure due to the existence of concave pressure-volume relation. For a cellular material, the densification part of the stress-strain curve is a concave function and the shock wave may be formed under the usual one-dimensional condition.

3.4.2. Conservation laws through shock front

Let us consider a one-dimensional plane shock wave shown in Fig 3.5. Before the shock front arrives, the material state is given by the density ρ_0, particle velocity v_0, stress σ_0, and the internal energy E_0. Behind the shock front, the material is described by another state ρ_1, v_1, σ_1, E_1.

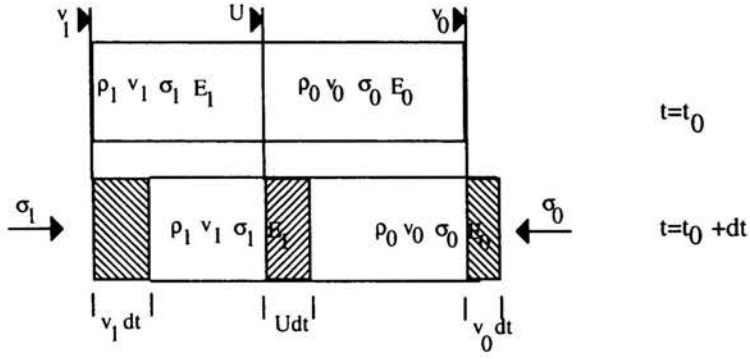

FIGURE 3.5. Conservation laws through shock front.

Conservation laws should be satisfied. For the conservation of mass, the balance of mass for a short time dt is as follows:

$$dM = S\big[-v_1\,dt\,\rho_1 + v_0\,dt\,\rho_0 + U\,dt\,(\rho_1 - \rho_0)\big] = 0. \tag{3.18}$$

It yields:

$$\rho_1(U - v_1) = \rho_0(U - v_0). \tag{3.19}$$

The balance of kinematical quantities for the time period dt is:

$$S\,(\sigma_1 - \sigma_0)\,dt = S\big[-v_1\,dt\,\rho_1 v_1 + v_0\,dt\,\rho_0 v_0 + U\,dt\,(\rho_1 v_1 - \rho_0 v_0)\big]. \tag{3.20}$$

Substituting the mass conservation law into Eq. (3.20) we obtain

$$\sigma_1 - \sigma_0 = \rho_0(U - v_0)(v_1 - v_0). \tag{3.21}$$

Similarly, the energy conservation law is obtained in the form

$$E_1 - E_0 = \frac{1}{2}(\sigma_1 + \sigma_0)\left(\frac{1}{\rho_1} - \frac{1}{\rho_0}\right). \tag{3.22}$$

3.4.3. Shock enhancement of cellular materials

Shock wave can be formed in cellular materials when a very high velocity impact is applied. Indeed, when the foam reaches the locking strain, the constitutive equation becomes concave and the shock front can be formed. Reid and Peng (1997) considered a simple model case of foam material crushing against a rigid wall, see Fig. 3.6.

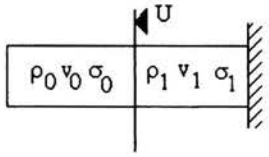

FIGURE 3.6. Foam shock wave model.

Assuming that the foam behaviour can be approximated by rigid-plastic-rigid-locking model (Reid and Peng, 1997), see Fig. 3.7, a unique shock front propagation at velocity U will be formed.

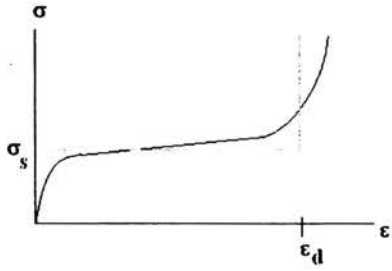

FIGURE 3.7. Simplification of cellular material behaviour (after Reid and Peng, 1997.)

The boundary conditions are given by

$$v_0 = V, \qquad v_1 = 0. \tag{3.23}$$

The stress ahead of shock front is the plastic flow stress of foams σ_s and the stress behind shock front is the so-called shock enhanced stress σ_d:

$$\sigma_0 = \sigma_s, \qquad \sigma_1 = \sigma_d. \tag{3.24}$$

Using this simplified rigid locking model, the density behind shock wave is given by

$$\rho_1 = \frac{\rho_0}{1 - \varepsilon_d}, \tag{3.25}$$

where ε_d denotes the locking strain.

The mass conservation (3.19) leads to:

$$\rho_1 U = \rho_0 (U - V). \tag{3.26}$$

It provides an explicit expression of the shock wave speed U:

$$U = \frac{1 - \varepsilon_d}{\varepsilon_d} V. \tag{3.27}$$

Substituting (3.26) into the conservation of kinetical quantities (3.21) leads to:

$$\sigma_1 - \sigma_0 = \rho_1 UV = \frac{\rho_0}{1 - \varepsilon_d} UV. \tag{3.28}$$

Taking account of Eq. (3.27) we have:

$$\sigma_1 - \sigma_0 = \frac{\rho_0 V^2}{\varepsilon_d}. \tag{3.29}$$

The shock enhancement is finally written as follows:

$$\sigma_d = \sigma_s + \frac{\rho_0 V^2}{\varepsilon_d} \quad \text{or} \quad \frac{\sigma_d}{\sigma_s} = 1 + \frac{\rho_0 V^2}{\varepsilon_d \sigma_s}. \tag{3.30}$$

We observe that the enhancement exists under particular condition of the shock front forming. The stress calculated from Eq. (3.30) can not be considered as material characteristics and the energy absorption under this shock enhancement is still an open question. Therefore, it should not be applied simply to the energy absorption design.

Chapter 4

Introduction of impact testing techniques

4.1. High speed testing machine

One of the commonly used impact testing devices is the high speed hydraulic testing machine. It differs from an ordinary hydraulic testing machine, since high delivery hydraulic pressure generator combined with accumulators of air pressure is required (Fig. 4.1). It should be emphasized that such machines provides only a single impact at a given initial speed (up to 20 m/s). It is impossible to control other parameters of loading (holding, unloading) as in a static testing machine. The force measurement is usually done by a load cell mounted at the top of the machine.

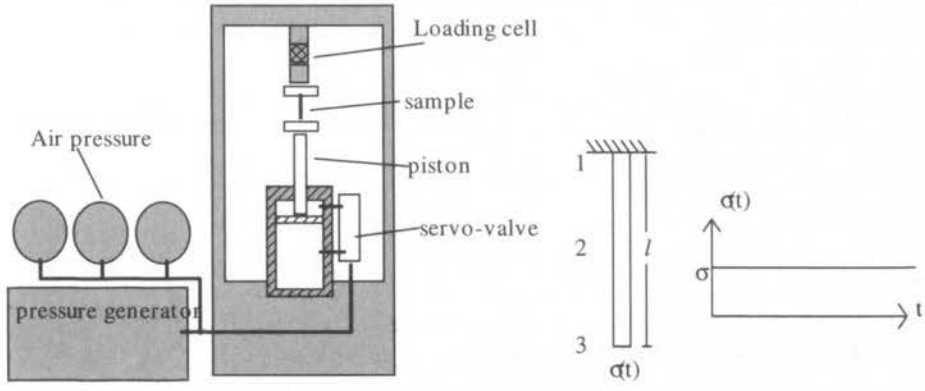

FIGURE 4.1. High velocity testing machine.

This testing configuration raises the measuring difficulty because the recording sensor can not be put in contact with the sample. If the top column is assumed thin enough, it can be considered as a one-dimensional elastic bar subjected to a sudden impact force applied at the column end by the loaded sample (Fig. 4.1, on the right). Using the boundary and jump conditions for one-dimensional elastic waves (2.15), the stress and the particle velocity can be calculated for three positions:

1. at the top of the column,
2. at the middle,
3. at the contact interface with the sample.

The stress and particle velocity time histories are shown in Fig. 4.2. These time-histories are different. We observe that the average stress and velocities are similar. Thus, if the test is slow and a small sampling rate is required, one can have just one sample point in one oscillating period to measure accurately the mean value at any position. However, if a high velocity test is made and a high sampling rate is necessary, the recording profile at the position 2 is absolutely different from the signal at the position 1.

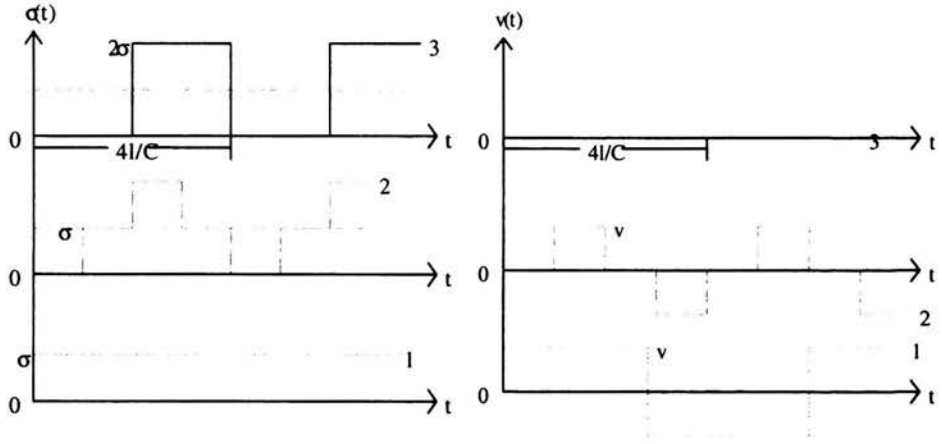

FIGURE 4.2. Analysis of loading measurement.

4.2. Weight drop hammer

The weight drop device is another very popular impact testing methods. As shown in Fig. 4.3, a compact mass guided in a rail falls and hits the

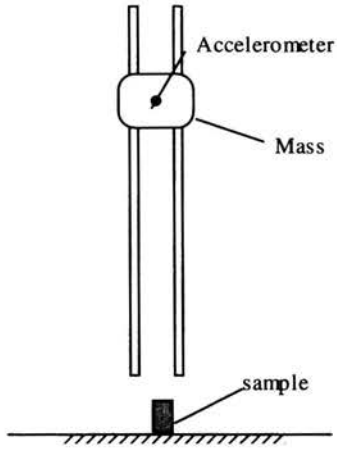

FIGURE 4.3. Drop weight testing device.

sample. The deceleration of that mass is measured by an accelerometer. The associated force and displacement are then found. The recorded accelerometer signal is not always of sufficient quality because of vibrations of the weight and of its guiding rail or suspension system. Draconian but not justified filtering has to be processed to get acceptable curves.

4.3. Split Hopkinson Pressure Bar

4.3.1. Experimental setup

The SHPB (Split Hopkinson Pressure Bar), also called the Kolsky apparatus, is a commonly used experimental technique to study constitutive laws of materials at high strain rates. (Hopkinson, 1914; Kolsky, 1949, 1963). A typical SHPB, shown in Fig. 4.4, is composed of the long input and output bars with a short specimen placed between them. The impact between

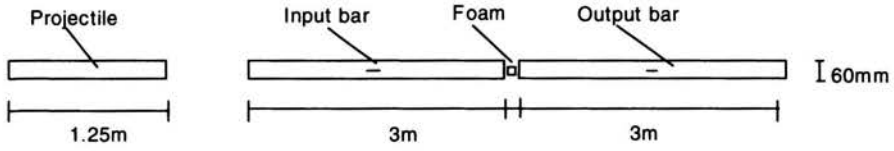

FIGURE 4.4. Split Hopkinson Pressure Bar setup.

the projectile and the input bar generates a compressive longitudinal incident pulse $\varepsilon_i(t)$ in the input bar. Once this incident pulse reaches the specimen-bar interface, a reflected pulse $\varepsilon_r(t)$ in the input bar and a transmitted pulse $\varepsilon_t(t)$ in the output bar are developed. With strain gauges fixed to the input and output bars, one can record those three pulses that allow for the determination of the forces and particle velocities at both faces of the specimen.

The conventional analysis is based on the mechanics of the elastic wave propagation in bars. According to the theory of elastic wave propagation, the stress and particle velocity of a single wave can be accurately determined from the associated strain (2.13) measured by strain gages.

4.3.2. Analysis of SHPB

The standard SHPB analysis is based on two assumptions. First, it is assumed that the wave profiles are not only known at the measuring points but everywhere in the bar because an elastic wave can be shifted to any locations according to the uniaxial elastic wave propagation theory. Thus, the transmitted wave can be shifted to the output bar-specimen interface to obtain the output force and velocity, whereas the input force and velocity can be determined via the incident and reflected waves shifted to the input bar-specimen interface.

The forces and the velocities at both faces of the specimen are then given by the following equations:

$$\begin{aligned} F_{\text{input}}(t) &= S_B E \left[\varepsilon_i(t) + \varepsilon_r(t)\right], \\ F_{\text{output}}(t) &= S_B E\, \varepsilon_t(t), \\ V_{\text{input}}(t) &= C_0 \left[\varepsilon_i(t) - \varepsilon_r(t)\right], \\ V_{\text{output}}(t) &= C_0 \varepsilon_t(t), \end{aligned} \tag{4.1}$$

where F_{input}, F_{output}, V_{input}, V_{output} are forces and particle velocities at the interfaces; S_B, E, C_0 are the cross sectional area of the bars, Young's modulus, and the longitudinal wave speed, and $\varepsilon_i(t)$, $\varepsilon_r(t)$, $\varepsilon_t(t)$ are the waves known at the bar-specimen interface.

Secondly, from forces and velocities at both bar-specimen interfaces, the standard analysis assumes the axial uniformity of stress and strain fields in the specimen, and thus, the stress strain curve can be obtained (like those

obtained from quasi-static test):

$$\dot{\varepsilon}_s(t) = \frac{V_{\text{output}}(t) - V_{\text{input}}(t)}{l_s}, \tag{4.2}$$

$$\sigma_s(t) = \frac{F_{\text{output}}(t)}{S_s}. \tag{4.3}$$

Equations (4.2), (4.3) give the usual two-waves formula of Split Hopkinson Pressure Bar test:

$$\begin{aligned} \varepsilon_s(t) &= \frac{2C_0}{l_s} \int_0^t \varepsilon_r(t)\, d\tau, \\ \dot{\varepsilon}_s(t) &= \frac{2C_0}{l_s} \varepsilon_r(t), \\ \sigma_s(t) &= \frac{S_B E}{S_s} \varepsilon_t(t). \end{aligned} \tag{4.4}$$

As such a homogeneous assumption is not really correct under dynamic loading, at least at the early stage of the test because of the transient effects: the loading starts at one face of the specimen whereas the other faces remain at rest. Investigations on this point were reported by Conn (1965), Hauser (1966) and Jahsman (1971), using a one-dimensional simulation of the wave propagation in the specimen. A two-dimensional numerical simulation was given by Bertholf and Karnes (1975). Experimental observations of the strain field using the diffraction grating technique were reported by Bell (1966). It has been proved that stresses and strains are not axially uniform, especially at the early stage of the test. However, such analyses become quite realistic after a great number of wave reflections in the specimen when a short metallic specimen is tested.

A three-waves analysis has been proposed to use the average of the two forces to calculate the stress (4.2) instead of Equation (4.3) (Lindhlom, 1964).

$$\sigma_s(t) = \frac{F_{\text{input}}(t) + F_{\text{output}}(t)}{2S_s}. \tag{4.5}$$

It leads to the following three wave SHPB formulas:

$$\begin{aligned} \sigma_s(t) &= \frac{S_B E}{2S_s} \left[\varepsilon_t(t) + \varepsilon_r(t) + \varepsilon_i(t)\right], \\ \dot{\varepsilon}_s(t) &= \frac{C_0}{l_s} \left[\varepsilon_t(t) + \varepsilon_r(t) - \varepsilon_i(t)\right], \end{aligned} \tag{4.6}$$

$$\varepsilon_s(t) = \frac{C_0}{l_s} \int_0^t \left[\varepsilon_t(t) + \varepsilon_r(t) - \varepsilon_i(t)\right] d\tau. \tag{4.6}$$
[cont.]

Equations (4.4) or (4.6) are usually applied, provided they are derived from non-dispersive wave propagation and homogeneous stress strain field assumptions. *However, it should be emphasized that the homogeneous stress-strain fields assumption is not necessary for the test using SHPB. If one stops at Eq. (4.1) of SHPB analysis, such a test provides an accurate measurement of forces and velocities at both sides of specimen.*

4.3.3. Other derived Hopkinson bar techniques

The split Hopkinson bar technique, which has been initially used in compression, was extended to the tension (Harding *et al.*, 1960) and torsion (Duffy *et al.*, 1971). For the tensile test, an impact tube is used to strike a T-shape incident bar (Fig. 4.5) to generate a tensile pulse. The main difficulty lies in the attaching system between specimen and bars. An important artificial initial peak is often observed in such tests.

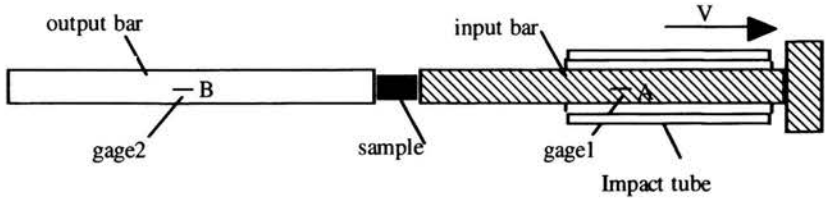

FIGURE 4.5. A typical tensile Hopkinson bar.

In compression test, the friction between bars and specimen induces an overestimation of sample strength. In order to minimise friction effects, Davies and Hunter (1963) recommend an optimal length/diameter ratio of specimen. The correction of friction effect, based on the assumption of the axial uniformity of fields, is proposed. Other suggestions for the correction of inertia and friction effects can be found in later works (Klepaczko, 1969; Dharan and Hauser, 1970; Malinowski and Klepaczko, 1986). Most of those corrections were analysed and proved by the numerical simulation work of Bertholf and Karnes (1975).

The loading system of the torsion bar is different because it is difficult to impose the rotating impact. However, the torsion wave can be generated by

accumulating torsion energy in a part of incident bar, separated by a brake. When the brake is suddenly broken, a torsion wave will propagate in the incident bar (Fig. 4.6). We observe that the torsion wave in a cylindrical bar is not dispersive.

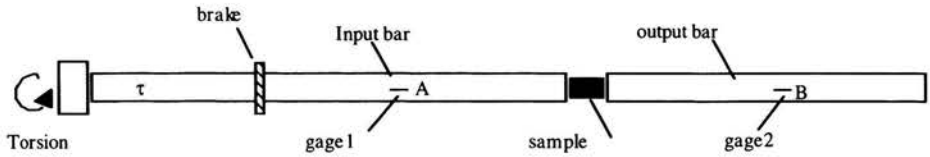

FIGURE 4.6. Torsion bar setup.

An arrangement which permits loading with only one pulse in compression, as well as in tension (Fig. 4.7), has been reported in the work of Nemat-Nasser and co-workers (1991). It is very useful for post test observations. A summery of the recent development of this SHPB technique can be found in (Zhao and Gary, 1996).

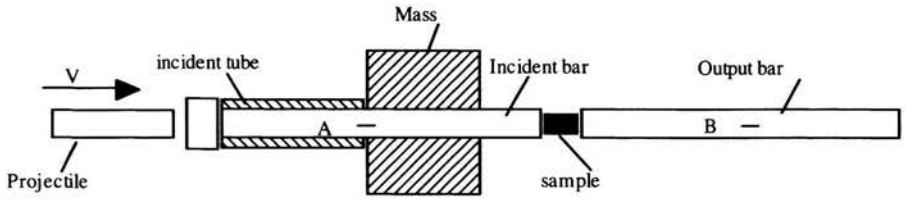

FIGURE 4.7. Arrangement to provide a tension-compression cycle

The impacting velocity for a SHPB setup is limited by the yield stress of bar, and it leads to the following relation:

$$V_{\max} \leqslant \frac{2\sigma_y}{\rho C}, \tag{4.7}$$

where σ_y is the yield stress of the bar.

Taking the nylon bar as an example, it would be dangerous to strike over 30 m/s. In order to know the behaviour at higher velocity, a modified Hopkinson bar setup should be used. A simple solution is to put specimen at the front of the input bar (Fig. 4.8) to protect the bars from a direct impact of the projectile.

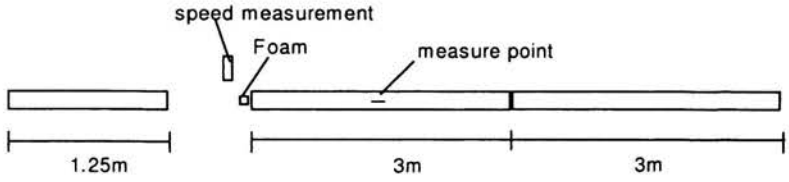

FIGURE 4.8. A modified SHPB setup, block bar.

However, we lost the measurement of the force and velocity of the input side of specimen. However, assuming that the forces at both side of foams are nearly the same, the velocity at the impacting face can be calculated. The projectile is supposed decelerated by the force measured by Hopkinson bar from its measured initial impacting velocity V_0 (by an optical device).

Taking into account the one-dimensional wave propagation in the projectile we have:

$$V_{\text{projectile}} = V_0 - \frac{1}{S_p \rho_p C_p}\left[F(t) + \sum_{n=1}^{N} 2F(t - nT)\right], \quad \text{if } NT \leqslant t \leqslant (N+1)T, \tag{4.8}$$

where S_p, ρ_p, C_p are the cross-sectional area, the density and the wave velocity of the projectile, respectively, while $N = \text{int}(t/T)$, and T is the characteristic time, i.e. time needed for the wave to travel twice the projectile length.

4.4. High velocity impact tests

For much higher velocity impact behaviour, the most common test is the plate-impact test which consists of launching a flying plate with a gas gun at the speed range from 100 m/s to several kilometers per second to impact a target plate. From measured free surface velocity history of the target plate (by the Visar system for example) and impacting velocity, wave propagation information in the target plate is known which gives indirect information about target material behaviour (Fig. 4.9).

It should be noted that the material information in the centre of the target is under one-dimensional strain state because the waves have no time to reach the lateral free surface during impact. Such a situation yields an

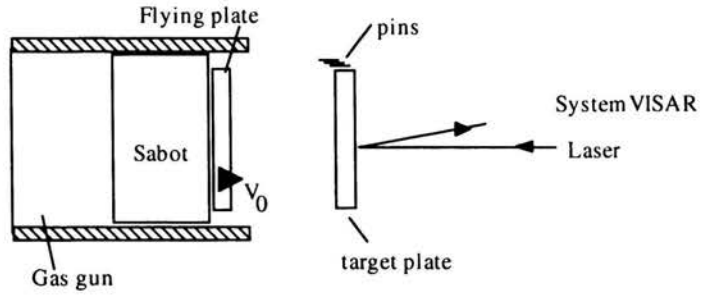

FIGURE 4.9. Plate impact tests.

important hydrostatic stress:

$$\boldsymbol{\varepsilon} = \begin{bmatrix} \varepsilon_1 & 0 & 0 \\ 0 & 0 & 0 \\ 0 & 0 & 0 \end{bmatrix}, \qquad \boldsymbol{\sigma} = \begin{bmatrix} \sigma_1 & 0 & 0 \\ 0 & \sigma_2 & 0 \\ 0 & 0 & \sigma_3 \end{bmatrix}. \tag{4.9}$$

Other high velocity tests such as Taylor's impact test or ring expansion tests are not presented here. The interested reader can easily find necessary information in (Zukas, 1982, 1991; Meyers, 1994; Zhao, 1995).

Chapter 5

Viscoelastic SHPB for soft (cellular) materials

5.1. Introduction, need for large diameter soft bars

>From the analysis presented in Chapter 3, it can be seen that SHPB tests provides more accurate experimental data of material behaviours at high strain rates. However, such tests can not be applied directly to cellular materials because of the following difficulties.

First, for large cell cellular materials, specimens must be large enough to be representative of the studied materials. Bars of large diameter are needed to ensure a sufficient sectional area.

Second, the main characteristics of foams is their relatively weak resistance compared to solid materials so that the force to be measured is small. Such a small force yields very small strains in the output bar if the usual steel bars are used. According to Eq. (4.1), the transmitted wave $\varepsilon_t(t)$ is proportional to the force at the bar-specimen interface, but inversely proportional to the product of the cross-sectional area and the Young modulus of the bar.

One method to enhance the signal is to embed a piezoelectric film in the bar. It may improve the recorded signals in the output bar (Chen *et al.*, 1999, 2000, 2003). However, it does not solve the problem for input bar where the force to be measured is the difference between incident wave and reflected wave, which are close to each other. Therefore, reducing the impedance of pressure bar is necessary for testing soft specimens.

In this Chapter, a solution consisting in using soft nylon bars with large diameters is suggested in order to improve the impedance ratio and consequently the signal/noise ratio.

5.2. Wave dispersion correction for large diameter nylon bars

Soft nylon bars are unfortunately viscoelastic and the wave dispersion increases greatly with the diameter of the bars. Kolsky's original SHPB analysis is based on the basic assumption that the wave propagation in the bars can be described by the one-dimensional wave propagation theory. As the three waves are not measured at bar-specimen interfaces in order to avoid their superposition, they have to be shifted from the position of the strain gages to the specimen faces, in terms of both time and distance. This shifting requires the knowledge of wave propagations along the bar.

Wave dispersion in a cylindrical bar was extensively studied in past decades. Following Davies' works (1948), Pochhammer and Chree's harmonic wave propagation theory has been used in the data processing. The oscillations due to wave dispersion effects observed in average stress-strain curves were decreased (Follansbee and Franz 1983; Gorham, 1983; Gong *et al.*, 1990; Lifshitz and Leber, 1994; Zhao and Gary, 1996).

The correction of wave dispersion due to viscoelastic behaviour coupled with geometrical effect is indispensable. Based on Pochhammer's and Chree's longitudinal wave solution for an infinite cylindrical elastic bar, the dispersion correction was extended to viscoelastic bars (Zhao and Gary, 1995). Even though the Pochhammer–Chree solution is not an exact solution for a finite bar, it is sufficiently accurate for long bars. Such a correction procedure is then accepted and applied by many authors.

Assuming that the exact solution for the harmonic wave propagation in an infinite linear viscoelastic rod can be represented by a combination of harmonic waves for all frequencies, the displacement $\mathbf{u}(r,z,t)$ can be then expressed as follows:

$$\mathbf{u}(r,z,t) = \frac{1}{2\pi}\int_{-\infty}^{+\infty} \bar{\mathbf{u}}(r,\omega)\, e^{i[\xi(\omega)z-\omega t]}d\omega. \tag{5.1}$$

The complete 3D analysis gives the frequency equation between frequency ω and complex wave number ξ. The real part of ξ defines the relation between

frequency and associated phase velocity, and its imaginary part gives the relation between the frequency and the associated damping coefficient. The solution of this frequency equation leads to the dispersive relation $\xi(\omega)$ which depends on the mechanical properties and on the diameter of the bar. It takes into account coupled geometry and material effects.

We observe that performing the wave shifting by simply adding the effects of the elastic geometry dispersion and the one-dimensional viscoelastic wave propagation is not correct. This is mostly due to the strong coupling between the geometry and the attenuation coefficient (Zhao and Gary, 1995).

Once the dispersive relation is known, one can calculate the wave $u_z^p(t)$ propagated at a distance Δz from the measured wave $u_z^m(t)$. According to Eq. (5.1), the components in the z-direction at the surface of the bar $u_z^m(t)$ and $u_z^p(t)$ are:

$$\begin{aligned} u_z^m(t) &= \frac{1}{2\pi} \int_{-\infty}^{+\infty} \bar{u}_z(r_0, \omega)\, e^{i[\xi(\omega) z_0 - \omega t]} d\omega, \\ u_z^p(t) &= \frac{1}{2\pi} \int_{-\infty}^{+\infty} \bar{u}_z(r_0, \omega)\, e^{i[\xi(\omega)(z_0 + \Delta z) - \omega t]} d\omega. \end{aligned} \tag{5.2}$$

The wave shifting procedure is then performed numerically by the Fast Fourier Transform:

$$u_z^p(t) = \mathrm{FFT}^{-1}\left[e^{i\xi(\omega)\Delta z}\, \mathrm{FFT}\,[u_z^m(t)]\right] \tag{5.3}$$

5.3. Identification of the material parameters of nylon bar

As mentioned in the introduction, a series of papers gave satisfactory wave dispersion correction based on the Pochhammer–Chree's model for elastic rods. For a viscoelastic bar, the same process can be used with the method presented here if the viscoelastic wave propagation characteristics $\xi(\omega)$ of the bar is known. In practice, these characteristics are not given and they cannot be measured with a quasi-static test. Thus, an impact identification of its viscoelastic characteristics must be performed.

Different methods can be used to obtain this complex function $\xi(\omega) = \alpha(\omega) + i\beta(\omega)$, the real part of which defines the wave dispersion whilst the imaginary part the attenuation. For example, waves generated by a simple

impact can be recorded at two or more different points. From two recorded signals, a direct experimental determination is possible (Blanc, 1993; Humen and Potesil, 1993; Bacon, 1998, Bacon and Brun; 2000). From Eq. (5.3) we get

$$e^{i\xi(\omega)\Delta z} = \frac{\mathrm{FFT}\,[u_z^p(t)]}{\mathrm{FFT}\,[u_z^m(t)]}. \tag{5.4}$$

It leads to a direct dependance of $\beta(\omega)$ from the modulus of the ratio between two signals and that of $\alpha(\omega)$ on the angle of this ratio.

Another possibility is to use an identification process based on an inverse calculation technique. It is assumed that the functions $\lambda^*(\omega)$, $\mu^*(\omega)$ in the wave propagation equation (2.29) have a pre-defined form with some parameters to be determined. Using the wave at a recording point as input data, the parameters can be determined by comparing the predicted wave with the recorded wave at another point.

As an example, the model describing a nylon bar is constructed from the one-dimensional rheological model: four Voigt elements and a spring, connected in series. Assuming that the material is homogeneous and isotropic with constant Poisson's ratio, the functions $\lambda^*(\omega)$, $\mu^*(\omega)$ can be constructed with nine parameters to be determined (Fig. 5.1).

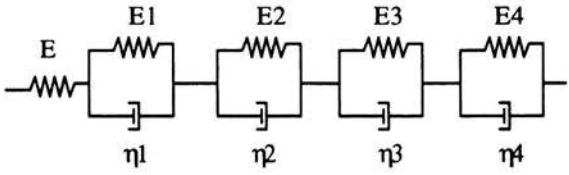

FIGURE 5.1. Rheological model.

To illustrate the excellent quality of the identification of those parameters, the original record and two other records at respective distances of 4 m and 8 m of the original one, as well as their corresponding predictions, are shown in Fig. 5.2.

Another method based on the frequency resonance of the bar is also possible. For a finite length bar, the duration of the round trip of the wave propagation depends on the wave speed and length of the bar. If the time signal is measured for a sufficiently long time, there should be a resonance frequency peak in the spectrum of corresponding signal (Othman *et al.*, 2002).

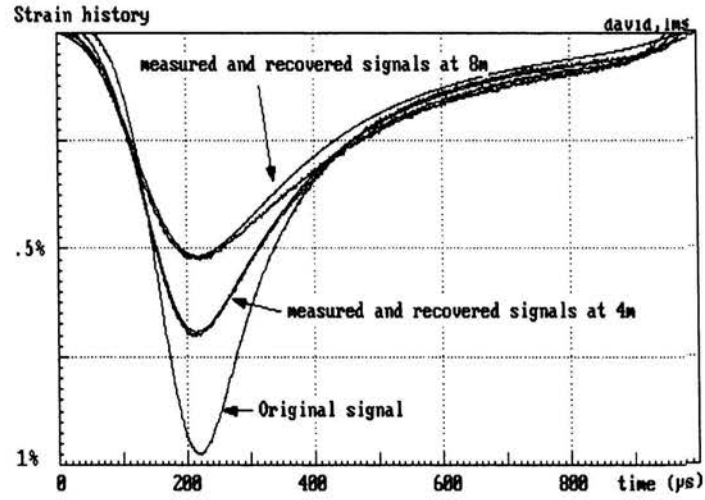

FIGURE 5.2. Test of the identified parameters (after Zhao and Gary, 1995).

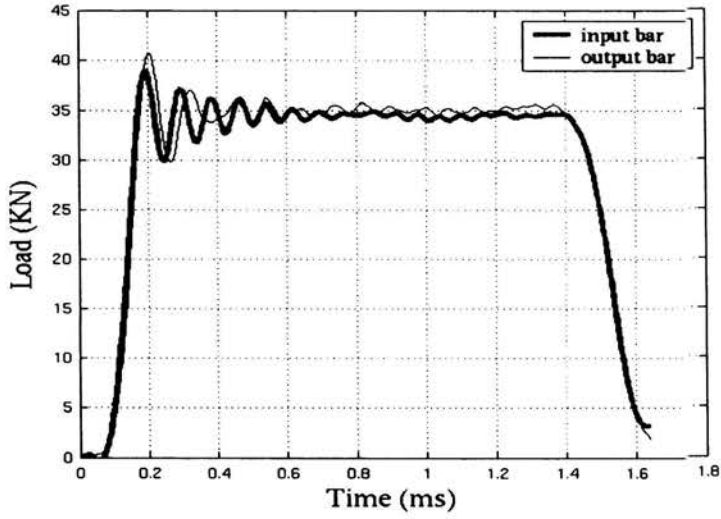

FIGURE 5.3. Comparison of input and output forces.

In order to show the quality of this correction, a SHPB test without specimen is carried out. In such a test, the input and output forces should be equal. Figure 5.3 presents a comparison between these two forces for a 60 mm diameter nylon bar. It proves the efficiency of the proposed correction.

5.4. Wave separation methods

The measuring technique using pressure bars relies on the knowledge of two elementary waves propagating in opposite directions. Once they are known, they can be shifted in time to the desired cross-section (for example, to bar specimen interfaces) to calculate the force and particle velocity at that point. However, the directly measurable quantities such as strains or velocities anywhere on the bar are the sum and the difference of the two elementary waves. The SHPB technique uses long bars and a short loading pulse so that there exists a cross-section where the total incident pulse and first part of reflected waves (of the same duration) can be recorded separately. There exists a maximum pulse duration depending on the length of the pressure bars. The measuring duration ΔT of a classical SHPB set-up is limited (Kolsky, 1963) to $\Delta T \leqslant L/C$ where C is the wave speed and L the length of the bar. Consequently, the total relative displacement Δl between the two bar-specimen interfaces is limited by $\Delta l \leqslant V\Delta T$ for a given loading speed V. For material behaviour tested at a given average strain rate, the maximum measurable strain is limited ($\varepsilon_{\max} \leqslant \dot{\varepsilon}\Delta T$). For instance, the measurable duration does not exceed 400 μs for a SHPB set-up made of 2 m long steel bars ($C \cong 5000$ m/s) and the measurable maximum strain is limited then to 20%, for a test performed at the average strain rate of about 500 s^{-1} (and only 1% for 25 s^{-1}). The SHPB technique then fails in testing of cellular material because the maximum strain attained is insufficient to investigate the locking strain.

One solution is to built a very long SHPB bar system (Albertini *et al.*, 1993). On the other hand, some earlier workers have analysed the multiple reflections in bars to increase the measuring duration of SHPB. Campbell and Duby (1956) reported a method based on one-dimensional elastic wave theory. Lundberg and Henchoz (1977) also proposed a simple explicit formula (within one-dimensional wave propagation assumption) to separate the two elementary waves and to measure the particle velocity outside observation window, using two signals recorded at two different cross-sections in the bar.

Considering the two elementary waves in the bar, the wave propagating in the positive direction (arbitrarily defined) is named the "ascending" wave and the other one the "descending" wave (to avoid the confusion with the classical SHPB, the terms "incident wave" and "reflected wave" are not used here). The strain $\varepsilon(t)$ at each section is the sum of the contribution of the

elementary "ascending" wave $\varepsilon_{\text{asc}}(t)$ and that of the elementary "descending" wave $\varepsilon_{\text{des}}(t)$, and the velocity $v(t)$ is proportional to their difference:

$$\begin{aligned} \varepsilon(t) &= \varepsilon_{\text{asc}}(t) + \varepsilon_{\text{des}}(t), \\ v(t) &= C_0\big[\varepsilon_{\text{asc}}(t) - \varepsilon_{\text{des}}(t)\big], \end{aligned} \tag{5.5}$$

where C_0 is the wave speed.

At the section where the strain is measured, a prior knowledge of the contribution of one elementary wave will allow to calculate another one.

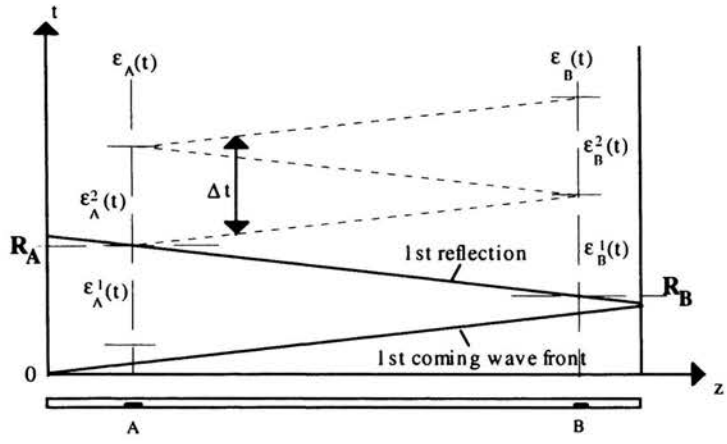

FIGURE 5.4. Wave separation scheme.

Two strain gages are then cemented at distinct points A and B of the bar, as shown in Fig. 5.4. The strain histories at those two points $\varepsilon_{\text{A}}(t)$ and $\varepsilon_{\text{B}}(t)$ are recorded. Since the bar is loaded at one end (by the projectile for the input bar and by the specimen for the output bar) while the other end remains at rest, the recorded signal at the first measuring cross-section A is due to a single elementary wave until the reflection at the other end comes back. The "ascending" wave $\varepsilon_{\text{asc A}}(t)$ at A (because of positive direction of z-axis) is then equal to the measurement at point A for the period $t < R_{\text{A}}$. Similarly, the "descending" wave at point B $\varepsilon_{\text{des B}}(t)$ is equal to zero for the period $t < R_{\text{B}}$:

$$\begin{aligned} &\varepsilon_{\text{asc A}}(t) = \varepsilon_{\text{A}}(t), \quad \text{if } t < R_{\text{A}}, \\ &\varepsilon_{\text{des B}}(t) = 0, \qquad\quad \text{if } t < R_{\text{B}}. \end{aligned} \tag{5.6}$$

In order to exhibit "ascending" and "descending" waves from measurements at A and B which become afterwards mixtures of both elementary waves, an iterative process is constructed. The strain measurements $\varepsilon_{\mathrm{B}}(t)$ and $\varepsilon_{\mathrm{B}}(t)$ are divided into small pieces $\varepsilon_A^i(t)$ and $\varepsilon_{\mathrm{B}}^i(t)$ of constant time length Δt as shown in Fig. 5.4. This interval Δt is twice the time needed by the waves to travel between the two gages. In other words, $\varepsilon_{\mathrm{A}}^1(t)$, $\varepsilon_{\mathrm{A}}^2(t), \ldots$, $\varepsilon_{\mathrm{A}}^i(t)$ and $\varepsilon_{\mathrm{B}}^1(t)$, $\varepsilon_{\mathrm{B}}^2(t), \ldots, \varepsilon_{\mathrm{B}}^i(t)$ are obtained through the characteristic function of the intervals $[(i-1)\Delta t\,, i\Delta t]$ $(i = 1, 2, 3, \ldots)$:

$$\begin{aligned} \varepsilon_{\mathrm{A}}^i(t) &= \begin{cases} \varepsilon_{\mathrm{A}}(t), & \text{if } R_{\mathrm{A}} + (i-2)\Delta t \leqslant t \leqslant R_{\mathrm{A}} + (i-1)\Delta t, \\ 0, & \text{otherwise,} \end{cases} \\ \varepsilon_{\mathrm{B}}^i(t), &= \begin{cases} \varepsilon_{\mathrm{B}}(t), & \text{if } R_{\mathrm{B}} + (i-1)\Delta t \leqslant t \leqslant R_{\mathrm{B}} + i\Delta t, \\ 0, & \text{otherwise.} \end{cases} \end{aligned} \tag{5.7}$$

This operation can be applied to both virtual elementary "ascending" and "descending" waves at points A and B to obtain $\varepsilon_{\mathrm{asc\,A}}^i(t)$, $\varepsilon_{\mathrm{asc\,B}}^i(t)$, $\varepsilon_{\mathrm{des\,A}}^i(t)$, and $\varepsilon_{\mathrm{des\,B}}^i(t)$. According to Eq. (5.6), the "ascending" wave at A for $i = 1$ $(R_{\mathrm{A}} - \Delta t \leqslant t \leqslant R_{\mathrm{A}})$, $\varepsilon_{\mathrm{asc\,A}}^1(t)$ is known. Knowing how the waves propagate, the "ascending" wave at point B can be found from the "ascending" wave at point A by applying the shifting function (transportation without shape change in one-dimensional wave propagation theory)

$$\varepsilon_{\mathrm{asc\,B}}^1(t) = f_{\mathrm{shift}}\left(\varepsilon_{\mathrm{asc\,A}}^1(t)\right). \tag{5.8}$$

Using Eqs. (5.5) at the point B for $i = 1$ $(R_{\mathrm{B}} \leqslant t \leqslant R_{\mathrm{B}} + \Delta t)$, the corresponding part of the "descending" wave at point B is

$$\varepsilon_{\mathrm{des\,B}}^1(t) = \varepsilon_{\mathrm{B}}^1(t) - \varepsilon_{\mathrm{asc\,B}}^1(t). \tag{5.9}$$

The same process is performed to calculate the "ascending" wave at point A for the next interval from the knowledge of the "descending" wave given by Eqs. (5.5). Following this procedure, an iterative formula is constructed and both "ascending" and "descending" waves can be calculated for all the time intervals.

5.5. Wave dispersion correction in wave separation iterative process

As indicated by some authors (Campbell and Duby, 1956; Lundberg and Henchoz, 1977, Bacon *et al.*, 1994, Lataillade *et al.*, 1994; Lundberg *et al.*, 1990), such a method is valid only if the wave dispersion effect can be neglected. If the wave dispersion effects are not taken into account, the accuracy of the two strain measurement method becomes rapidly insufficient with the increase of the propagation distance. Consequently, a more accurate Pochhammer–Chree type propagation theory must be used and so-called wave dispersion effects are to be taken onto account, as it has already been introduced in the SHPB to improve the accuracy of the shifting process.

It is then natural to use this wave propagation theory. Such an approach relies on the assumption that waves in the bar are harmonic so that all the associated variables can be described by their harmonic components. For instance, the strain $\varepsilon(z,t)$ can be expressed as follows:

$$\varepsilon(z,t) = \int_{-\infty}^{+\infty} \varepsilon^*(\omega)\, e^{i[\xi(\omega)z-\omega t]} d\omega, \tag{5.10}$$

where the upper asterisk denotes frequency components of corresponding temporal functions.

The dispersion relation $\xi = \xi(\omega)$ between the wave number ξ and the frequency ω, describing the propagation of each frequency component, is defined through the so-called frequency equation derived from the solution of the three-dimensional wave propagation in an infinite bar (see Chapter 2).

The signal $\varepsilon_{\mathrm{A\,asc}}(t)$ or $\varepsilon_{\mathrm{B\,asc}}(t)$ at section A or B is considered as the component $\varepsilon_{z\,\mathrm{asc}}$ of the strain tensor $\boldsymbol{\varepsilon}$ in the axis of the bar (z-axis). For any elementary wave we have:

$$\begin{aligned} \varepsilon_{\mathrm{A\,asc}}(t) &= \varepsilon_{z\,\mathrm{asc}}(z_{\mathrm{A}},t) = \int_{-\infty}^{+\infty} \varepsilon^*_{z\,\mathrm{asc}}(\omega)\, e^{i[\xi(\omega)z_{\mathrm{A}}-\omega t]} d\omega, \\ \varepsilon_{\mathrm{B\,asc}}(t) &= \varepsilon_{z\,\mathrm{asc}}(z_{\mathrm{B}},t) = \int_{-\infty}^{+\infty} \varepsilon^*_{z\,\mathrm{asc}}(\omega)\, e^{i[\xi(\omega)z_{\mathrm{B}}-\omega t]} d\omega. \end{aligned} \tag{5.11}$$

The wave shifting between A and B (separated by the distance $\Delta z = z_{\mathrm{B}} - z_{\mathrm{A}}$) is obtained by multiplying the frequency components by a term

depending on the dispersive relation:

$$\varepsilon^*_{\mathrm{B\,asc}}(\omega) = \varepsilon^*_{\mathrm{A\,asc}}(\omega)\, e^{i\xi(\omega)\Delta z}. \tag{5.12}$$

5.5.1. Approach in the time domain

For the time separating scheme presented above, the shifting function used in Eq. (5.8) is obtained with this wave propagation theory and evaluated numerically using the Fast Fourier Transform (FFT):

$$f_{\mathrm{shift}}\left(\varepsilon^i_{\mathrm{asc,des}}(t)\right) = \mathrm{FFT}^{-1}\left[e^{i\xi(\omega)\Delta z}\,\mathrm{FFT}\left[\varepsilon^i_{\mathrm{asc,des}}(t)\right]\right]. \tag{5.13}$$

We observe that the time separation scheme becomes theoretically not exact because of the incompatibility between the temporal cuts and infinite stationary wave propagation theory. For example, the interval of duration Δt has been previously defined as "twice the time required by the waves for a travel between two gages", but a common value with respect to frequency components of Δt cannot be defined because the wave velocity now depends on the frequency.

To overcome this difficulty, one can separate each frequency component and apply this time domain separation scheme for each component and to combine all the separated frequency components jointly (Jacquelin and Hamelin, 2003).

In order to test the overall efficiency of the method in a real situation, a bar with three strain gages is used. Figure 5.5(a) shows the strain recordings at the points A and B of viscoelastic nylon bar. Using this new separation method, we can recover the strain history at any point of the bar. Figure 5.5(b) illustrates the comparison at C between the measured value and that recovered with the method (C was here chosen as the middle point of the bar).

The nylon bar is only slightly viscous and the recorded signals is similar to those recorded from elastic set-up. However, the one-dimensional elastic wave approximation does not offer results of sufficient accuracy (Lundberg and Henchoz, 1977). The comparison between the recovered signal obtained by the one-dimensional elastic approximation and the measured signal is shown in Fig. 5.5(c). It shows that a more accurate description of the wave propagation is indeed necessary in this case.

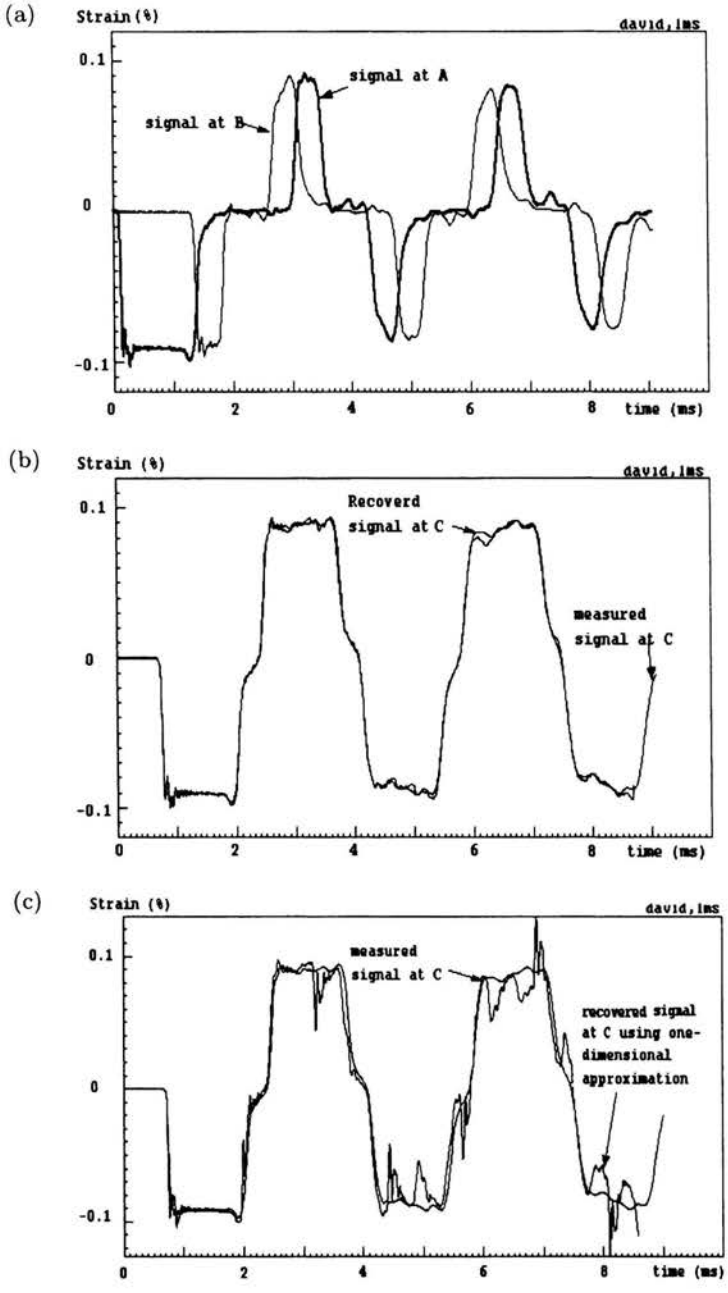

FIGURE 5.5. (a) Direct measurements at points A and B. (b) Measurement at point C compared with reconstructed value. (c) Measurements at point C compared with theoretical values obtained using the one-dimensional approximation (after Zhao and Gary, 1997).

5.5.2. Approach in the frequency domain

Since the wave shifting is defined in the frequency domain, it should be easier to conduct separating scheme in this domain. Indeed, the linearity of Eqs. (5.5) shows that the frequency components of the strain can be expressed as the sum of the components of "ascending" and "descending" waves:

$$\begin{aligned} \varepsilon^*_{\mathrm{A}}(\omega) &= \varepsilon^*_{\mathrm{asc\,A}}(\omega) + \varepsilon^*_{\mathrm{des\,A}}(\omega), \\ \varepsilon^*_{\mathrm{B}}(\omega) &= \varepsilon^*_{\mathrm{asc\,B}}(\omega) + \varepsilon^*_{\mathrm{des\,B}}(\omega). \end{aligned} \tag{5.14}$$

Using Eq. (5.12), we can substitute the "descending" wave at A by that at B and vice versa so that Eqs. (5.14) leads to:

$$\begin{aligned} \varepsilon^*_{\mathrm{asc\,A}}(\omega) &= \frac{\varepsilon^*_{\mathrm{B}}(\omega) - \varepsilon^*_{\mathrm{A}}(\omega)\, e^{-i\xi(\omega)\Delta z}}{e^{i\xi(\omega)\Delta z} - e^{-i\xi(\omega)\Delta z}}, \\ \varepsilon^*_{\mathrm{des\,B}}(\omega) &= \frac{\varepsilon^*_{\mathrm{A}}(\omega) - \varepsilon^*_{\mathrm{B}}(\omega)\, e^{-i\xi(\omega)\Delta z}}{e^{i\xi(\omega)\Delta z} - e^{-i\xi(\omega)\Delta z}}. \end{aligned} \tag{5.15}$$

It has been found that numerically it is difficult to reach sufficient accuracy with this method. A reliable evaluation of high frequency components of the strain measurement $\varepsilon^*_{\mathrm{A}}(\omega)$ and $\varepsilon^*_{\mathrm{B}}(\omega)$ requires a fast sampling rate whereas the evaluation of low frequency components requires a long observing duration.

Besides, the denominator in Eq. (5.15) could become null when an elastic bar is used (for $\xi(\omega)\Delta z = k\pi$, $\xi(\omega)$ being a real number). It becomes also nearly null for a viscoelastic bar. This problem is related to the inability of the set-up to "see" waves having a wave length equal to the distance between two gages. For all the frequencies near those singular points, it is difficult to obtain accurate results (Bacon, 1999).

An accurate solution of this problem was found with the integration along a path on the imaginary half-plane rather than on the path along the real axis (Bussac *et al.*, 2002).

Chapter 6

Rate sensitivity of cellular materials: examples

6.1. Polymeric foams

Mechanical properties of polymeric foams are often involved in the crashworthiness study in automobile industry. For example, anthropomorphic dummies have been developed to investigate the response of the human body and to analyse their interaction with the occupant compartment, where polymeric foams are frequently used. In addition to experimental car crash investigations, numerical crash simulations have been widely used to evaluate the occupant protection in the early phases of car design. The modelling of the mechanical behaviour of polymeric foams, and especially their rate sensitivity, is indispensable.

The behaviour of polymeric foams at relatively high strain rates has been studied since 1960s. Experimental results using different devices such as the falling weight or impacting mass technique (Faruque *et al.*, 1997; Lacey, 1965; Schreyer *et al.*, 1994; Traegar, 1967; Zhang *et al.* 1997), rapid hydraulic testing machine (Chang *et al.*, 1998; Rehkopf *et al.*, 1996; Wagner *et al.*, 1997), split Hopkinson bar were reported (Rinde and Hoge, 1971, 1972; Zhao, 1997; Chen and Winfree, 2002).

Phenomenological constitutive models at high strain rates (Chang *et al.*, 1998; Faruque *et al.*, 1997; Rehkopf *et al.*, 1996; Schreyer *et al.*, 1994; Wagner *et al.*, 1997; Zhang *et al.* 1997) and those based on the micromechanical analysis were also developed (Mills, 1997; Shim *et al.*, 1992).

6.1.1. Heterogeneous stress and strain field and inverse methods

As mentioned in the last Chapter, there are two technical difficulties for the use of the SHPB device for foam testing. One is due to the low impedance ratio between the foam specimens and metallic split bars. This leads to imprecise measurements of the input force, output forces and output velocity. For example, Rinde and Hoge (1971, 1972) had to use quartz crystals for the measurement of specimen stress, which are not sufficiently accurate at the early stage of loading so that it is impossible to measure the apparent Young modulus and the yielding stress. Another particular feature of foam testing is the need to achieve a large maximum strain (up to 80%) for the study of the densification, associated with a significant increase of the stress. The experimental results presented here are obtained with 40mm diameter nylon SHPB bar (density of $1200\,\mathrm{kg/m^3}$ and sound speed of $1700\,\mathrm{m/s}$).

Figure 6.1 shows the comparison between the input and output forces measured on two faces of an open cell polyurethane foam specimen. There is no equilibrium states at the early stage of the test.

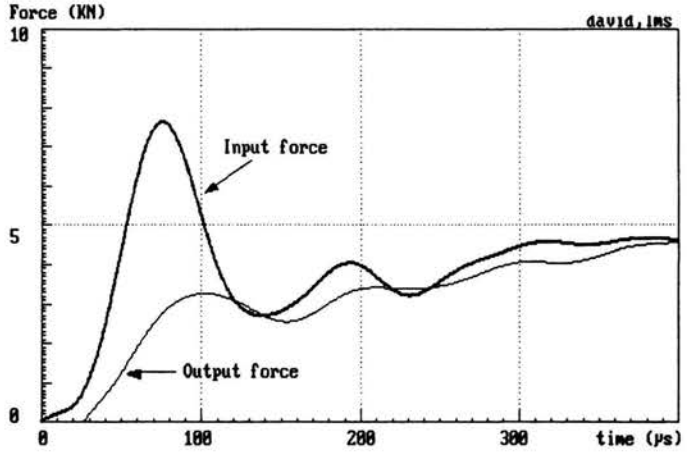

FIGURE 6.1. Non-equilibrium forces on two specimen faces (after Zhao *et al.*, 1997).

Pictures were taken during the test of foam specimens printed with a regular grid before the test. Figure 6.2(a) was taken at early stage of about 100 μs which shows a non-homogeneous strain field. Figure 6.2(b) provides a picture near the end of the test.

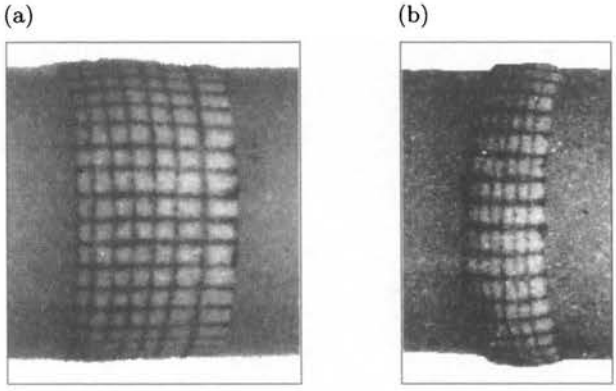

FIGURE 6.2. High speed camera photographs during testing.

It is emphasised that this non-homogenous strain field is due to the characteristic of this foam, independent of the experimental arrangement used in the test. In order to study the stress field in the specimen, additional load cell is needed in any test (even if it is a standard testing machine or a falling weight equipment). It is then necessary to develop a method which permits relating the material behaviour to the measured forces and velocities without the assumption of the stress and strain uniformity.

The measurements of the forces and particle velocities at both specimen faces can be used to provide the data on material behaviour. With an inverse approach, an appropriate form of the material behaviour can be assumed first, and then parameters can be determined using measured signals.

Let us consider a given domain Ω where forces and velocities are measured in a part of the boundary $\partial\Omega^m$.

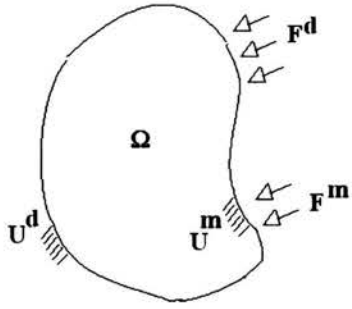

FIGURE 6.3. Inverse calculation method.

A constitutive framework is assumed with several parameters P_k to be determined:

$$\sigma_{ij} = f(\varepsilon_{ij}, \dot{\varepsilon}_{ij}, P_k). \tag{6.1}$$

The direct problem is defined by the governing equations in the domain Ω and prescribed boundary conditions:

$$\sigma_{ij,j} + f_i = \rho \frac{\partial^2 u_i}{\partial t^2}, \tag{6.2}$$

$$\varepsilon_{ij} = \frac{1}{2}\left(\frac{\partial u_i}{\partial x_j} + \frac{\partial u_j}{\partial x_i}\right), \tag{6.3}$$

$$u_i = u_i^d \text{ on } \partial\Omega^u, \qquad F_i = F_i^d \text{ on } \partial\Omega^F. \tag{6.4}$$

For the boundary where forces and velocities are measured, we use a part of the information as input data (for example the displacement field):

$$u_i = u_i^m \text{ on } \partial\Omega^m.$$

This condition gives a well-defined direct problem and it determines the forces at the boundary for a given set of parameter P_k.

The inverse problem is the identification of material parameter P_k with the minimisation of a deviation between the measured and the calculated forces:

$$\min \int_{\partial\Omega^m} \left\| F^m - F^c(u_i^m, P_k) \right\| ds. \tag{6.5}$$

Theoretical analysis shows that this inverse technique can provide good results provided that appropriate form of material behaviour of foams is found (cf. Bui, 1993). In the case of SHPB bar test, using one part of data as input data (for example velocities), the remaining data (the two forces) can be used to determine those parameters that give the best fit between the measured and calculated forces (Rota, 1997).

6.1.2. Experiments

We proceed to the presentation of general features of testing results. Most polymeric foams exhibit strong rate sensitivity because of the rate sensitivity of the base material. Their mechanical properties depend also on the temperature and moisture. Figure 6.4 shows the rate sensitivity of polyurethane

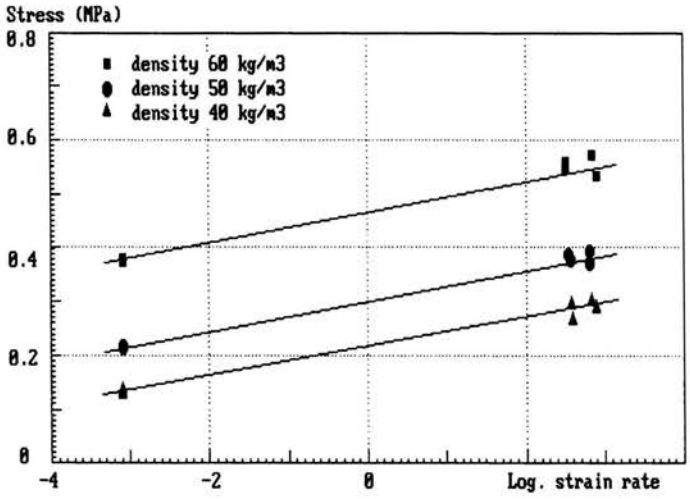

FIGURE 6.4. Rate sensitivity vs. density (after Zhao and Gary, 2002).

rigid foams as a function of its density. The specimen is a 40 mm long cylinder, 40 mm in diameter. Figure 6.4 shows that, at room temperature, static as well as dynamic stress levels increase with the density. However, the rate sensitivity is nearly the same for foams of different densities. Thus the rate sensitivity of foams mostly depends on materials of which they are made.

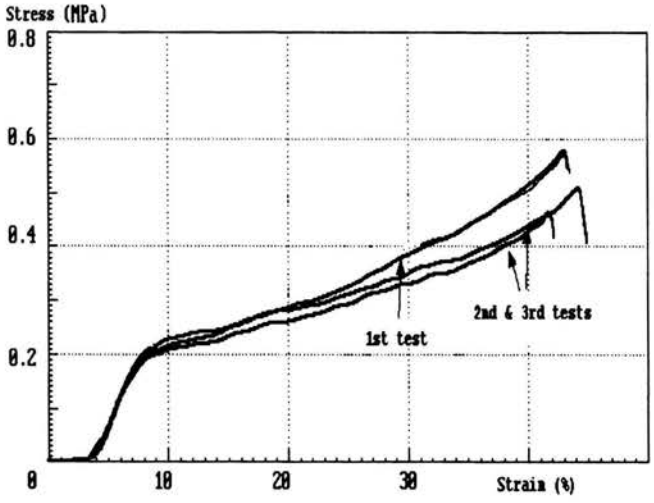

FIGURE 6.5. Cell damage effect (after Zhao and Gary, 2002).

Another interesting feature is the weak effect of the foam cell damage, especially for flexible foams. Figure 6.5 shows stress-strain curves derived from three successive SHPB tests on the same sample (diameter 40 mm, length 20 mm, density 105 kg/m^3) in the same testing condition (strain rate 325/s) during 15 min. The deformation of this kind of foams is mostly due to elastic bulking of hollow polymeric structure.

Figure 6.6 shows the rate sensitivity of foams in its complete range of strain. The test at 250/s is performed by a nylon SHPB. The generalised two-gage method provides 4 loading-unloading cycles corresponding to the reflections of the input pulse in the input bar whereas the classical analysis gives only half of a cycle. The test at 25/s is performed by a so-called "slow-bar" technique which uses the bars as measuring device and a high speed oil jack as loading device.

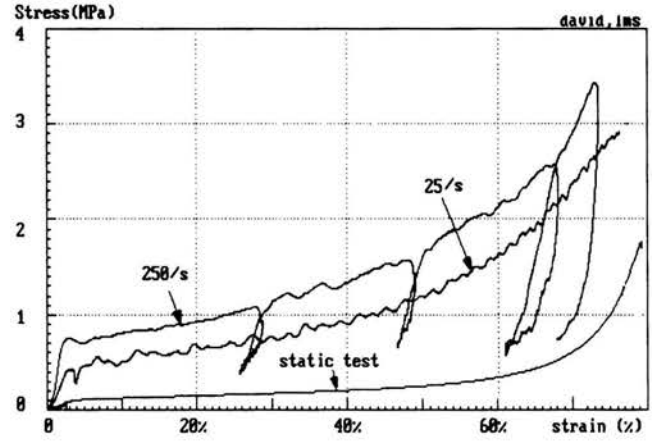

FIGURE 6.6. Rate sensitivity of closed cell polyurethane foam.

6.2. Aluminium honeycombs

Simple analysis of honeycomb presented in Chapter 1 provides a reasonable prediction of their behaviour. More accurate models with similar micromechanical analysis can be found in the relevent literature. Wierzbicki (1983) developed an out-of-plane large deformation crushing model that gives an analytical prediction of the crush pressure; Klintworth and Stronge (1988, 1989) have formulated a large-deformation behaviour of the in-plane crushing that takes account of localised deformation band effects. Related topics

such as fracture detection using elastic waves (Thwaites and Clark, 1995), negative Poisson's ratio honeycombs (Prall and Lakes, 1997), and foam-filled honeycombs (Wu *et al.*, 1997) have been also reported in the open literature.

Applications of such analyses under impact loading imply that the rate sensitivity is derived from that of the base materials as it is the case for most polymeric foams.

However, Goldsmith and co-workers (1992, 1995) reported some experimental work on out-of-plane crushing and on ballistic perforation of honeycombs. They fired a rigid projectile to a target made of honeycombs and showed that mean crushing pressure sometimes increases up to 50% with respect to the static results. These authors claim that the accuracy of the technique is not always satisfactory. Wu and Jiang (1997) also studied out-of-plane crushing with a similar experimental technique. Their results confirm significant enhancement of the crushing strength in the x_3-direction. Hönig and Stronge (2002) reported numerical results in the x_1- and x_2-directions.

6.2.1. Honeycomb specimen and nylon bar testing device

Experimental results on the behaviour of honeycomb materials under impact loading presented here are obtained with the Split Hopkinson Pressure Bar (SHPB, or Kolsky's bar) technique. The studied honeycomb resistance

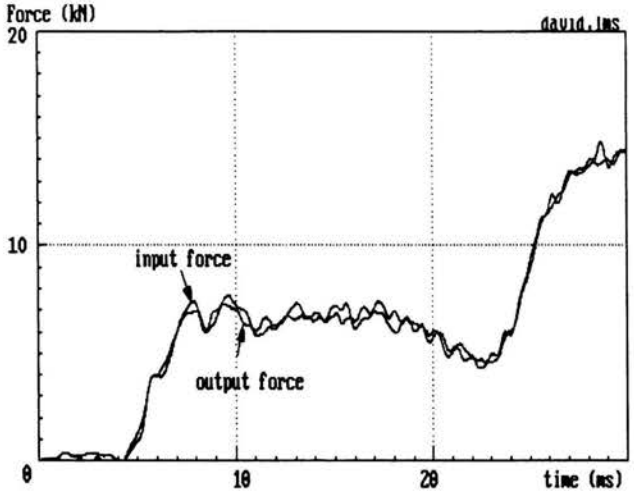

FIGURE 6.7. Equilibrium check for honeycomb tests.

is quite low (typically, 5 MPa in the x_3-direction, 0.2 MPa in the x_1- and the x_2-directions).

Two nylon (Pa 6.6) bars (3 m length, 40 mm diameter) were used to test these specimens. The two-point strain measurement method was applied for tests at 2 m/s. Simple formula (Eqs. (4.2) and (4.3)) are used to obtain the pressure-crush curves for all the tests where the equilibrium check is satisfactory. Figure 6.7 shows the input and output forces in a typical test at 10 m/s. Non-equilibrium state was not observed between forces at two sides of honeycomb, even though the homogeneous state of deformation was not achieved.

6.2.2. Rate sensitivity of the studied honeycomb

Cubic specimens (about 36 × 36 × 36 mm) are used. Two types of aluminium honeycombs (Table 6.1) are tested in three directions. Because similar results have been obtained for both honeycombs, only the results for honeycomb No. 1 are presented. For a given loading rate, the experiment is repeated at least once. To make figures more legible, only one curve is presented for one loading rate.

TABLE 6.1. Specimen characteristics.

No.	Cell size h [mm]	Thickness t [mm]	Density [kg/m^3]
1.	4.7	0.08	130
2.	6.2	0.08	100

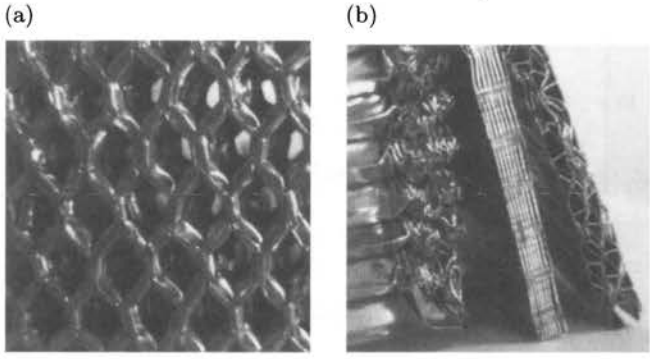

FIGURE 6.8. Post-test observations.

The post-mortem observations of crushed specimens do not reveal visible differences between static and dynamic loading. The out-of-plane crushing mode (x_3-direction) is a regular multiple localised folding (Fig. 6.8(a) and 6.8(b)-left). For in-plane crushing, a regular folding is observed in the x_1-direction (Fig. 6.8(b)-center), whereas irregular patterns are found in the x_2-direction (Fig. 6.8(b)-right), similar to those observed by Klintworth and Stronge (1988, 1989).

(a) Out-of-plane behaviour

A summary of experimental data in the x_3-direction is shown in Fig. 6.9. The difference in the maximum strain is due to the limitation of the measurement duration of the standard SHPB system (tests at 10 m/s and 28 m/s): the final crush depends on impact velocities.

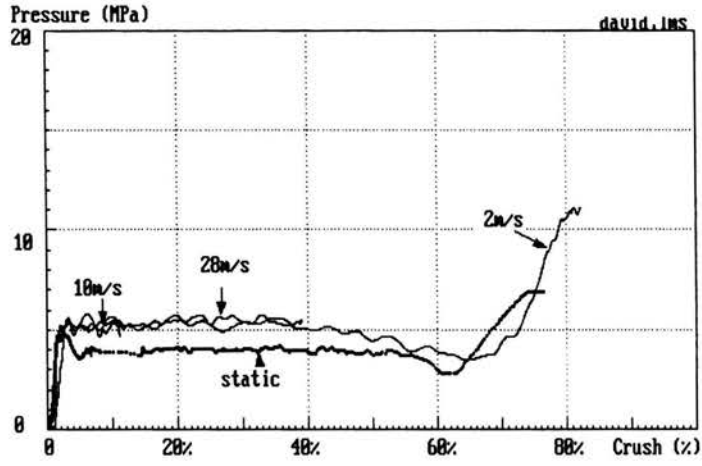

FIGURE 6.9. Mean crushing strength in direction x_3.

The significant differences between static and dynamic loading (40%) have been found for the mean crushing pressure in the x_3-direction. However, mean crushing pressures are nearly the same (about 5.4 MPa) for impact velocities from 2 m/s to 28 m/s. This result differs from those of Wu and Jiang (1997) but agrees with those of Goldsmith and Sackman (1992). The densification point seems independent of the loading rate (at 65% crush).

Table 6.2 shows the rate sensitivity for different honeycombs.

TABLE 6.2. Rate sensitivities.

t/h [mm/mm]	Density [kg/m^3]	Static [MPa]	Dynamic [MPa]	Difference [%]
0.08/4.7	130	3.9	5.4	+38
0.08/6.2	100	2.8	3.6	+28

(b) In-plane behaviour

The mean pressure in the x_1-direction is nearly the same (0.09 MPa) for dynamic (impact at 2 m/s, 10 m/s, 28 m/s) and quasi-static loads (Fig. 6.10). The densification points at different loading rates exhibit a spread but are located at about 70% of crush.

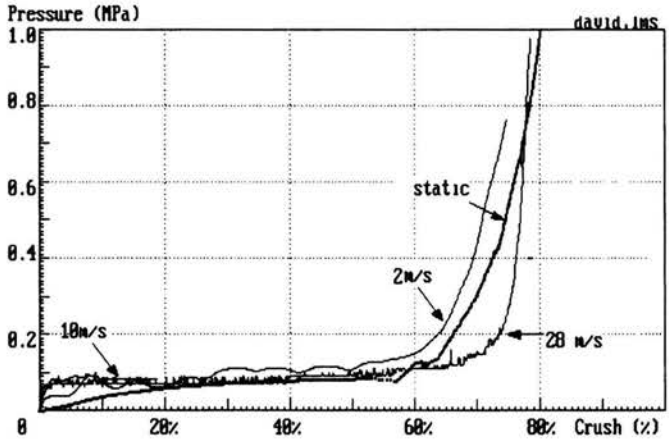

FIGURE 6.10. Behaviour in x_1-direction.

The pressure-crush curve in the x_2-direction is less regular under dynamic loading (Fig. 6.11), although the mean pressure is close to that under static loading. This is probably a consequence of the irregular deformation mode (Fig. 6.8(b)). The densification point (about 80% crush) is, again, independent of the loading rate.

Significant differences between static and dynamic results are only found in the out-of-plane crushing. The rate sensitivity of aluminium foils from which the tested honeycombs were made was then investigated. Static and dynamic tests (with steel SHPB) were performed with a crushed honeycomb (in the x_1-direction and before the full contact of foils). A 10% difference of flow stress between static loading (10^{-4}/s) and dynamic loading (600/s)

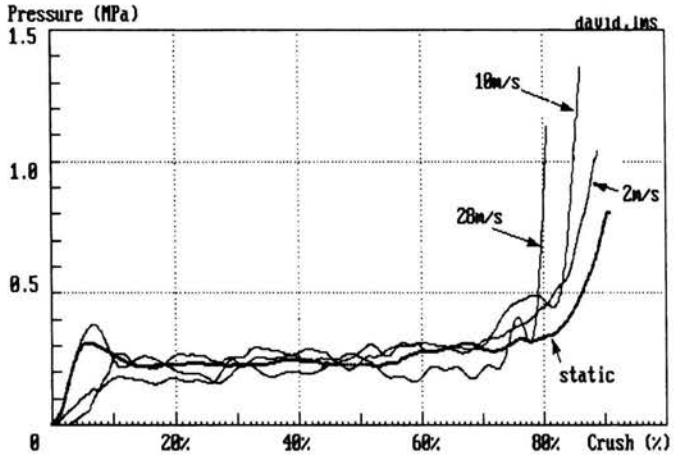

FIGURE 6.11. Behaviour in x_2-direction.

is found, which agrees with the known results in previous works (Lindholm, 1964). This result indicates that the increase of the flow stress of aluminium foils is not the major cause of the observed enhancement of the crushing strength.

Other observations also support such a conclusion. There is no significant enhancement of the crushing strength in the two in-plane (lateral) directions. This indicates that the large enhancement in the x_3-direction is related to structural effects. In addition, for the two different tested honeycombs (Table 6.2), the increase of the crushing strength in the x_3-direction appears to be proportional to the mass density, implying a correlation with structural inertia.

6.3. Aluminium foams

Metallic foams have been studied by many authors. The open cell Nickel foam or closed cell aluminium foams have been studied in the case of various loading path (Badishe *et al.*, 2000; Chastel *et al.*, 1999; Blazy, 2003). The microstructure of foam can be characterised by computer tomography images (Maire *et al.*, 2003). Such microstructural data can be used to evaluate the stiffness and strength of foams (Fazekas *et al.*, 2002). Studies on foam filled structures are also reported in the literature (cf. Hanssen *et al.*, 2000).

Regarding the rate sensitivity of aluminium foam, the same conclusion as for the aluminium honeycomb can be drawn from the simple model developed in Chapter 1. Deshpande and Fleck (2000b) used a standard SHPB arrangement (diameter 12.7 mm) with a polymeric output bar to test Alulight and Duocel open cell foams. The results obtained exhibit considerable scatter partially because of small size of specimen and no rate sensitivity was found. Mukai *et al.* (1999) investigated, using standard SHPB arrangement, Alporas foams obtained by direct foaming of aluminium melts with a blowing agent. The rate sensitivity was observed. Tan *et al.* (2002) reported impact tests using a gas-gun to launch Hydro-Cymat foam, manufactured by direct foaming of melt with gas injection technique, against the target. They used a Hopkinson bar to measure the crushing pressure and proposed a shock-wave theory to explain the observed enhancement in their tests.

>From the experimental point of view, impact test of metallic foam involves two major difficulties. The first difficulty is related to the weak strength of foam material, but it can be eventually overcome by the use of soft polymeric bar. The second difficulty is the large scatter due to small ratio (specimen size/cell size). Therefore a large diameter pressure bar to host a larger specimen is required. A 60 mm diameter nylon SHPB arrangement is in LMT-Cachan used to improve the measuring accuracy.

6.3.1. Rate sensitivity of Cymat foam

45 mm × 45 mm × 55 mm Cymat foam samples manufactured by the gas injection process are cut from foam plates of about 200 mm thickness. The

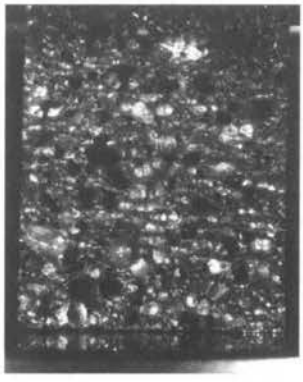

FIGURE 6.12. Microstructure of Cymat foam sample.

average density is about 250 kg/m^3. Figure 6.12 shows the microstructure of this quite brittle foam.

Tests under static and dynamic loading have been performed. The scatter is significant, because the crushing mode is the micro-fracture of cell walls which are brittle due to the addition of silicon carbide in the process (see Chapter 1). No convincing rate sensitivity is found because of the huge scatter.

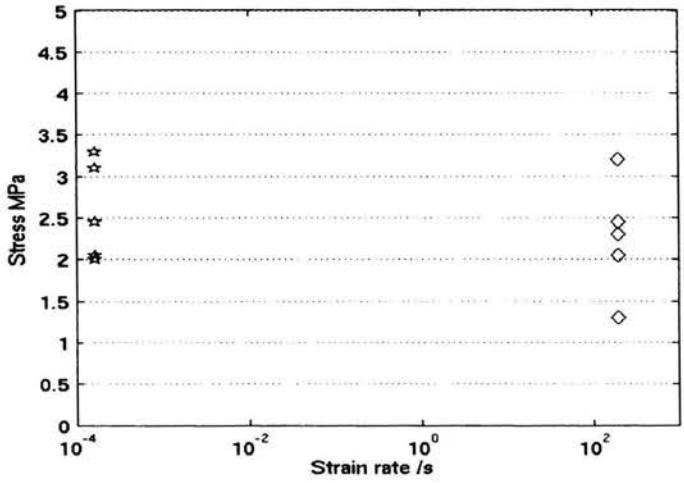

FIGURE 6.13. Cymat foam rate sensitivity.

6.3.2. Rate sensitivity of IFAM AA6061 powder metallurgy foam

IFAM foam samples are obtained from Aluminium powder blowing process. Precursor materials are composed of pre-alloyed AA6061 powder and 0.5 wt.% titanium hydride powder as a blowing agent. The powder mixture was first consolidated by cold isostatic pressing and followed by hot extrusion to long rectangular rods. The foaming was carried out in a batch furnace with indirect conductive heating and atmosphere circulation at 730°C (Lehmhus and Banhart, 2003). The final specimens are cylinders of 45 mm diameter and 60 mm height with closed outer skins. As one of the advantages of IFAM foaming process is the direct foaming process to make final product without any machining (sandwich plate, etc.), the out skin will exist anyway in the final product. Therefore it is interesting to test the IFAM foam with its skin.

The density of the specimen is about $620\,\mathrm{kg/m^3}$. X-ray Computer Tomography images reveal that the foam is not really homogeneous, and irregular holes can be found inside the specimen. A group of less heterogeneous specimens (according to the CT images) is selected to carry out this study. However, the scatter is significant because of holes.

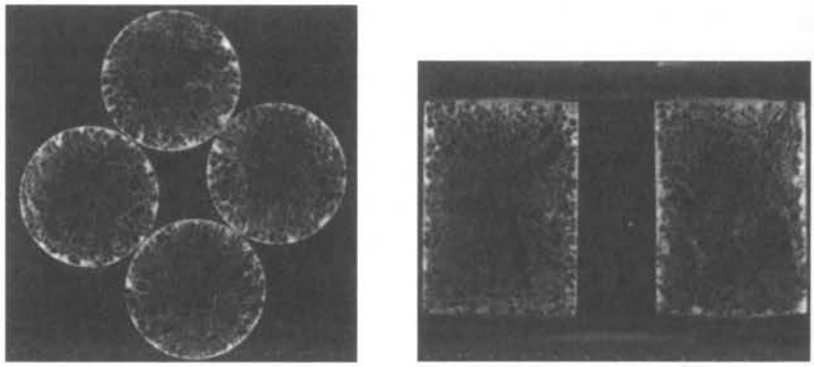

FIGURE 6.14. CT image of closed out skin IFAM foams.

Static test is performed by using a universal testing machine. The strain range is voluntarily limited to about 20% because our interest is mainly focused on the plateau yield stress for the energy absorption application. Fur-

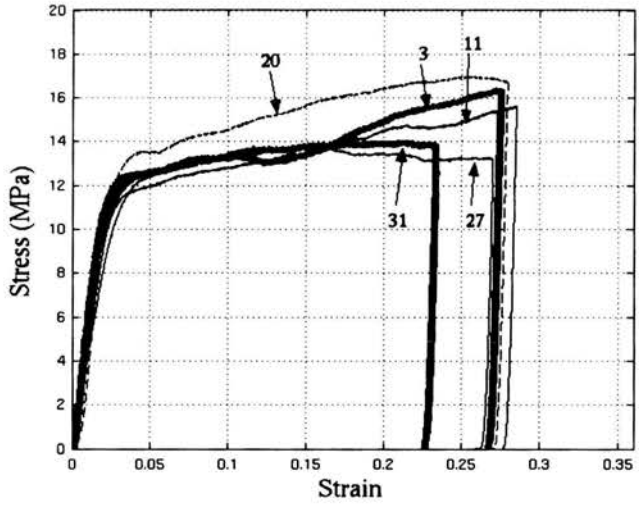

FIGURE 6.15. Static stress-strain curves.

ther dynamic loading will be carried out, as presented afterwards. Figure 6.15 shows the stress-strain curves of 5 specimens.

One can see that some foams (as specimen No. 31) have nearly no strain hardening and the others (like specimen No. 3) have weak strain hardening effect.

Figure 6.16 shows the stress-strain curves obtained with two-wave formulas in a standard SHPB configuration (specimen between input and output bars).

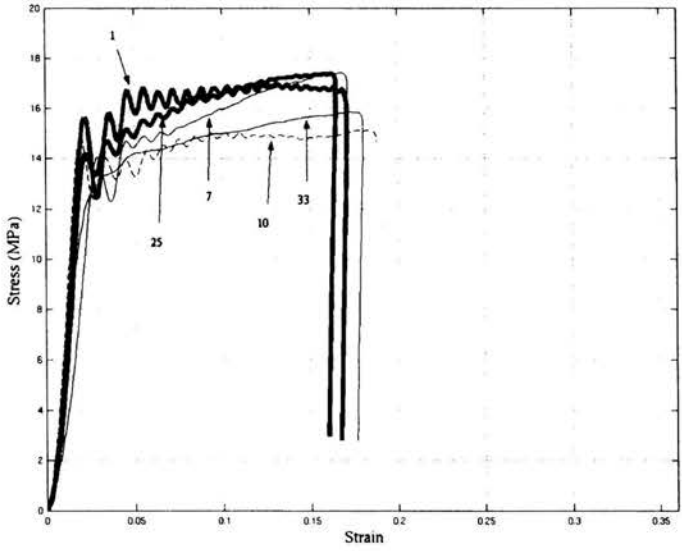

FIGURE 6.16. Dynamic stress-strain curves.

Direct impact Hopkinson bar test is also performed to get higher impact velocities up to 27 m/s. Table 6.3 summarises all static and dynamic tests.

Figure 6.17 shows the flow stress at 10% of nominal strain with respect to the logarithmic value of the nominal strain rate. It shows an enhancement of about 15% for the mean flow stress. However, the scatter is quite important and the lowest value under impact loading almost coincides with the highest value under static loading.

In order to eliminate uncertainty of the rate sensitivity because of the scatter due to the specimen morphological and mass dispersion, one possibility is to do static and dynamic test on the same specimen. Such a test is possible at least for specimens where no strain hardening are observed. Two

TABLE 6.3.

Velocity [ms]	Stress at 10% [MPa]	Density [kg/m^3]	Sample No.	Strain rate [1/s]
0.01	13.25	603.2	3	0.00016
0.01	12.8	621.4	11	0.00016
0.01	14.5	625.75	20	0.00016
0.01	13.25	616.5	27	0.00016
0.01	13.3	618.37	31	0.00016
14.6	16	609.7	7	204
14.8	14.9	638.8	10	175
15.0	15	622.8	33	139
15.0	16.5	627.5	25	180
15.6	16.6	633	1	186
25	16.2	629.8	12	365
27	14.9	631.6	13	344

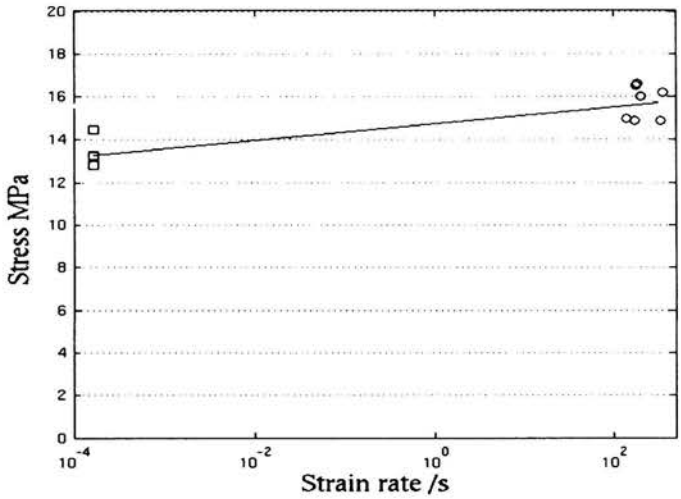

FIGURE 6.17. Rate sensitivity of foams.

ways allowing to combine static and dynamic loading are carried out. One is to perform static test to a given strain and to continue with impact loading; another is the inverse dynamic-static tests.

Figure 6.18 shows a sudden enhancement under dynamic loading for specimens already tested statically. The same tendency is observed for the speci-

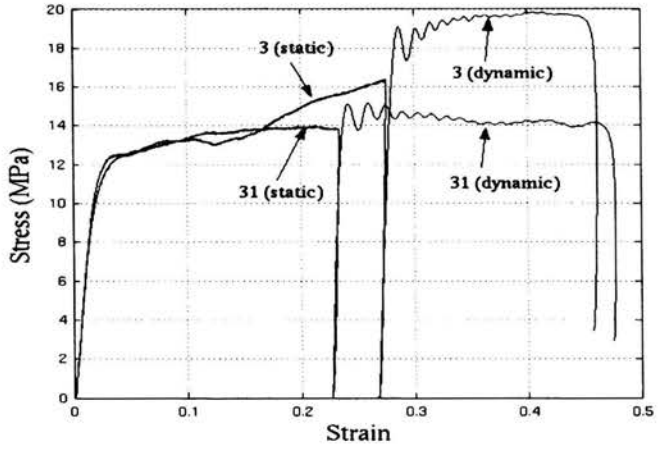

FIGURE 6.18. Static-dynamic rate jump test.

men with strain hardening (specimen No. 3) and the specimen without strain hardening (specimen No. 31). Figure 6.19 illustrates the inverse strain rate jump test where a sudden drop of the flow stress is observed. Both types of tests imply that rate sensitivity exists in this type of foam.

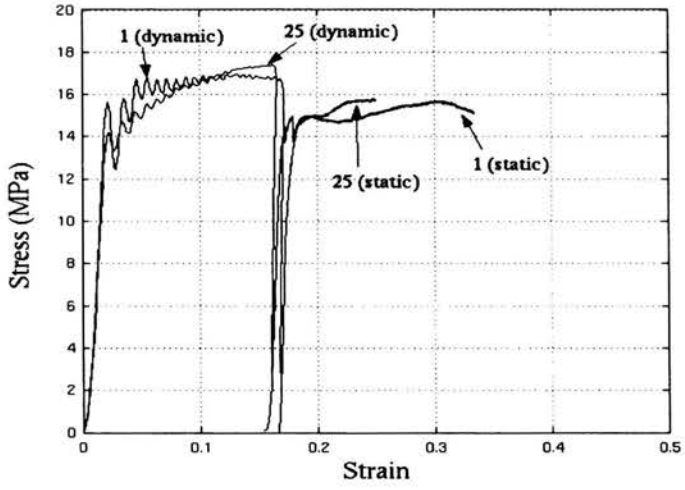

FIGURE 6.19. Dynamic-static inverse rate jump test.

6.3.3. Discussion

For IFAM foams, Fig. 6.20 shows the photograph (a) of the tested specimen No. 10 cut into two semi-cylinders, compared with CT image before testing (b). Since it is difficult to guess the right plane to cut in order to coincide with the CT image, quantitative match cannot be made. However, qualitatively it seems that the central great hole is not the weak point where the localisation would start. The localisation band is nearly perpendicular to the impact direction. It is also noteworthy that a great number of buckling system of the longitudinal cell wall (parallel to the crushing direction) is observed. All this indicates that the crushing is the result of successive buckling of cell wall.

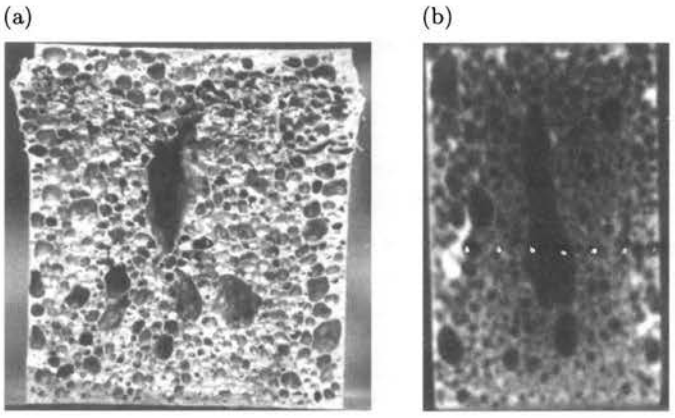

FIGURE 6.20. Comparison between initial and crushed specimens.

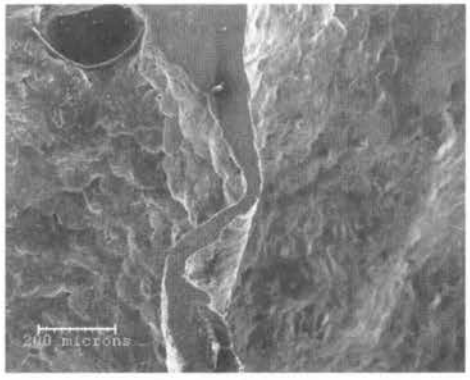

FIGURE 6.21. Micro-buckling of the cell wall.

Figure 6.21 shows a photograph under electronic microscope illustrating this micro-buckling of the cell wall.

It seems that such a crushing mode is more like the crushing mode in honeycomb than the usual assumption of the bending of the transversal cell wall. As it is shown in (Banhart and Baumeister, 2001) that the outer skin has an important influence on the behaviour because of their rigidity; such an observation might be the consequence of the existence of outer skin.

Chapter 7

Inertia effect in progressive folding: model structure study

7.1. Model structure definition

>From experimental results presented in Chapter 6, a significant rate sensitivity has been inferred for cellular materials such as ductile IFAM Al6061 foams or Al5056 honeycomb, which cannot be explained by the weak rate sensitivity of the cell wall material. The crushing mode of such cellular materials indicates that the main failure mode is progressive buckling of the cell wall so that micro-inertia may play an important role.

One of the possible methods to understand this rate sensitivity is to study a model structure under quasi-static and dynamic crushing, provided

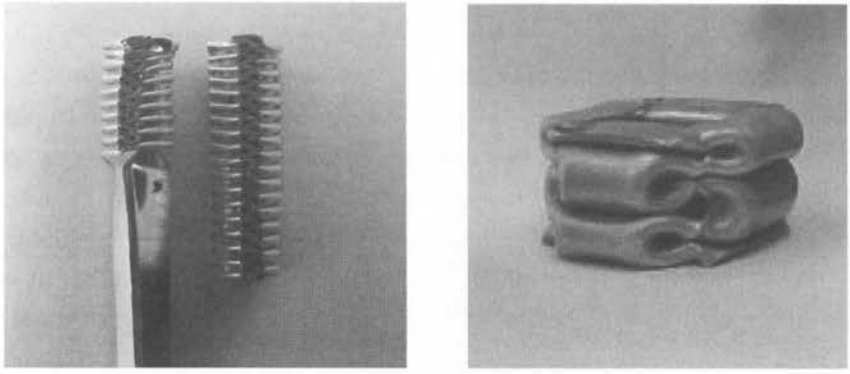

FIGURE 7.1. Crushing by ductile progressive folding.

that this structure have the same crushing mode. One of such type of model structures is commercially available brass square tube (after suitable partial annealing). Crushing of such tubes is also a progressive folding process (right part of Fig. 7.1), which is similar to the previous cases. Another advantage of such a structure is that the brass is not rate sensitive in a large range of strain rates.

The 35 mm × 35 mm square tube of 1.5 mm thickness is chosen because of the restrictions of the impact testing device. However, strain hardening during manufacturing processes makes these tubes brittle and the progressive crushing mode is not observed because of early fractures at the four ridges. Annealing becomes necessary in order to make them more ductile. To obtain a repeatable heat treatment, we measured the exact chemical composition of the studied brass tube (Cu 64%, Zn 36%) by an EDS microprobe. The corresponding phase equilibrium diagram indicates the temperature range where the phase diagram is less complex. The following heat treatment is performed: 30 min annealing at 450°C and water quenching.

7.2. Experimental study of the crushing strength for brass square tubes

7.2.1. Experimental characterization of the rate sensitivity of cell wall material

To know if the basic material is rate insensitive, especially after annealing, an experimental study of the material behaviour under a comparable loading mode (static as well as dynamic) is necessary. Compressive tests under static and dynamic loading are chosen for the following reasons:

- the main loading mode in the tube crushing is compression,
- under dynamic loading, compression test with SHPB (Split Hopkinson Pressure Bar) is much more accurate than tension test because of the specimen shapes and relevant difficulties.

However, very small specimens should be used to avoid buckling. The specimen is cut from the heat treated brass tube, the dimension of which is about 2 mm high and 10 mm wide. Quasi-static tests are performed with a MTS810 universal testing machine. The main difficulty is the strain measurement. As the specimen length is as short as 2 mm, it is hard to glue a strain gauge or put an extensometer on the specimen. The displacement

measurement of the machine is supposed to be not accurate enough to obtain a reliable strain measurement; even if the stiffness correction of the test machine can be made. An alternative is to use an optical displacement field measurement. The principle is to compare images of the specimen taken during the test by means of Kodak Megaplus CCD camera and a long-distance microscope Questar QM100. A correlative image processing technique provides the match of the same material points in different images, and it gives then the displacement of this point. The software Correli developed at LMT is used to perform this image processing task which can give a sub-pixel precision of the displacement and offer a precision of strain at least 10^{-4} with an 8-bits 1008×1016 pixel optical camera (Hild *et al.*, 1999; Chevalier *et al.*, 2001). Such a technique allows also for a check of strain fields during the test and it provides a proof that it is really a pure compression test; even if the specimen size is thin and very small.

Two typical images of the central part of brass specimen are shown in Fig. 7.2(a, b). The calculated displacement field is given in Fig. 7.2(c).

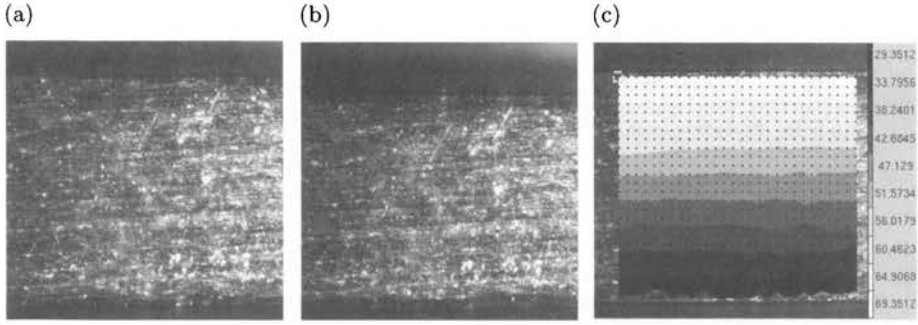

FIGURE 7.2. Image based displacement and strain measurement.

Dynamic tests are carried out with Split Hopkinson Pressure Bar or Kolsky's apparatus which has become a very popular experimental technique for the study of constitutive laws of materials undergoing high strain rates (Hopkinson, 1914; Kolsky, 1949). The only problem in applying this technique consists in shifting properly basic waves measured at the midpoint of the bar to the bar-specimen interfaces where the knowledge of forces and velocities is required. Careful data processing is necessary to obtain this shift because the waves change their shapes during the propagation (Davies, 1948; Zhao and Gary, 1995, 1996). The classical analysis, which assumes the axial

uniformity of stress and strain fields in the specimen, can be used. An average stress-strain curve can be obtained which lead to the so-called two-wave analysis or three-wave analysis (Lindholm, 1964).

Figure 7.3 shows a comparison of the stress-strain response of annealed brass at quasi static rate and various strain rates up to 2500/s. It is clear that there is no significant rate sensitivity.

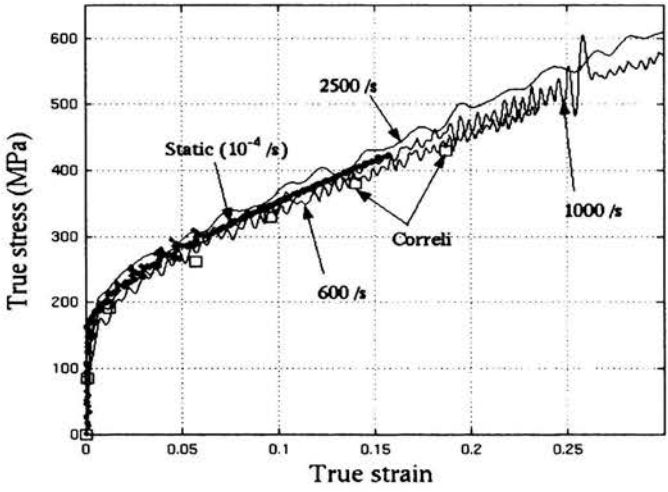

FIGURE 7.3. Stress-strain relations at static and dynamic strain rates.

7.2.2. Strength enhancement of the model structure

Static crushing tests have been performed on heat-treated tubes with a MTS810 universal testing machine. To avoid global elastic buckling mode, the length of the tube specimen is selected as 104 mm. The progressive folding mode is observed. The force-displacement recordings are quite repeatable for tested specimens and this indicates that the applied heat-treatment is reproducible and homogeneous because the buckling mode is very sensitive on local weak points.

Under dynamic loading, the measurement accuracy of the experimental arrangement available in the literature is not very satisfactory. Indeed, most of reported testing results are obtained using a falling weight device. In such tests, the deceleration of the falling mass is measured by an accelerometer and the associated force and displacement are then deduced. The accuracy is often quite low because of vibrations of the weight and its suspension

system. Thus, previous works in the available literature often report only the final crushing displacement at a given mass and initial velocity (Abramowicz and Jones, 1984, 1986). Here we used a large scale SHPB system (diameter 80 mm, input bar of 6m and output bar 4m) in order to obtain an accurate force and displacement measurements.

However, the crucial difficulty for these tests is the measurement duration required to observe the progressive peak load (after the initial peak load). A two-gauge method is used to obtain the signals after the first round trip of the waves in bars (Lundberg and Henchoz, 1977). Additional details of this measurement method are described in (Zhao and Gary, 1997) and (Bussac *et al.*, 2002). We have used the direct impact configuration to supply enough energy to crush the tube (cf. Hauser, 1966).

A typical comparison between static and dynamic tests is shown in Fig. 7.4. We can see that not only the initial peak load but also the progressive peak load are accurately measured. It shows that there is a significant enhancement of initial and progressive peak loads.

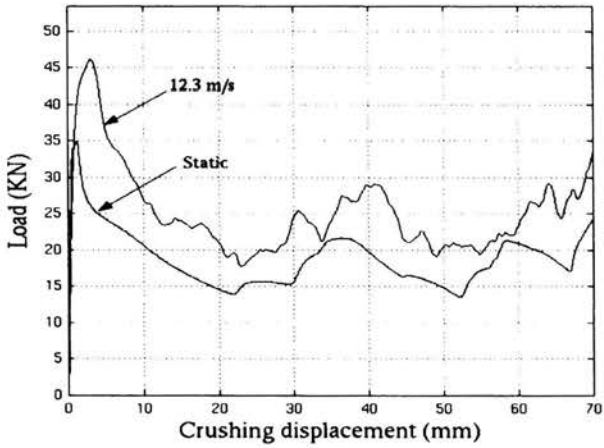

FIGURE 7.4. Force displacement curves under static and dynamic loading.

Table 7.1 provides the corresponding initial and progressive peak loads under static and impact loads. The average enhancement is about 35% for both initial and progressive peak loads. The last column gives the ratio of the progressive peak load increase to the initial peak load increase. If the base material had a rate sensitivity of 35% (which is not the case), it would explain this enhancement.

TABLE 7.1. Enhancement ratio for initial and progressive peak loads.

Speed [m/s]	Initial peak [kN]	Increase [kN]	Progressive peak [kN]	Increase [kN]	Increase ratio [%]
Static	**35**	—	**22**	—	0
7.7	43	9 (26%)	29	7 (32%)	77
9.6	43	9 (26%)	28	6 (28%)	66
11	45	11 (31%)	28	6 (28%)	54
11.5	45	11 (31%)	28	6 (28%)	54
12.3	46	12 (34%)	29	7 (32%)	58
12.6	47	13 (37%)	29	7 (32%)	53
13.5	47	13 (37%)	30	8 (36%)	61
15.3	49	15 (43%)	31	9 (41%)	60

7.3. Numerical analysis of tube crushing

In the crushing tests presented above, only force-displacement recordings are available. For static loading, some pictures of tubes during tests are also taken. There are no simple methods to know what was happening in the tube, especially under impact loading. It makes the understanding of this strength enhancement difficult. An alternative is to simulate the crushing of tubes numerically, provided that the simulation is able to reproduce accurately the force-displacement history and other observed events (pictures). Under such conditions the numerical simulation may give reliable local information, such as the stress state and deformation history in the tube.

7.3.1. Validity of numerical models

The explicit version of the commercial code Ls-dyna is used to carry out the simulations under impact loading, and the implicit version is adopted for the static loading. The same geometric file and the same Belycheko and Tsai plate elements are used in both static and dynamic loading. It is expected that the numerical errors between the static and dynamic loading will be as small as possible. The sensitivity of the simulated results on the mesh density is analysed in order to choose a suitable element size for the simulation. The chosen element size is 2.5×2.5 mm, which means that there are 14 elements in one side. It satisfies the rule of 7 elements in the half wave length, and the use of smaller elements does not make significant difference.

For the constitutive equation, the simple Johnson–Cook law parameters are identified from experimental stress-strain relations, obtained from compressive tests on very small specimen. The parameters for the rate sensitivity and temperature effect are chosen to be zero.

The simulated results of the tube crushing strongly depend on the initial imperfection introduced in the geometry of the tube. Random and sinusoidal (sinus function of the length) perturbations of wall geometry have been used. The sinusoidal perturbations are more numerically stable to initiate the symmetric progressive mode, which is observed in all our tests. Random perturbations can generate numerically an extensional crushing mode. The amplitude of this perturbation is also an important parameter. In the present case, the maximum lateral perturbation is chosen as 0.08 mm, and around this value the peak loads are nearly not affected. Figure 7.5 gives a comparison between experimental and simulated force-displacement curves under static loading. It illustrates that the numerical calculation gives a fair estimation of the force as well as the displacement.

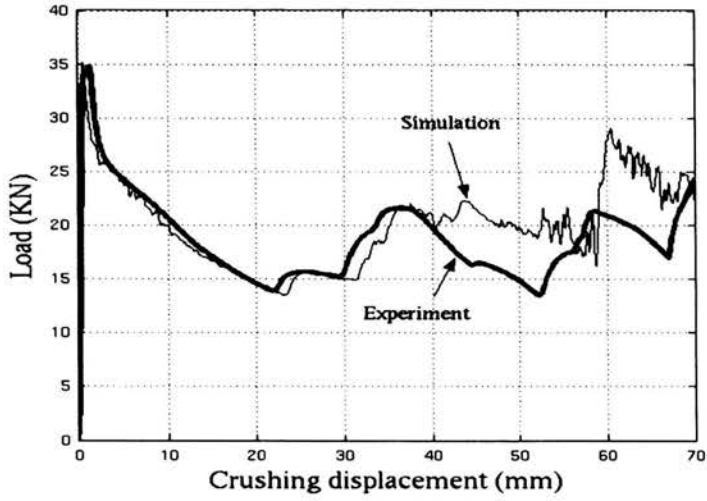

FIGURE 7.5. Experimental and numerical force-displacement curves.

It is also observed that the simulated crushing tests can give a good prediction of the progressive crushing events and reproduce the strength enhancement under impacts, which is another proof of the pertinence of simulations. All these comparisons show that the present simulations (with the specified element size, mode and amplitude of the initial geometrical per-

turbation) provide a reliable description of the tube crushing. It becomes a virtual test, providing the user an access to global and local stresses as well as to deformations at any time and to better understanding of the crushing mechanisms.

7.3.2. Folding events

A careful examination of the progressive crushing events reveals that there exist small areas around the four corner lines remaining nearly straight, while the middle of plates is significantly deformed. On the left of the simulated figures of deformed tube (Fig. 7.6), the corner line around the ridge node A is straight whereas the flat plate around nodes B or B' in the centre is already bent. On the right of Fig. 7.6, further crushing of the tube is seen and is attributed to the buckling of the corner line areas.

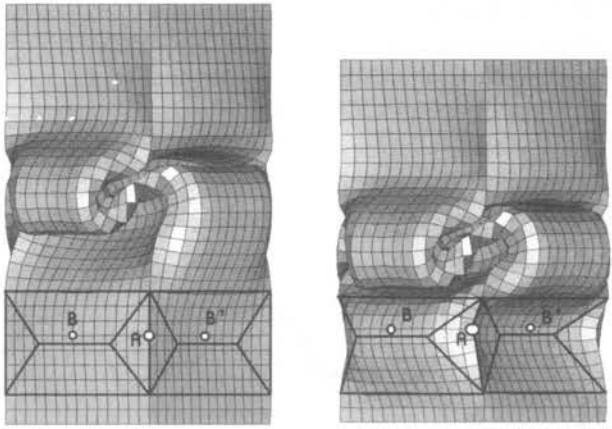

FIGURE 7.6. Detail of simulated deformed tube.

The buckling of these ridge zones corresponds to the decrease of the global crushing load. Figure 7.7 shows the displacement in two perpendicular lateral directions of node A at the corner with the corresponding global crushing force. The displacement value of 41 mm corresponds to the moment where the corner node begins to move laterally and the global crushing force begins to decrease. Furthermore, Fig. 7.8 shows the profile of lateral displacement of an adjacent plate from the middle (point B) to the corner (point A) at this instant. It can be seen that just before the force decrease, the corner elements are not laterally moved whereas the central element is alraedy displaced laterally in both the static and dynamic cases.

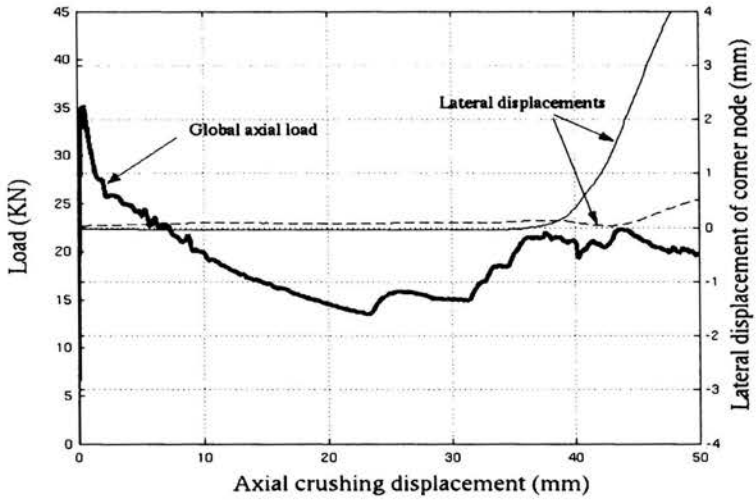

FIGURE 7.7. Lateral displacements of corner node and global crushing force.

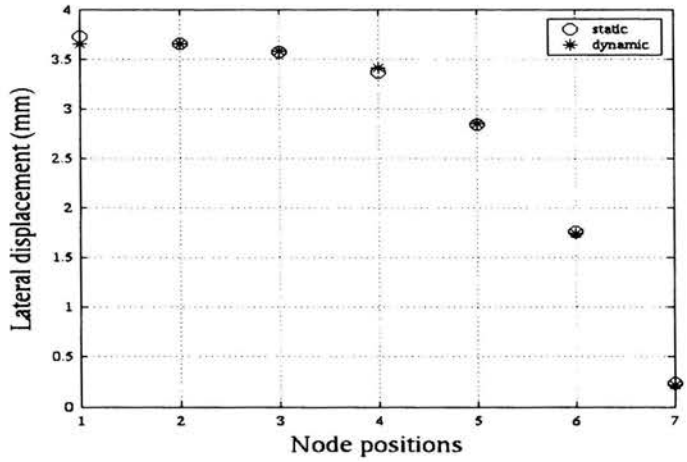

FIGURE 7.8. Lateral displacement of 7 elements in half width of the flat plate (position 1 denotes the element in the middle of the flat plate, position 7 – the element in the ridge line).

Let us extract an idealized crushing square box model (Abramowicz and Wierzbicki, 1989; Wierzbicki and Huang, 1991; Markiewicz *et al.*, 1996; Meng and Al-Hassani, 1983) shown in Fig. 7.9. The crushing process can be divided into two stages. The first one is mainly bending of central plates in an X-form, one plate turns out of the box and its adjacent plate turns into the box. The kinematical compatibility can be obtained by the rigid turning of two vertically adjacent triangular elements and the vertical compression of these triangular elements. The second phase is the buckling of these 8 angular elements around the four ridges.

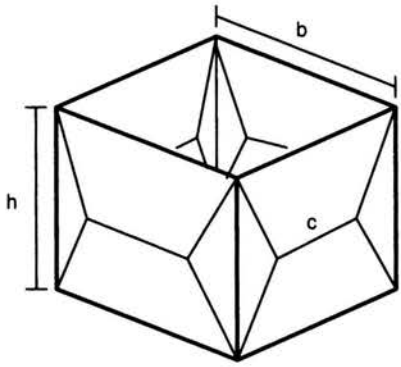

FIGURE 7.9. Kinematical motions during crushing.

It is also interesting to examine the stress profile in the crushing direction, e.g., in the cross section from node B to node A (see Fig. 7.6). It shows that the corner element supports most of the crushing load (Fig. 7.10). It explains why the buckling force of these zones determines the peak loads in the progressive folding process. Similar conclusions can be drawn for static as well as dynamic cases.

The folding peak load is related to the buckling forces of the quasi-straight triangular zone. Indeed, the apparent imperfection is very important in this progressive folding process (bending of X-form plate). As most part of progressive crushing load is supported by the straight corner zones with small imperfections and consequently inertia sensitive, the inertia effect will affect this progressive folding peak load.

>From Fig. 7.11, one can see that in the dynamic case the von Mises equivalent strain profile is higher than that in the corresponding static case, and this is especially true for the corner elements. It reveals that in these

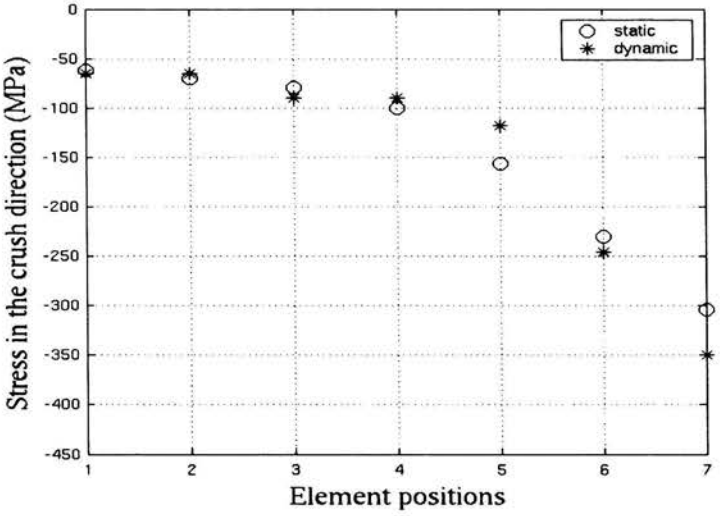

FIGURE 7.10. Stress profile in the crushing direction from centre to corner.

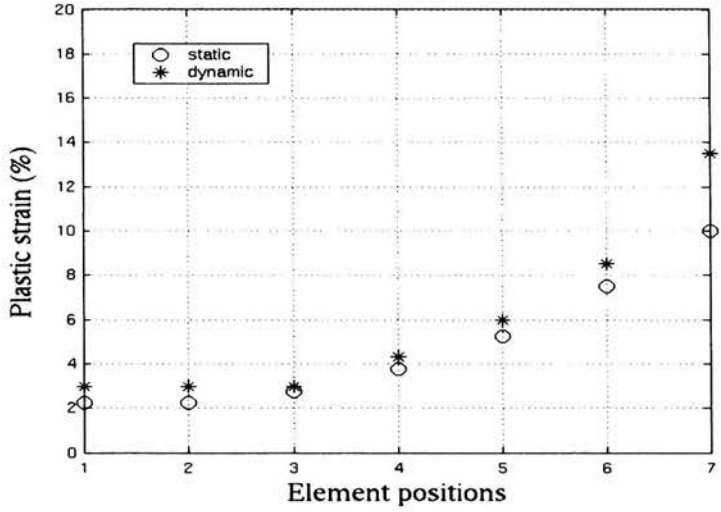

FIGURE 7.11. Residual strain profiles from middle to corner.

small areas, elements are more compressed under dynamic loading because of the inertia effect, as in the case of a straight column. As the base material (brass) is strain hardening, the buckling theory for a straight beam under dynamic loading may explain such a strength enhancement under impact loading.

We observe that the stress and strain shown here are the values at the Gauss points in the neutral mid-surface of the plates.

7.4. Theoretical analysis of the model structure

In Table 7.1, the enhancement of initial and progressive peak loads are very close, hence we conclude that in both cases they may be due to the same cause – the inertia effect.

7.4.1. First peak load

The initial peak load arises with the increase of the impact velocity. If one divides the crushing force by the cross section of the tube, the calculated nominal stress follows the stress-strain curve of the base material as predicted by the buckling theory of a straight column (Fig. 7.12). This initial peak load

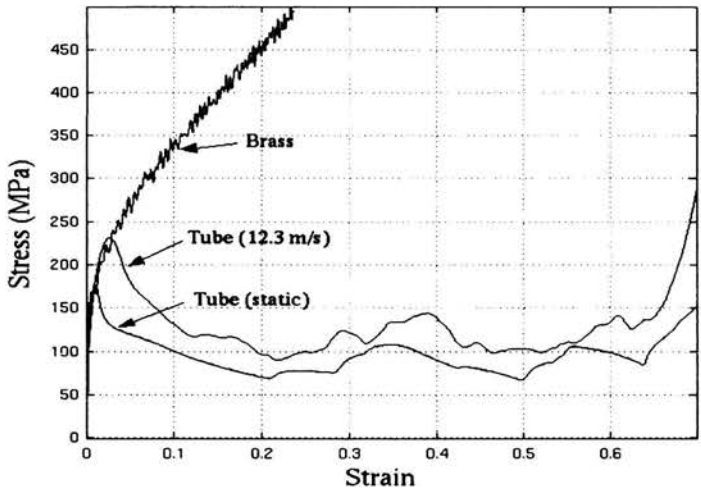

FIGURE 7.12. Force divided by cross section area vs. displacement divided by length.

is determined by the compressive load at the moment when the structure leaves the simple compression loading.

The static initial peak load can be estimated with the flow stress for the buckling strain multiplied by the tube cross sectional area. Thus, under static loading, the strain before buckling is about 1.5% of that corresponding to the flow stress (about 175 MPa). The following estimate is readily obtained:

$$F^{\text{static}}_{\text{initial peak}} = \sigma_s A = 175\,\text{MPa} \cdot 201\,\text{mm}^2 \approx 35\,\text{kN}.$$

Under impact loading, the inertia effect mentioned in the introduction leads to a more important strain of 3% and the corresponding flow stress of about 225 MPa, so that

$$F^{\text{impact}}_{\text{initial peak}} = \sigma_s A = 225\,\text{MPa} \cdot 201\,\text{mm}^2 \approx 46\,\text{kN}.$$

Such an initial peak load implies that a possible bending mode other than uniaxial compression may exist when the force is greater than this load. Taking the idealized box column model of Fig. 7.9 for a given small angle θ corresponding to the strain of about 2%, one can apply a small perturbation on this state state (just *after* initial buckling) to get an energy balance analysis. Figure 7.13 gives a simplified case of this idealized buckling box with the wave length equal to b and the middle length of the X element being $b/2$.

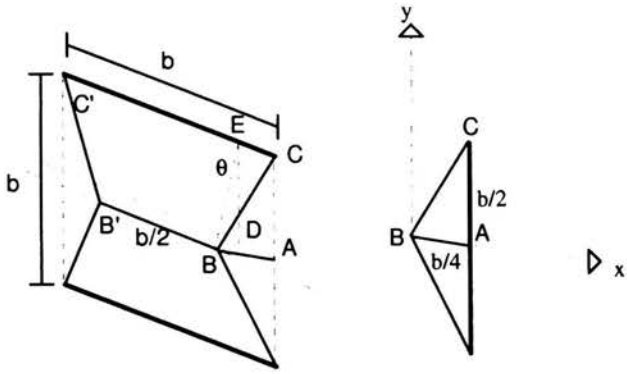

FIGURE 7.13. More detailed crushing box column model.

The energy increment is contributed by the 4 X-form bending elements and 8 triangular corner elements. The total energy increment is then the sum of the partial energies of 8 trapezoids BB'CC' and 16 triangles ABC. Let us

consider a small crushing increment δv which is a vertical displacement of the line CC' with respect to the symmetrical central line BB'.

To calculate the energy increment in one of the 16 triangular elements (ABC) corresponding to the crushing displacement δv, a uniform strain state in the triangle and no displacement in x-direction are assumed. Within the framework of incompressible plasticity, it leads to the following strain state:

$$\delta\varepsilon^p = \begin{bmatrix} 0 & \dfrac{\delta v}{b/2} & 0 \\ \dfrac{\delta v}{b/2} & \dfrac{\delta v}{b/2} & 0 \\ 0 & 0 & -\dfrac{\delta v}{b/2} \end{bmatrix}. \tag{7.1}$$

We recall that $b/2$ and $b/4$ are the lengths of AC and AB of the triangle ABC (Fig. 7.13), respectively.

The equivalent strain is

$$\delta\varepsilon^p_{\text{eq}} = 4\sqrt{\frac{2}{3}}\,\frac{\delta v}{b}. \tag{7.2}$$

If σ_s, t denotes the flow stress and the wall thickness, the energy increment in all the small triangles is

$$\Delta E_{\text{triangle}} = 16\left[\int_V \sigma_s\,\delta\varepsilon^p_{\text{eq}}\,d\Omega\right] = 16\sigma_s\,4\sqrt{\frac{2}{3}}\,\frac{\delta v}{b}\,\frac{b^2 t}{16}. \tag{7.3}$$

By assuming that the energy of X-form elements is absorbed only by plastic hinge lines (CC', BB', BC, B'C') and the X-form element is free from compression or shear, a perturbation rotation of $\delta\theta$ about hinge line CC' leads to a rotation $2\delta\theta$ about hinge line BB'. In the present situation, the hinge lines BC and B'C' will rotate by $\delta\varphi$.

To calculate the bending energy increment in the X-form element, the relationship between $\delta\varphi$ and $\delta\theta$ is required (Fig. 7.14). Here φ denotes the angle between the triangles BCE and ABC. The normal directions of the triangle BCE and ABC are, respectively:

$$\mathbf{v}_1 = \begin{bmatrix} \cos\theta \\ 0 \\ \sin\theta \end{bmatrix}, \qquad \mathbf{v}_2 = \begin{bmatrix} \cos 2\theta \\ \sin 2\theta \\ 0 \end{bmatrix}. \tag{7.4}$$

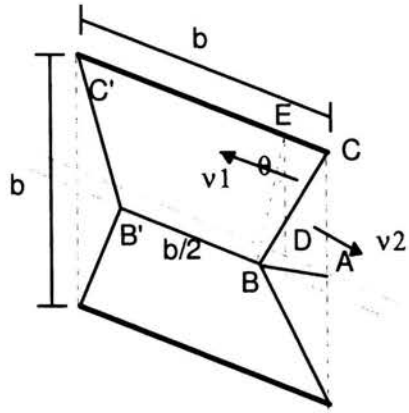

FIGURE 7.14. Relationship between rotation angles θ and φ.

The angle φ is calculated by:

$$\cos\varphi = \mathbf{v}_1 \cdot \mathbf{v}_2 = \cos\theta\cos 2\theta. \tag{7.5}$$

For a very small angle, we can make following approximation:

$$\varphi = 3\theta \quad \text{and} \quad \delta\varphi = 3\delta\theta. \tag{7.6}$$

For the general case, we have the following differential relation:

$$\sin\varphi\delta\varphi = (\sin\theta\cos 2\theta + 2\cos\theta\sin 2\theta)\,\delta\theta. \tag{7.7}$$

Let us define the density of the plastic moment per unit length within the hinge line as

$$m_p = \frac{t^2\sigma_s}{4}. \tag{7.8}$$

The whole bending energy of the square box can be defined as follows:

$$\Delta E_{\text{bending}} = 8\left[m_p\,\delta\theta\,b + m_p\,\delta\theta\,\frac{b}{2} + 2m_p\,\delta\varphi\,\sqrt{5}\,\frac{b}{4}\right]. \tag{7.9}$$

Using the geometric relation between the vertical displacement and the rotation angle in Eq. (3.1), the angle $\delta\theta$ is related to δv by:

$$\delta\theta = \frac{2\delta v}{b\sin\theta}. \tag{7.10}$$

Finally the bending energy increment is

$$\Delta E_{\text{bending}} = (3 + 3\sqrt{5})\sigma_s t^2 \frac{2\delta v}{b \sin\theta} b. \tag{7.11}$$

The energy balance is written as:

$$2F\delta v = (3 + 3\sqrt{5})\sigma_s t^2 \frac{2\delta v}{\sin\theta} + \sigma_s 4\sqrt{\frac{2}{3}}\,\delta v\, bt, \tag{7.12}$$

so that the applied load becomes

$$F = 3(1 + \sqrt{5})\sigma_s \frac{t^2}{\sin\theta} + \sigma_s 2\sqrt{\frac{2}{3}}\, bt. \tag{7.13}$$

The angle θ is related to the ridge line variation ratio (i.e. the strain for the ridge element) by the following relationship:

$$\cos\theta = \frac{b - b\varepsilon}{b}, \tag{7.14}$$

where ε is the strain at the ridge line.

At the instant just after initial buckling, the ridge line strain is about 2% (see Fig. 7.12) and it leads to an angle of 11°. In the present case where $b = 35\,\text{mm}$, $t = 1.5\,\text{mm}$, $\sigma_s = 175\,\text{MPa}$ (static case), we have:

$$F \approx 114\,\text{mm}^2\sigma_s + 85\,\text{mm}^2\sigma_s \approx 35\,\text{kN}. \tag{7.15}$$

Equation (7.15) shows that at the given strain (2%), the present bending model yields the same crushing load as that of the previous pure compressive situation. It means then that the initial peak load corresponds to the buckling of X-form elements in the centre of each plate. The inertia effect under impact loading leads to an increased strain before buckling and consequently to a higher peak load. Equation (7.15) provides also the respective contributions from bending (first term) and from triangular elements (second term).

7.4.2. Progressive peak load

However, our interest is the progressive peak load because it is the basis of the crushing strength enhancement for cellular structures. The simulations in Sec. 7.3 show that buckling of the vertically straight triangular elements determines the progressive peak load. One should analyze further crushing of the idealized crushing box shown in Fig. 7.14 obtained by further bending

of X-form central plates and compression-shear of the straight triangular elements.

Let us consider the instant just before the buckling of these straight triangular elements. The angle θ is 28.4° for the ridge strain of 12% (see Fig. 7.14).

>From the simulated results (Fig. 7.10), further crushing leads to a linear distribution of the strain and stress in the triangular elements. By assuming that the further drop of point C will induce a linear plastic strain distribution, the strain increment becomes

$$\delta\varepsilon^p(x) = \frac{4x}{b}\begin{bmatrix} 0 & \dfrac{\delta v}{b/2} & 0 \\ \dfrac{\delta v}{b/2} & \dfrac{\delta v}{b/2} & 0 \\ 0 & 0 & -\dfrac{\delta v}{b/2} \end{bmatrix}, \tag{7.16}$$

and the equivalent strain is

$$\delta\varepsilon^p_{\text{eq}}(x) = 4\sqrt{\frac{2}{3}}\,\frac{\delta v}{b}\,\frac{4x}{b}. \tag{7.17}$$

The energy increment in these small triangles is then given by

$$\begin{aligned} \Delta E_{\text{triangle}} &= 16\left[\int_V \left[(\sigma_s' - \sigma_s)\,\frac{4x}{b} + \sigma_s\right]\delta\varepsilon^p_{\text{eq}}(x)\,d\Omega\right] \\ &= 16\left[4\sqrt{\frac{2}{3}}\frac{\delta v}{b}\left[(\sigma_s' - \sigma_s)\,\frac{b^2 t}{32} + \sigma_s\frac{2}{3}\,\frac{b^2 t}{16}\right]\right], \end{aligned} \tag{7.18}$$

where the flow stress is also a linear function of x (see Fig. 7.10). It varies from σ_s (compression flow stress just before initial peak load as used in Eq. (7.15) to σ_s' (maximum flow stress at the ridge line before the progressive folding load).

The bending energy increment is defined according to Eq. (7.9) with $\delta\varphi \cong 2\delta\theta$ for the angle $\theta = 28.4°$ (see Eq. (7.7)):

$$\Delta E_{\text{bending}} = (3 + 2\sqrt{5})\sigma_s t^2 \frac{2\delta v}{b\sin\theta}\,b. \tag{7.19}$$

The energy balance yields:

$$F = (3 + 2\sqrt{5})\sigma_s \frac{t^2}{\sin\theta} + \sigma_s'\sqrt{\frac{2}{3}}\,bt + \sigma_s\frac{1}{3}\sqrt{\frac{2}{3}}\,bt. \tag{7.20}$$

In the present case we have: $b = 35\,\text{mm}$, $t = 1.5\,\text{mm}$, $\sigma_s = 175\,\text{MPa}$, $\sigma'_s = 350\,\text{MPa}$ (see Figs. 7.10 and 7.3), so that:

$$F^{\text{static}}_{\text{progressive peak}} \approx 35\,\text{mm}^2\,\sigma_s + 42\,\text{mm}^2\,\sigma'_s + 14\,\text{mm}^2\,\sigma_s \approx 23\,\text{kN}. \quad (7.21)$$

Under dynamic loading, the strain is increased before buckling, which leads to $\sigma_s = 225\,\text{MPa}$, $\sigma'_s = 425\,\text{MPa}$, and therefore

$$F^{\text{impact}}_{\text{progressive peak}} \approx 35\,\text{mm}^2\,\sigma_s + 42\,\text{mm}^2\,\sigma'_s + 14\,\text{mm}^2\,\sigma_s \approx 29\,\text{kN}. \quad (7.22)$$

Such a simple model does not reflect exactly the real folding process. For example, the x-displacement is not zero and the base size of the triangular element increases during crushing. However, it offers a good explanation of the progressive peak load. Equations (7.19) and (7.20) provides also respective contributions of X-form bending elements (first terms) and of the triangular elements. Another feature of this model is that the vertically straight triangular elements take more than 80% of crushing load (see also the last column of Table 7.1). The progressive folding load is very sensitive to inertia because the contribution of the bending to inertia sensitivity is relatively small.

7.5. Post-buckling micro-hardness measurement for the validation

The above simulations and analyses suggest that the inertia effect is the origin of the strength enhancement under dynamic loading. To prove that, the micro-hardness test on the crushed tubes at various crushing stages has been performed. It provides an experimental examination of the local information given by the simulation. The micro-hardness of the material reveals an average strain hardening state of the material. It is also known that the hardness measurement and the plastic strain are not directly and quantitatively related. However, if reference tests on the base material for a series of given strain levels are performed, a quantitative relationship can be derived for this material under such loading.

The strain states for small specimens are known according to the compressive stress-strain curves (Fig. 7.3) of the base material. Post-buckling micro-hardness measurements on these small specimens give correspondence between the micro-hardness and known plastic strain. This correspondence for treated brass material is shown in Fig. 7.15. The same micro-hardness measurement is applied to the square tubes.

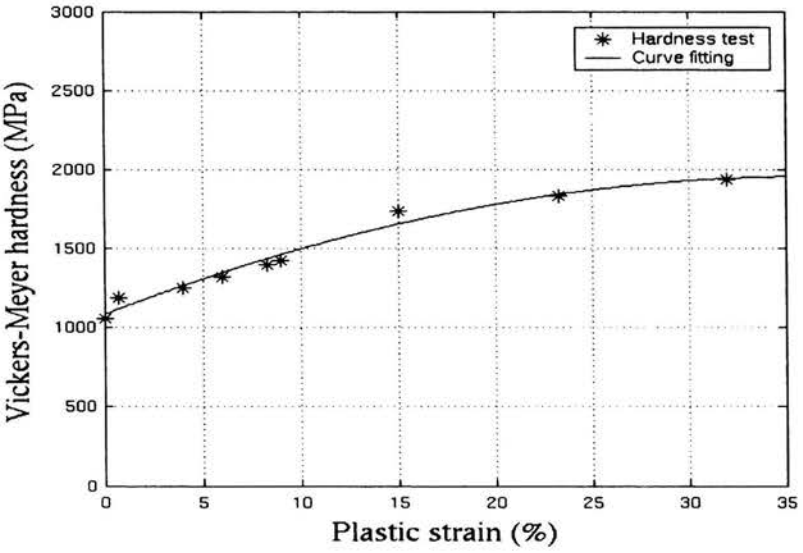

FIGURE 7.15. Micro-hardness vs. plastic strain.

Qualitative and quantitative matching can then be sought between simulations and experiments. Figures 7.16 and 7.17 show a typical micro-hardness measurement operation. Three crushing states under static loading are used for this matching. The first is the one just after the first peak load (see Fig. 7.16(a), left), and the second is the one just after the second peak load which is the progressive peak load (middle). The last one corresponds to the case after full crushing (right). Figures 7.16(b) and 7.16(c) show the specimen preparation and the stamp of the indentation for the micro-hardness measurement. It is noted that the measurement presented in Fig. 7.17 is performed in the middle of the plate (half-thickness position). Actually the hardness near the plate surfaces is quite different because of the bending effect.

Such a measurement proves that:

- just after the first initial peak load, the plastic strain is nearly uniform in a section;
- afterwards, only the region near the ridge line is loaded.

Thus the theory developed above is confirmed. Furthermore, an excellent match between simulation and post-buckling micro-hardness measurement is found (Fig. 7.18). It validates the results given by simulations.

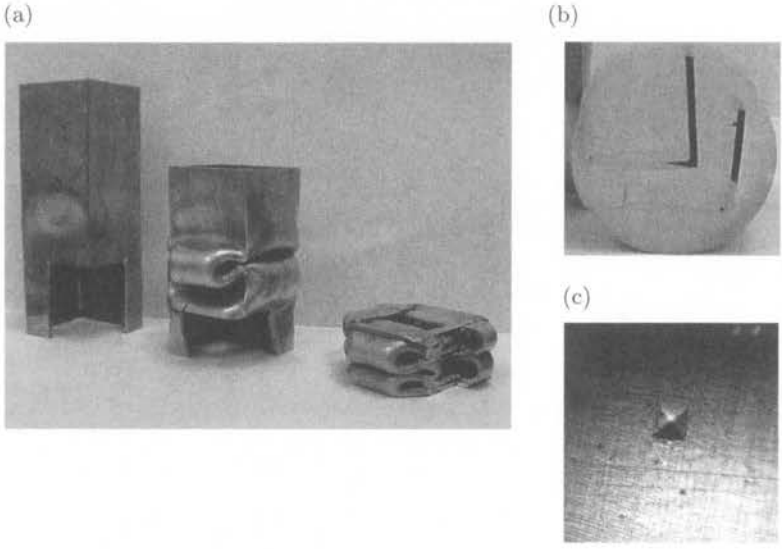

FIGURE 7.16. (a) crushed tubes, (b) prepared piece for hardness measurement, (c) stamp.

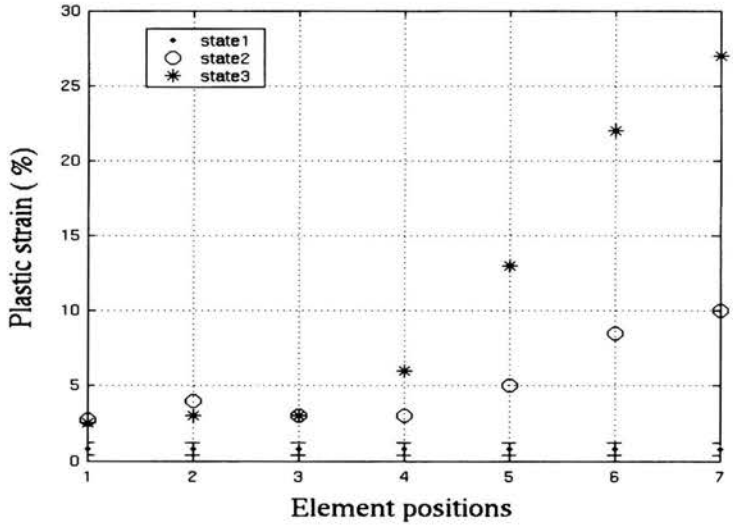

FIGURE 7.17. Plastic strain profiles at three crushing stages (position 1 denotes the element in the middle of the flat plate, position 7 denotes the element in the ridge line).

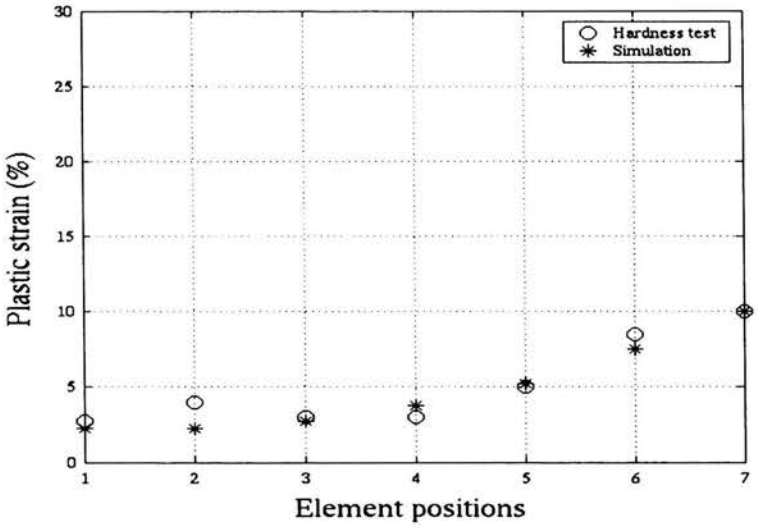

FIGURE 7.18. Comparison simulation and micro-hardness measurement.

7.6. Summary

This Chapter treats the rate sensitivity due to structure effect by studying a model structure of a Cu-Zn alloy square tube. Actually, the observed crushing mode of this square tube is a progressive folding process, which is also the crushing mode for cellular structures such as IFAM aluminium foam and honeycombs. The static and dynamic crushing tests of annealed brass square tubes under a symmetric progressive folding mode were presented. Tests under dynamic loading were performed with a large scale (80 mm diameter, and 10 m long) SHPB system, using recently developed two-gauge method to obtain a sufficient measuring duration. It provides an accurate measurement of force-displacement curves, with accurate values not only for the initial peak load, but also for the progressive folding peak load. An enhancement of the progressive folding peak load is observed.

Careful characterization of the behaviour of the base material is performed and it shows that there is no observable rate sensitivity up to 2500/s. Tests on tubes and also on the base material show that the progressive folding peak load of square tubes made of a rate insensitive base material can have an important enhancement under impact loading. To understand this significant enhancement for square tubes, a numerical simulation of these tests is performed, using a rate insensitive constitutive law (Johnson–Cook

law with zero rate sensitivity). The material parameters are determined using experimental results on samples cut from the tubes. The influence of the element size and the initial imperfection amplitude on the final results was also studied. The simulations reproduce the observed deformation map and the event sequences, as well as the crushing force and the displacements measured during the tests.

These virtual tests provide all the details in stresses and strains during crushing of tubes, which is very difficult to measure in the experiments. Careful examinations of the stress and strain profiles show that small zones around the four ridges of square tubes remain straight and support the main loading in the folding process. Buckling of these zones corresponds to the fall of the crushing force. Under impact loading, buckling takes place at a larger strain than the static case. Post-buckling micro-hardness measurements at various crushing stages confirm this result.

A simple model of box column crushing is used to illustrate the progressive folding process and the role played by inertia. It was shown that the vertically straight corner zones support about 80% of the crushing load. This inertia sensitive structure is responsible for the observed progressive peak load enhancement under impact loading.

Bibliography

1. ABRAMOWICZ, W., JONES, N., (1984), Dynamic axial crushing of square tubes, *Int. J. Impact Engng.*, **2**, 179-208.

2. ABRAMOWICZ, W., JONES, N., (1986), Dynamic progressif buckling of circular and square tubes, *Int. J. Impact Engng.*, **4**, 243-270.

3. ABRAMOWICZ, W., WIERZBICKI, T., (1989), Axial crushing of multicorner sheet metal columns, *Journal of Applied Mechanics*, **56**, 113-120.

4. ACHENBACH, J.D., (1978), *Wave propagation in elastic solids*, North-Holland publishing company.

5. ALBERTINI, C., DEL GRANDE, A., DELZANO, A., KIEFER, R., MONTAGNINI, M., MURAROTTO, M., PIZZINATO, E.V., RODIS A., and SCHNABEL, A.W., (1993), New approach to crashworthiness studies of automotive and aerospace sheet metal structure by a large Hopkinson bar method, *Structure Dynamics* (Eurodyn 93, eds.: T. Moan, P.G. Bergan, O.T. Gudmestad, C.M. Larsen, S. Nordal, S. Remseth, A.N. Nounadis, W.B. Krätzig, and G.I. Schuëller), Publ. A.A. Balkema, Rotterdam, 539-545.

6. BACON, C. FÄRM, J., and LATAILLADE, J.L., (1994), Dynamic fracture toughness determined from load-point displacement, *Exper. Mech.*, **34**(9), 217-223.

7. BACON, C., (1998), An experimental method for considering dispersion and attenuation in a viscoelastic Hopkinson bar, *Experimental Mechanics*, **38**, 242-249.

8. BACON, C., (1999), Separation of waves propagating in an elastic or viscoelastic Hopkinson pressure bar with three-dimensional effects, *Int. J. Impact Engng.*, **22**, 55-69.

9. BACON, C., BRUN, A., (2000), Methodology for a Hopkinson test with a non-uniform viscoelastic bar, *Int. J. Impact Engng.*, **24**, 219-230.

10. BADICHE, X., FOREST, S., GUIBERT, T., BIENVENU, Y., BARTOUT, J.-D., IENNY, P., CROSET, M., and BERNET, H., (2000), Mechanical properties

and non-homogeneous deformation of open-cell nickel foams: application of the mechanics of cellular solids and of porous materials, *Mater. Sci. & Engng. A*, **A289**, 276-288.

11. BANHART, J., (2001), Manufacture, characteristaion and application of cellular metals and metal foams, *Progress in Material Science*, **46**, 559-632.

12. BANHART, J., and BAUMEISTER, J., (1998), Deformation characteristics of metal foam, *J. Mater. Sci.*, **33**, 1431-1440.

13. BANCROFT, D., (1941), The velocity of longitudinal waves in cylindrical bars, *Phys. Rev.* **59**, 588-593.

14. BELL, J.F., (1966), An experimental diffraction grating study of the quasi-static hypothesis of the split Hopkinson bar experiment, *J. Mech. Phys. Solids*, **14**, 309-327.

15. BERTHOLF, L.D., and KARNES, J., (1975), Two-dimensional analysis of the split Hopkinson pressure bar system, *J. Mech. Phys. Solids*, **23**, 1-19.

16. BLANC, R.H., (1993), Transient wave propagation methods for determining the viscoelastic properties of solids, *J. Appl. Mech.*, **60**, 763-768.

17. BLAND, D.R., (1960), *The Theory of Linear Viscoelasticity*, Oxford Univ. Press., Oxford.

18. BLAZY, J.S., (2003), *Comportement mécanique des mousses d'aluminium: caractérisations expérimentales sous sollicitations complexes et simulations numériques dans le cadre de l'élasto-plasticité compressible*, Ph.D thesis, Ecole des Mines de Paris.

19. BUI, H.D., (1993), *Introduction aux problèmes inverses en mécanique des matériaux.* Editions Eyrolles, Paris. English translation: *Inverse Problems in the Mechanics of Materials: An Introduction*, CRC Press, Boca Raton, 1994.

20. BUDIANSKY, B., HUTCHINSON, J.W., (1964), Dynamic buckling of imperfection sensitive structures, *Proc. 11^{th} international Congress of Applied Mechanics*, Springer Verlag, Munich.

21. BUSSAC, M.N., COLLET, P.C, GARY, G., OTHMAN, R., (2002), An optimisation method for separating and rebuilding one-dimensional dispersive waves from multi-point measurements. Application to elastic or viscoelastic bars, *J. Mech. Phys. Solids*, **50**, 321-349.

22. CALLADINE, C. R., and ENGLISH, R.W., (1984), Strain-rate and inertia effects in the collapse of two types of energy-absorbing structure, *Int. J. Mech. Sci.*, **26**, 689-701.

23. CAMPBELL, J.D., and DUBY, J., (1956), The yield behaviour of mild steel in dynamic compression, *Proc. R. Soc. Lond.*, **A236**, 24-40.

24. CHANG F.S., SONG, Y., LU, D.X., and DESILVA, C.N., (1998), Unified constitutive equations of foams materials, *ASME J. Engng. Mater. Tech.*, **120**, 212-217.

25. CHASTEL, Y., and HUDRY, E., and FOREST, S., and PEYTOUR, C., (1999), Mechanical behaviour of aluminium foam for various deformation paths, *Experiment and Modelling, Metal Foam and Porous Metal Structures*, J. Banhart, M.F. Ashby, and N.A. Fleck (Eds.), Verlag MIT Publishing, pp.263-268.

26. CHEN, W., ZHANG, B., and FORRESTAL, M.J., (1999), A split Hopkinson bar technique for low-impedance materials, *Experimental Mechanics*, **39**, 81-85.

27. CHEN, W., LU, F., and ZHOU, B., (2000), A quartz crystal imbedded split Hopkinson bar for soft materials, *Experimental Mechanics*, **40**, 1-6.

28. CHEN, W., LU, F., and WINFREE, N.A., (2002), Dynamic compressive response of polyurethane foams of various densities, *Experimental Mechanics*, **42**, 65-73.

29. CHEVALIER, L., CALLOCH, S., HILD, F., and MARCO, Y., (2001), Digital image correlation used to analyse the multiaxial behavior of rubber-like materials, *European Journal of Mechanics A/Solids*, **20**, 169-187.

30. CHIU, S.S., and NEUBERT, V.H., (1967), Difference method for wave analysis of the split Hopkinson pressure bar with a viscoelastic specimen, *J. Mech. Phys. Solids*, **15**, 177-193.

31. CHREE, C., (1889), The equations of an isotropic elastic solid in polar and cylindrical coordinates, their solutions and applications, *Cambridge Phil. Soc. Trans.*, **14**, 250-369.

32. CONN, A.F., (1965), On the use of thin wafers to study dynamic properties of metals, *J. Mech. Phys. Solids*, **13**, 311-327.

33. CRISTESCU, N., (1967), *Dynamic Plasticity*, North-Holland Publishing Company, Amsterdam.

34. COQUIN, G.A., (1964), Attenuation of guided waves in isotropic viscoelastic materials, *J. Acoustic society of America*, **36**(6), 1074-1080.

35. DESHPANDE, V.S., and FLECK, N.A., (2000), High strain rate compressive behaviour of aluminium, *Int.J.Impact Engng.*, **24**, 277-298.

36. DESHPANDE, V.S., and FLECK, N.A., (2000), Isotropic constitutuve models for metallic foams, *J. Mech. Phys. Solids*, **48**, 1253-1283.

37. DAVIES, R.M., (1948), A critical study of Hopkinson pressure bar, *Philosophical Transaction of Royal Society*, **A240**, 375-457.

38. DAVIES, E.D.H., and HUNTER, S.C., (1963), The dynamic compression testing of solids by the method of the split Hopkinson pressure bar, *J. Mech. Phys. Solids*, **11**, 155-179.

39. DHARAN, C.K.H., and HAUSER, F.E., (1970), Determination of stress-strain characteristics at very high strain rates, *Exp. Mech.*, **10**, 370-376.

40. DUFFY, J., CAMPBELL, J.D., and HAWLEY, R.H., (1971), On the use of a torsional split Hopkinson bar to study rate effects in 1100-0 aluminium, *J. Appl. Mech.*, **38**, 83-91.

41. FARUQUE, O., LIU, N., and CHOU, C., (1997), Strain rate dependent foam – constitutive modeling and applications, *S.A.E Transactions - J. Materials & Manufacture*, **106**, 904-912.

42. FAZEKAS, A., DENDIEVEL, R., SALVO, L., BRECHET, Y., (2002), Effect of microstructural topology upon the stiffness and strength of 2D cellular structures, *Int. J. Mech. Sci.*, **44**, 2047-2066.

43. FOLLANSBEE, P.S., and FRANZ, C., (1983), Wave propagation in the split Hopkinson pressure bar, *J. Engng. Mater. Tech.*, **105**, 61-66.

44. GARY, G., (1983), Dynamic buckling of an elastoplastic column, *Int. J. Impact Engng.*, **1**, 357-375.

45. GARY, G. ROTA, L., and ZHAO, H., (1995), Tecting viscous soft materials at medium and high strain rates, *IUTAM Symposium on Constitutive Relation in High/Very High Strain Rates*, 16-19 October, NODA, Japan.

46. GIBSON, L.J., and ASHBY, M.F., (1988), *Cellular Solids*, Pergamon Press.

47. GOLDSMITH, W., and SACKMAN, J.L., (1992), An experimental study of energy absorption in impact on sandwich plates, *Int. J. Impact Engng.*,**12**, 241-262.

48. GOLDSMITH, W., and LOUIE, D.L., (1995), Axial perforation of aluminium honeycombs by projectiles, *Int. J. Solids & Structs.*, **32**, 1017-1046.

49. GONG, J.C. MALVERN, L.E., and JENKINS, D.A., (1990), Dispersion investigation in the split Hopkinson pressure bar, *J. Engng. Mater. Tech.*, **112**, 309-314.

50. GORHAM, D.A., (1983), A numerical method for the correction of dispersion in pressure bar signals, *J. Phys. E: Sci. Instrum.*, **16**, 477-479.

51. GRAFF, K.F., (1975), *Wave motion in elastic solids.* Ohio State University Press.

52. HANSSEN A.G., LANGSETH, M., and HOPPERSTAD, O.S., (2000), Static and dynamic crushing of square aluminium extrusions with aluminium foam filler, *Int. J. Impact Engng.*, **24**, 347-383.

53. HILD, F., PÉRIÉ, J.N, CORET, M., (1999), *Mesure de champs de déplacements 2D par intercorrélation d'images.* Correli2D, LMT-Cachan, internal report No.230.

54. HARDING, J., WOOD, E.D., and CAMPBELL, J.D., (1960), Tensile testing of materials at impact rates of strain, *J. Mech. Engng. Sci.*, **2**, 88-96.

55. HAUSER, F.E., (1966), Techniques for measuring stress-strain relations at high strain rates, *Exp. Mech.*, **6**, 395-402.

56. HÖNIG, A., STRONGE, W.J., (2002), In-plane dynamic crushing of honeycomb. Part II: application to impact, *Int. J. Mech. Sci.*, **44**, 1697–1714.

57. HOLZER, A.J., (1978), A technique for obtaining compressive strength at high strain rates using short load cells, *Int. J. Mech. Sci.* **20**, 553-560.

58. HOPKINSON, B., (1914), A method of measuring the pressure in the deformation of high explosives by the impact of bullets, *Phil. Trans. Roy. Soc.*, **A213**, 437-452.

59. HUNTER, S.C, (1960), Viscoelastic waves, *Progress in solid mechanics*, **1**, N. Sneddon and R. Hill (Eds.), North-Holland, Amsterdam, 1-57.

60. HUMEN, V., and POTESIL, A., (1993), Pulse method used to identify material properties in linear viscoelastic media, *Int. J. Impact Engng.*, **13**, 85-98.

61. JACQUELIN, E., HAMELIN, P., (2003), Force recovered from three recorded strains, *Int. J. Solids & Structs.*, **40**, 73-88.

62. JAHSMAN, W.E., (1971), Reexamination of the Kolsky technique for measuring dynamic material behavior, *J. Appl. Mech.*, 77-82.

63. JULLIEN, A., LAUNAY, J., and GUILLET, C., (1995), Structural sandwiches for railway structures, mechanical test, *Mécanique idustrielle et Matériaux*, **48**, 204-207.

64. KARAGIOZOVA D., ALVES M., and JONES, N., (2000), Inertia effects in axisymmetrically deformed cylindrical shells under axial impact, *Int. J. Impact Engng.*, **24**, 1083-1115.

65. KLEPACZKO, J.R., (1969), Lateral inertia effects in the compression impact experiments, *Reports of Inst. Fund. Technical Research*, No.17, Warsaw.

66. KLINTWORTH, J.W., and STRONGE W.J., (1988), Elasto-plastic yield limits and deformation laws for transversely crushed honeycombs, *Int. J. Mech. Sci.*, **30**, 273-292.

67. KLINTWORTH, J.W., and STRONGE, W.J., (1989), Plane punch indentation of a ductile honeycomb, *Int. J. Mech. Sci.*, **31**, 359-378.

68. KOLSKY, H., (1949), An investigation of the mechanical properties of materials at very high rates of loading, *Proc. Phys. Soc.*, **B62**, 676-700.

69. KOLSKY, H., (1956), The propagation of stress pulses in viscoelastic solids, *Phil. Mag.*, **1**(8), 693-710.

70. KOLSKY, H., (1963), *Stress Waves in Solids*, Clarendon Press, Oxford.

71. LACEY, R.M., (1965), Response of several materials at intermediate strain rates, *Fifth Int. Symp. on High Speed Testing*, Boston.

72. LANGSETH, M., HOPPERSTAD, O.S., (1996), Static and dynamic axial crushing of square thin-walled aluminium extrusions, *Int. J. Impact Engng.*, **18**, 949-968.

73. LANGSETH, M., HOPPERSTAD, O.S., BERSTAD, T., (1999), Crashworthiness of aluminium extrusions: validation of numerical simulation, effect of mass ratio and impact velocity, *Int. J.Impact Engng.*, **22**, 829-854.

74. LATAILLADE, J.L., BACON, C., COLLOMBET, F., and DELAET, M., (1994), The benefit of Hopkinson bar of composite and ceramic materials, *Wave Propagation and Emerging Technologies*, W.K. Kinra, R.J. Clifton, and G.C. Johnson (Eds.), *AMD*, **188**, 85-93.

75. LEHMHUS, D., and BANHART, J., (2003), Properties of heat-treated aluminium foams, *Materials Science and Engineering A*, 1-13.

76. LIFSHITZ, J.M., and LEBER, H., (1994), Data processing in the split Hopkinson pressure bar tests, *Int. J. Impact Engng.*, **15**, 723-733.

77. LINDHOLM, U.S., (1964), Some experiments with the split Hopkinson pressure bar, *J. Mech. Phys. Solids*, **12**, 317-335.

78. LOIZOU, N., and SIMS, R.B., (1953), The yield stress of pure lead in compression, *J. Mech. Phys. Solids*, **1**, 234-243.

79. LUNDBERG, B., and HENCHOZ, A., (1977), Analysis of elastic waves from two-point strain measurement, *Exper. Mech.*, **17**, 213-218.

80. LUNDBERG, B., CARLSSON J., and SUNDIN K. G., (1990), Analysis of elastic waves in non-uniform rods from two-point strain measurement, *J. Sound and Vibration*, **137**, 483-493.

81. MAIRE, E., ELMOUTAOUAKKIL, A., FAZEKAS, A., and SALVO, L., (2003), In-situ measurements of deformation and failure of metallic foams using X-ray tomography, *MRS bulletin*, **28**, 284-289.

82. MALINOWSKI, J.Z., and KLEPACZKO, J.R., (1986), Dynamic frictional effects as measured from the split Hopkinson bar, *Int. J. Mech. Sci.*, **28**, 381-391.

83. MARKIEWICZ, E, DUCROCQ, P., DRAZETIC, P., and RAVALARD, Y., (1996), Calculation of the dynamic axial crushing response of complex prismatic sections, *Int. J. Crashworthiness*, **1**, 203-224.

84. MENG, Q., AL-HASSANI, S.T.S, and SODEN, P.D., (1983), Axial crushing of square tubes, *Int. J. Mech. Sci.*, **25**, 747-773.

85. MEYERS, M.A., (1994), *Dynamic behavoir of Materials.* John Wiley & Sons Inc.

86. MILLS, N.J., (1997), Time dependence of the compressive response of polypropylene bead foam, *Cellular polymers*, **16**, 194-215.

87. MINDLIN, R.D., and MCNIVEN, H.D., (1960), Axially symmetric waves in elastic rods, *J. Appl. Mech.*, **27**, 145-151.

88. MUKAI, T., KANAHASHI, H., MIYOSHI, T., MABUCHI, M., NIEH, T.G., and HIGASHI, K., (1999), Experimental study of energy absorption in a close celled aluminium foam under dynamic loading, *Scripta Materialia*, **40**, 921-927.

89. NAKADA, I., and HAUG, E., (1994), Numerical simulation of crash behaviour of composite structures for automotive applications, *Matériaux & Techniques*, **82**, 33-38.

90. NEMAT-NASSER, S., ISAACS, J.B., and STARRETT, J.E., (1991), Hopkinson techniques for dynamic recovery experiments, *Proc. R. Soc. Lond.*, **A435**, 371-391.

91. OGUNI, K., and RAVICHANDRAN, G., (2000), An energy-based model of longitudinal splitting in unidirectional fiber reinforced composites. Transaction ASME, J. Appl. Mech., **67**, 437-443.

92. OGUNI, K., RAVICHANDRAN, G., (2001), Dynamic compressive behavior of unidirectionnal E Glass/Vinylester composites, *Int. J. Mech. Sci.*, **36**, 831-838.

93. OTHMAN, R., BLANC, R.H., BUSSAC, M.N., COLLET, P., ET GARY, G., (2002), Identification de la relation de dispersion dans les barres, *C. R. Mécanique*, **330**(12), 849-855.

94. POCHHAMMER, L., (1876), Über die Fortpflanzungsgeschwindigkeiten kleiner Schwingungen in einem unbergrenzten isotropen Kreiszylinder, *J. für die Reine und Angewandte Mathematik*, **81**, 324-336.

95. PRALL, D., and LAKES, R.S., (1997), Properties of chiral honeycomb with a Poisson's ratio of -1, *Int. J. Mech. Sci.*, **39**, 305-314.

96. REID, S.R., and PENG, C., (1997), Dynamic uniaxial crushing of wood, *Int. J. Impact Engng.*, **19**, 531-570.

97. REHKOPF, J.D., MCNEICE, G.M., and BORLAND, G.W., (1996), Fluid and Matrix components of polyurethane foam behaviour under cyclic compression, *ASME J. Engng. Mater. Tech.*, **118**, 58-62.

98. RINDE, J.A., HOGE, K.G., (1971), Time and temperature dependence of the mechanical properties of polystyrene bead foam, *J. Apppl. Polymer Sci.*, **15**, 1377-1395.

99. RINDE, J.A., and HOGE, K.G., (1972), Dynamic shear modulus of polystyrene bead foams, *J. Apppl. Polymer Sci.*, **16**, 1409-1415.

100. ROTA, L., (1997), Application de méthode inverse au dépouillement de l'essai aux barres de Hopkinson. Ph.D. Thesis, Ecole Polytechnique.

101. SCHREYER, H.L., ZUO, Q.H., and MAJI, A.K., (1994), Anisotropic plasticity model for foams and honeycombs, *ASCE J. Engng. Mech.*, **120**, 1913-1930.

102. SHIM, V.P.M., YAP, K.Y., and STRONGE, W.J., (1992), Effects of nonhomogeneity, cell damage and strain rate on impact crushing of a strain-softening cellular chain, *Int. J. Impact Engng.*, **12**, 585-602.

103. SU, X.Y., YU, T.X., and REID, S.R., (1995), Inertia sensitive impact energy-absorbing structures part I : Effects of inertia and elasticity, *Int. J. Impact Engng.*, **16**(4), 651-672.

104. TAM, L.L., and CALLADINE, C.R., (1991), Inertia and strain rate efects in a simple plate structure under impact loading, *Int. J. Impact Engng.*, **11**, 689-701.

105. TAN, P.J., HARRIGAN, J.J., and REID, S.R., (2002), Inertia effects in uniaxial dynamic compression of a closed cell aluminium alloy foam, *Mater. Sci. Tech.*, **18**, 480-488.

106. THWAITES, S., and CLARK, N.H., (1995), Non-destructive testing of honeycomb sandwich structure using elastic waves, *J. Sound & Vibration*, **187**, 253-269.

107. TRAEGAR, R.K., (1967), Physical properties of rigid polyurethane foams, *J. Cellular Plastics*, **3**, 405-418.

108. VURAL M., and RAVICHANDRAN, G., (2003), Dynamic response and energy dissipation characteristics of balsa wood: experiment and analysis, *Int. J. Solids & Structs.*

109. WAGNER, D.A., GUR, Y., WARD, S.M., and SAMUS, M.A., (1997), Modelling foam damping materials in automotive structure, *ASME J. Engng. Mater. Tech.*, **119**, 279-283.

110. WU, C.L., WEEKS, C.A., and SUN, C.T., (1995), Improving honeyconb-core sandwich structures for impact resistance, *J. Advanced Mater.*, **26**, 41-47.

111. WU, E., and JIANG, W.S., (1997), Axial crush of metallic honeycombs, *Int. J. Impact Engng.*, **19**, 439-456.

112. WIERZBICKI, T., (1983), Crushing analysis of metal honeycombs, *Int. J. Impact Engng.*, **1**, 157-174.

113. WIERZBICKI, T., HUANG, J., (1991), Initiation of plastic folding mechanism in crushed box column, *Thin-walled Structures*, **13**, 115-143.

114. WIERZBICKI, T., (1995), Material and Structural modelling in collision research, *9th Dymat Technical Conference*, University of Technology, Munich (TUM), Germany.

115. ZHANG, J., KIKUCHI, N., LI, V., YEE, A., and NUSHOLZ, G., (1997), Constitutive modelling of polymeric foam material subjected to dynamic crash loading, *Int. J. Impact Engng.*, **21**, 369-386.

116. ZHAO, H., (1992), *Analyse de l'essai aux barres de Hopkinson, application à la mesure du comportement dynamique des matériaux.* Ph.D. Thesis, ENPC, Paris.

117. ZHAO, H., (1995), Etudes expérimentales du comportement dynamique des matériaux. Polycopiés de cours, *DEA Dynamique des Structures et Couplages.*

118. ZHAO, H., and GARY, G., (1995), A three-dimensional analytical solution of longitudinal wave propagation in an infinite linear viscoelastic cylindrical bar. Application to experimental techniques, *J. Mech. Phys. Solids.*, **43**, 1335-1348.

119. ZHAO, H., and GARY, G., (1996), On the use of SHPB techniques to determine the dynamic behavior of materials in the range of small strains, *Int. J. Solids & Structures*, **33**(23), 3363-3375.

120. ZHAO, H., and GARY, G., (1997), A new method for the separation of waves. Application to the SHPB technique for an unlimited measuring duration, *J. Mech. Phys. Solids*, **45**, 1185-1202.

121. ZHAO, H., and GARY, G., (1998), Crushing behaviour of aluminium honeycombs under impact loading, *Int. J. Impact Engng.*, **21**(10), 827-836.

122. ZHAO, H., and GARY, G., (2002), Behaviour characterisation of polymeric foams over a large range of strain rates, *Int. J. Vehicle Design*, **30**, 135-145.

123. ZUKAS, J.A., (1982), *Impact Dynamics*, John Wiley & Sons, (2nd ed. 1991).

Institute of Fundamental Technological Research
publishes the following periodicals:

Archives of Mechanics — bimonthly (in English)
Archives of Acoustics — quarterly (in English)
Archives of Civil Engineering — quarterly (in English)
Engineering Transactions — quarterly (in English)
Computer Assisted Mechanics and Engineering Sciences — quarterly (in English)
Journal of Technical Physics — quarterly (in English)

Subscription orders for all journals edited by IFTR may be sent directly to:
Editorial Office
Institute of Fundamental Technological Research
Świętokrzyska 21, p. 508
00-049 Warszawa, POLAND